Wearable RF Resonant Gaseous Chemical Sensor Array

by

Wei Ting Chen

A thesis

presented to the University of Waterloo

in fulfillment of the

thesis requirement for the degree of

Doctor of Philosophy

in

Electrical and Computer Engineering

Waterloo, Ontario, Canada, 2015

AUTHOR'S DECLARATION

I hereby declare that I am the sole author of the thesis. This is the true copy of the thesis, including any required final revision, as accepted by the examiners.

I understand that my thesis may be made electronically available to the public.

ABSTRACT

Biomarker detection is a major engineering goal that enables numerous applications in the fields of biomedical and law enforcement. By monitoring the conditions of the subject with a dedicated biomarker detection system, the health condition as well as other biomedical parameters of interest can be evaluated in real-time, and further preemptive measures can be taken to improve the safety and chance of survival of the subject. In the pursuit of a better biomarker monitoring system, the ubiquitous and unobtrusiveness of the sensor is proven to be a critical design factor that directly impacts the subject's safety and the comfort level. The thesis presents the research results obtained for a novel single-port, multi-pole resonant sensor array fabricated on a novel Frame-Flex flexible substrate for a wearable epidermal ethanol sensor system in an attempt to achieve minimal obtrusiveness to the subject under testing. In this system, individual sensors carrying different functional polymers are brought together to share the same electrical input and output, and their resonance behavior along with inter-resonator coupling are captured through a single reflected array response curve (S_{11}). Initially, six RF resonant sensors carrying different polymeric sensing materials have been characterized individually under exposures of ethanol and three other interferents in order to characterize the steady-state and transient responses of the polymeric sensing materials. A thin film resonant sensor and a combline cavity-based resonant gaseous chemical sensor for chemical gas line integrated sensing system have been designed employing some of these polymeric sensing materials. Next, thin film RF sensors have been cascaded together and fabricated on the Kapton-SU-8 Frame-Flex flexible substrate, forming the flexible single-port, multi-resonator resonant sensor array. The array response was collected from its S_{11} response at the input port of the array. Then, a coupling-matrix readout extraction (CMRE) technique has been proposed to determine, from the S_{11} response, the changes in each of the cascaded resonant sensors, which were used as a signature to identify different chemical analytes. The proposed CMRE technique was then employed to obtain the coupling signatures of four analytes on various flexible sensor arrays. It has been successfully shown that the array response analyzed through the CMRE technique can clearly distinguish the presence of ethanol from other chemical interferents. For other complex mixtures of ethanol and other unwanted analytes, the distinctive coupling signatures obtained by CMRE can be used as a reliable data source fed to post-readout multi-variant analysis for pattern recognition. The research has made a contribution to establishing the engineering foundation for the development of wearable transdermal gaseous biomarker sensors / sensor arrays with low cost, optimal unobtrusiveness, and a compact form factor.

ACKNOWLEDGEMENT

This thesis is the grand outcome of enormous efforts made not just by me, but also by my dear family members, my beloved fiancé (A.I. Wang), my advisor (Dr. Raafat Mansour), my coworkers at the Centre of Integrated RF Engineering (CIRFE), the CTO of Sober Steering Sensor Inc. (J. Carroll), my mentors at Equustek Solutions Co. (R. Angus, R. Huth, and W.E. Warda), and my best soul-mate (S.Y.F. Wang). No words can express my immense appreciation to these individuals for their ongoing encouragement and support.

This thesis is also a solemn dedication to my grandmother (1925 - 2010), who passed away while I was pursuing my doctorate degree. She has always been my spiritual support, motivating me in my pursuit of higher education, career achievement, and personal integrity. I would have not reached this milestone in my life without her.

To My Grandmother (P.C. Chen)

TABLE OF CONTENTS

LIST OF FIGURES

LIST OF TABLES

LIST OF ABBREVIATIONS

ACN	Acetoneitrile
ADC	Analog-Digital Converter
BAC	Blood Alcohol Contents
CMOS	Complementary Metal-Oxide Semiconductor
CMRE	Coupling Matrix Readout Extraction
CNT	Carbon Nanotube
CPW	Coplanar Waveguide
DC	Direct Current
DSP	Digital Signal Processing
EtOH	Ethanol
GD	Group Delay
HFSS	High Frequency Structure Simulator
LTCC	Low Temperature Co-Fired Ceramic
MEMS	Micro-Electro-Mechanical Systems
MFC	Mass Flow Controller
MUT	Medium Under Test
MWCNT	Multi-Walled Carbon Nanotube
NMP	N-Methyl-2-Pyrrolidone
Op-Amp	Operational Amplifier
OV	Ohio Valley (Chemical Specialities Inc.)
PDMS	Polydimethylsolisane
PPV	poly(p-phenylene vinylene)
RF	Radio Frequency
RIE	Reactive Ion Etching
RLC	Resistance - Inductance - Capacitance
SMA	SubMiniature Version A (Connector)
SWCNT	Single-Walled Carbon Nanotube
TAC	Transdermal Alcohol Content
VNA	Vector Network Analyzer
VOC	Volatile Organic Compound

CHAPTER 1
INTRODUCTION

1.1 MOTIVATION

Biomedical monitoring systems have gradually migrated from intrusive sensing apparatuses to non-intrusive sensor designs for a wide range of safety and comfort applications. In this roadmap to achieving the ultimate ubiquitous sensing system, a collective research effort from various fields of expertise has been dedicated towards a more thorough understanding of human anatomy, the pathologies of how anatomical traits and symptoms can be effectively captured by engineered sensing systems, the technologies through which sensors can be made smaller but with superior performance, and finally, the engineering art of making such complex sensor systems on flexible materials for wearability and unobtrusiveness. This thesis aims to develop compact, low-cost, disposable, wearable sensor arrays that allow tracking of human biomarkers.

1.1.1 TRANSDERMAL BIOMARKER

In the past decades, medical research in the field of transdermal substances has revealed a wealth of correlations between human health conditions and the respective transdermal chemicals known as *Transdermal Biomarkers* [1, 2, 3]. Similar to how an individual's natural body scent is related to his / her dietary habit and the status of his / her immune system [3], our skin represents a large communication interface through which we may gain critical insights to our bodily health condition.

For example, isopropanol and related compounds were found in relatively high concentrations on the skin of all diabetes patients [2], providing an effective pathway through which non-intrusive blood-sugar monitoring can potentially be achieved. A change of body scent during female menopause is attributed to the sudden drop of estrogen in the blood, and consequently causes a change in transdermal pheromone concentration [3]. Every individual who consumes alcohol beverages would find his / her skin giving off an electronically-detectable amount of ethanol within several minutes after ingestion [4-8]. With sensor systems specifically designed to capture the presence and the concentration of these transdermal biomarkers of interest, the goal of non-intrusive body condition monitoring can be achieved.

1.1.2 POLYMERIC SENSING AND CHEMICAL SIGNATURE IDENTIFICATION

Chemical analyte detection can be done through various common methods such as chemi-capacitive detection [9, 10, 11] and chemi-resistive detection [12, 13, 14]; other exotic approaches such as mass change detection [15, 16], optical detection [17], and carbon-nanotube sensing [18] are also under rigorous research and development. However, the cost of implementing these sensing approaches on a practical sensing system varies greatly based on the cost of material and fabrication of individual sensor units. Among all of the approaches, polymeric chemi-capacitive sensing has proven to be one of the most versatile, customizable, and cost-effective solutions to achieving a low-cost, high performance 'electronic nose'.

The structures of chemi-capacitive sensors range from simple, low-cost planar interdigital configurations to more complex parallel-plate configurations, and the sensor itself can be operated in a wide range of frequencies with appropriate circuit designs. Once the sensor structure is fabricated, the *Polymeric Sensing Materials* that are responsive to certain chemical analytes of interest through changes in electrical and physical properties [19, 20] are deposited between the electrodes of the capacitor, effectively having the capacitive sensors *functionalized* [21, 22, 23] for

different analyte detections. These functional polymeric sensing materials can be obtained either from commercial vendors, or be synthesized in dedicated laboratories by attaching selected functional groups to the common carbon-based siloxane or polyaniline crystalline backbones to more specific sensing capabilities against selected target analytes [22, 23]. Most of these polymers, upon mass production, incur very low cost overhead on the sensor fabrication, while enabling the sensors to be notably more selective on analyte detection.

While numerous sensing methods are available in identifying a specific compound of interest, almost every approach, including polymeric chemi-capacitive sensing, would inevitably respond to unwanted chemicals, commonly known as *Interferents* [24]. When a sensor is exposed to an environment where target analytes and interferents are simultaneously present, the response of the sensor would be a superposition of the responses, often non-linear, to individual chemicals. Isolating the desired response from the interference is unachievable without acquiring additional information. Because of this insurmountable limitation, the identification and quantification of a specific chemical analyte is practically impossible in field applications with single-sensor system.

To address this shortcoming, multiple sensors with different sensing mechanisms towards the analyte of interest can be integrated into the sensing system known as an *Electronic Nose* [25]. The sensor array in the electronic nose generates a collection of sensor responses from individual sensors, providing distinct response patterns, known as the *Chemical Signature*, for different chemical analytes under test. Such signatures are then subject to pattern recognition algorithms such as multi-variant analysis or root-mean-square correlation analysis for analyte identification and concentration measurements. The chemi-capacitive sensor array functionalized with selected polymeric sensing materials would be the ideal candidate for such an application because of the low fabrication cost and the high specificity if properly customized.

1.1.3 RF Resonant Sensors

Resonant sensors [26, 27, 28] are known to have the advantage of response amplification when operated near their resonant frequencies. With the knowledge of the resonant frequency of a resonant sensor being inversely proportional to the square root of the inductance and the sensor capacitance [29, 30], any changes in the ambient environmental parameters can be captured by the change in sensor capacitance, which causes a shift in resonant frequency and thus a change in the resonant sensor response (i.e., S-parameters, Group Delay, Phase Delay, etc.) at an arbitrary sampling frequency close to the resonant frequency of the sensor. With a properly designed RF

resonant sensor, the change in the response can be at least one order of magnitude larger than the shift of resonant frequency of the sensor, thereby drastically improving the sensitivity of the chemi-capacitive sensor. This performance advantage is worth taking into the design consideration of the polymeric sensor array, as certain polymeric sensing materials may not yield sufficient property changes to be captured by conventional capacitive readout methods [27].

1.1.4 FLEXIBLE SUBSTRATE

Flexible electronic and microelectro-mechanical systems (MEMS) on flexible materials have become commonplace in the past decade, thanks to the well-known flexible substrate preparation process known as the Rigid-Flex process [31]. The substrate prepared by this process consists of the solid islands (i.e., the portions of the substrate that retain their original thickness and rigidity) and the flexible trench (i.e., the portions that have been thinned down through the etching process to allow localized deformation). Devices that are prone to performance degradation due to physical deformation could then be fabricated on the solid islands, thereby effectively preserving the system performance as well as its physical flexibility. For our wearable sensor array application, the Rigid-Flex substrate preparation process serves as a solid foundation for developing a novel monolithic flexible substrate preparation process specifically tailored to our fabrication and packaging requirements.

1.2 RESEARCH OBJECTIVES

The development of the wearable transdermal biomarker resonant sensor array consists of three major milestones: 1) The design and characterization of the planar and 3D polymeric RF resonant sensor structure against biomarkers of interest; 2) the fabrication and characterization of flexible polymeric RF resonant sensor array; and 3) the novel application of coupling-matrix readout extraction (CMRE) technique to accurately extract the sensor readouts from the array for post-readout multivariate pattern analysis and chemical analyte identification. Throughout the entire research, the RF sensors and sensor arrays are designed and characterized against the main biomarker analyte of gaseous ethanol as an example application of blood alcohol content (BAC) detection. In addition, selected gaseous chemical interferents are included to demonstrate the performance of the polymeric sensor array in producing distinct response patterns for different chemicals. Specifically, these gaseous interferents are acetone, methanol, benzene, and octane.

Objective 1: Design and Characterization of the Polymeric RF Resonant Sensor

In this part of research, the simple interdigital chemi-capacitive sensor is integrated with a coplanar waveguide (CPW) transmission line segment to form a single-port chemically sensitive RF resonator infrastructure. The interdigital chemi-capacitors are then functionalized through multiple coatings of selected polymeric sensing materials, allowing different resonant sensors to respond to ambient analytes differently. All the sensors are fabricated on solid glass substrates, and are tested individually against the main biomarker analyte of ethanol as well as the listed interferents. The responses of the sensors are recorded in three parameters – resonant frequency shift (Δf_0), change in response amplitude (ΔS_{11}), and change in response delay ($\Delta\text{GroupDelay}_{11}$) – through which the advantage of response amplification of the resonant sensor can be demonstrated. An RF combline-mode cavity resonant sensor can also be constructed using the same theoretical basis.

Objective 2: Fabrication and Characterization of Flexible RF Resonant Sensor Array

In this objective, the novel Frame-Flex monolithic flexible substrate preparation and packaging process is developed, and the novel single-port, multi-resonator sensor array is designed and fabricated on the Kapton-SU8 Frame-Flex flexible substrate. The fabrication process incorporates all of the mechanical advantages of the conventional Rigid-Flex substrates, while allowing polymeric sensing materials to be deposited in thick-film SU-8 pocket-confined controlled areas without the risk of deposition overflow. The SU-8 mould also offers sufficient thickness to serve the purpose of physical spacer between the polymer-coated chemi-capacitive portion of the resonant sensor and the target surface, which, in the application of biomarker detection, would be the human skin.

Objective 3: Derivation and Application of Coupling-Matrix Readout Extraction Technique

One of the main technical issues of the single-port, multi-resonator RF resonant sensor array developed in the previous objective is the prominent inter-resonator coupling that severely degrades the reliability of the readout information obtained from the array. To tackle this problem, the well-known coupling matrix model used in the RF filter synthesis procedure is customized and applied to the sensor array to capture the baseline resonant frequencies and the inter-resonator coupling coefficients of every single resonant sensor in the array. The sensor readouts from individual resonant sensors in the array can be isolated and extracted separately from the array response by recording the changes in the coupling matrix parameters. Thus, the distinct patterns of the extracted coupling matrix parameters under different gaseous analyte exposures can be used as the *Chemical Signatures* for analyte identification.

1.3 STRUCTURE OF THESIS

Chapter 2 contains a general literature review and the theoretical background related to the development of the sensor array and spans four major topics: resonant sensors, transdermal biomarkers, polymeric sensing materials, and the theory of coupling matrix model. Chapter 3 presents the design and characterization of the CPW-based single-port resonant sensor fabricated on solid substrates as the sensor prototypes. The selected polymeric sensing materials provide a sample application of ethanol detection, with ethanol, methanol, and benzene being used as the gaseous analytes for characterization. The steady-state responses, transient behaviors and selectivities of the sensors are experimentally collected as the performance characterization of the CPW-based polymeric resonant sensors. Chapter 4 presents the 3D RF combline-mode cavity resonant sensor designed under the same resonant sensor principle, and is customized to be seamlessly integrated with gas line networks for high-sensitivity gaseous chemical analyte detection. Chapter 5 first shows the development of the single-port, multi-resonator RF resonant sensor array and its CPW realization on the Kapton-SU8 Frame-Flex flexible substrate, after which the Coupling Matrix Readout Extraction (CMRE) technique is developed to represent the entire sensor array in the coupling matrix mathematical model form. The fabricated flexible sensor arrays carrying six selected polymeric sensing materials are initially subject to baseline CMRE characterization and then exposed to four different gaseous analytes: methanol, ethanol, acetone, and benzene. The variations in array responses are analyzed through the CMRE technique to yield the resonant factors (M_{ii}) as well as the inter-resonator interference factors (M_{ij}) of each sensor in the array. The resonant factors are then used as the chemical signatures of respective chemical analytes. Finally, Chapter 6 summarizes the significant contributions of this research and suggests potential future work in this research area.

CHAPTER 2
BACKGROUND INFORMATION

2.1 INTRODUCTION

This chapter provides a general overview of the prerequisite background fields of knowledge and the relevant literature for the development of the wearable RF resonant sensor array. The discussions in this chapter also cover the state-of-the-art technologies to which the performances of our novel sensor array designs are compared.

Section 2.1 contains the review of the state-of-the-art gaseous VOC (volatile organic compound) chemical sensor technologies, the existing resonant sensor designs, and the use of sensor arrays for various engineering applications. The performance parameters as well as the respective shortcomings of the existing common gaseous sensing technologies will be used towards calibrating the performance of our sensors and sensor arrays under testing. Section 2.2 covers a brief overview of some of the common transdermal biomarker chemicals detectable on the surface of human skin, and the evident correlations of the transdermal analyte concentration and the respective analyte concentration in the human blood circulation system. This section focuses on the transdermal

ethanol contents, as the sensors and sensor arrays presented in this thesis are designed towards a sample application of blood alcohol contents monitoring through transdermal biomarker detection. Finally, section 2.3 gives a general overview of the sorption mechanism and electrical properties under exposure to gaseous analytes, and provides a foundation for the more detailed discussion on the customizability of polyaniline-based crystalline sensing materials in Chapter 3.

2.1 CHEMICAL SENSORS, RESONANT SENSORS, AND SENSOR ARRAY

2.1.1 Chemi-Capacitive Sensors

Chemi-capacitive sensors detect changes in ambient environmental parameters through capacitance transduction. The variation in capacitance can be read out through the conventional DC readout circuit, as shown in Figure 2.1.1, where the voltage output of the operational amplifier is linearly proportional to the sensor capacitance at the negative input.

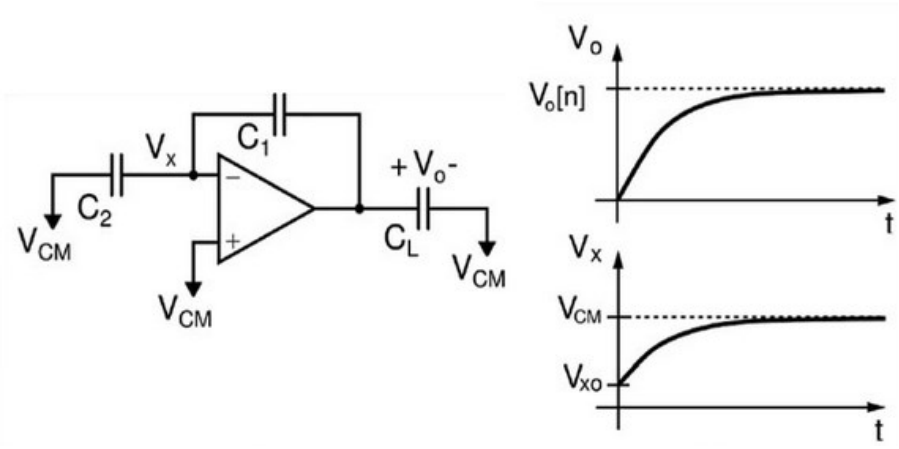

Figure 2.1.1: Traditional pipeline analog to digital conversion stage with op-amp implementation [32].

Alternatively, the sensor can also be connected in a series- or shunt-RLC circuit to form a resonant sensor configuration, as shown in Figure 2.1.2. The readout of the circuit can be achieved by exciting the circuit with a monotonic oscillating voltage at a frequency near the resonant frequency, f_0, of the circuit, followed by tracking the amplitude of the wave, which is proportionally affected by the change in sensor capacitance. This configuration is also the fundamental mechanism behind the RF resonant sensor, which will be discussed in the next section.

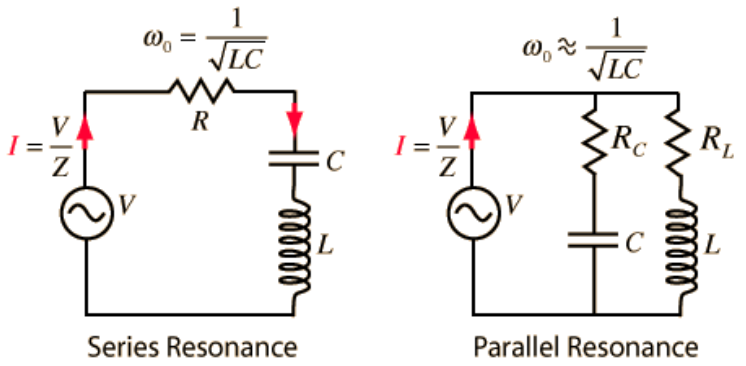

Figure 2.1.2: Series and parallel RLC resonator circuits [33].

As shown in Figure 2.1.3, chemi-capacitive sensors are commonly found in two structures: parallel-plate and planar interdigital. The two electrodes and the medium in between forms a capacitor; by replacing the medium with different chemically-sensitive materials, the chemi-capacitor can be functionalized towards detecting changes in specific sets of environmental parameters. Such functionalization is often done with polymeric sensing materials [34] or porous ceramic sensing materials [35], both of which would undergo changes in dielectric constants (ε_r) or physical volume or both simultaneously, thereby changing the capacitance of the sensor altogether.

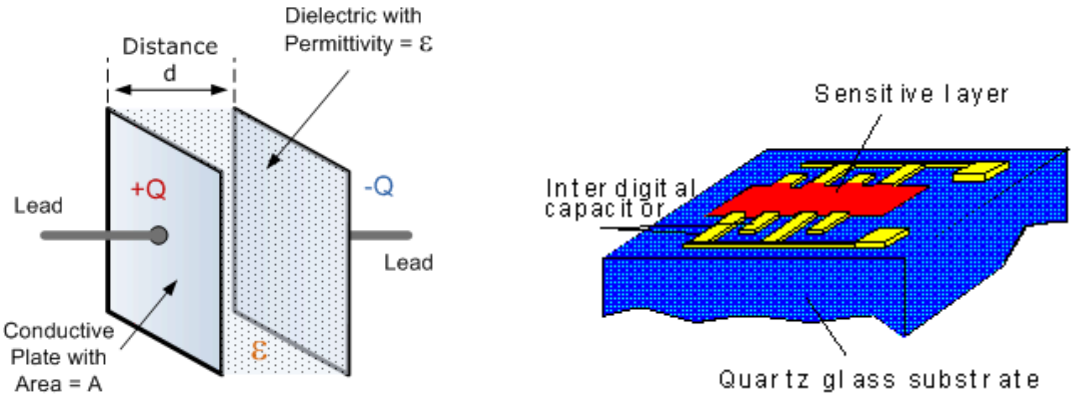

Figure 2.1.3: Parallel plate chemi-capacitor (left) and interdigital chemi-capacitor (right) [9, 36].

The structure shown in Figure 2.1.4 is a parallel-plate chemi-capacitor fabricated with the PolyMUMPs foundry process. The top plate of the capacitor is designed with a large fill-hole where the sensing materials can be deposited in between the plates. The release holes are also used as vent holes to allow the sensing material to be exposed to the chemical analytes in the air.

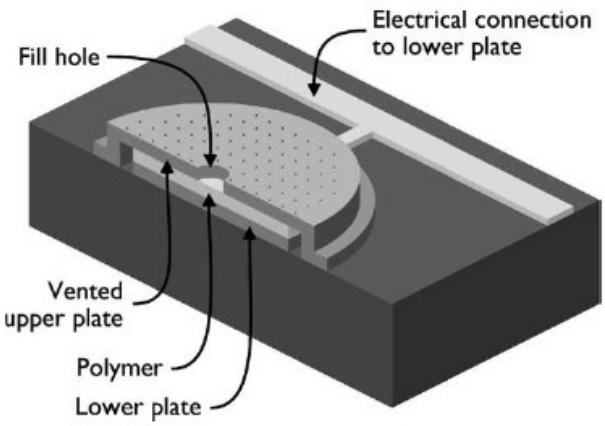

Figure 2.1.4: PolyMUMPs-based parallel plate chemi-capacitor with vent holes and fill-holes [10].

The readout circuit similar to the one illustrated in Figure 2.1.1 has been constructed in [10] to provide sensor readouts from individual sensors functionalized with different sensing materials to the post-readout analysis system, as illustrated in Figure 2.1.5.

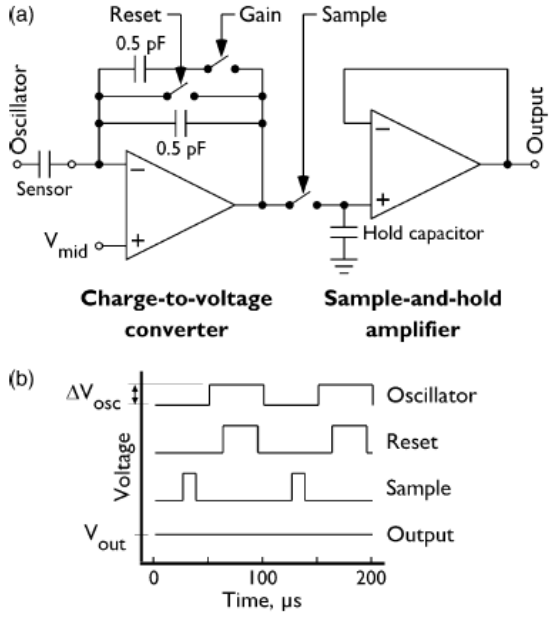

Figure 2.1.5: Op-amp-based readout circuit [10].

Chemi-capacitive sensors have also been used in the biosensing applications for its customizability towards specific groups of analytes. The sensor illustrated in Figure 2.1.6 is the planar interdigital chemi-capacitive sensor, of which the impedance (Z_o) of the sensor is used as the readout parameter. The sensor impedance is another representation of the sensor capacitance with the parasitic

resistive elements and other frequency-selective reactive effect taken into account. When the analytes occupy the bonding site of the sensing material, the dielectric constant of the sensing material changes. This affects both the electric field distribution around the electrode fingers and the impedance of the entire chemi-capacitive sensor.

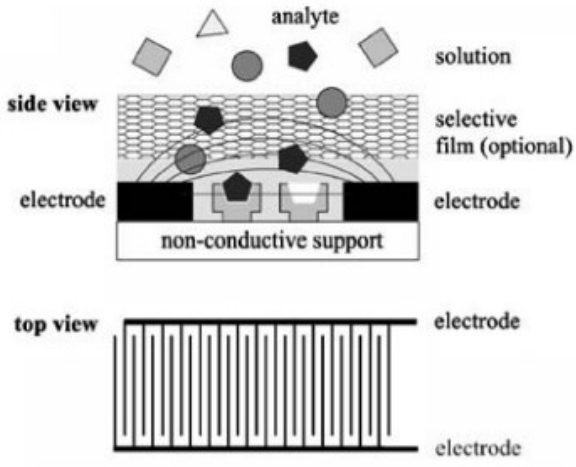

Figure 2.1.6: Interdigital chemi-capacitive biosensor with impedance readout [11].

2.1.2 Chemi-Resistive Sensors

The second class of common chemical sensor design is the chemi-resistive sensor, also known as the conductometric sensor [12]. As the sensing element is exposed to target analytes, the resistance of the sensing material changes proportionally, thus providing a readout mechanism compatible with most of the readout circuits operated at DC and low-frequency ranges. As illustrated in Figure 2.1.7, the readout can be obtained by applying a constant voltage across the chemi-resistive sensing material and monitoring the output current. Here, a constant current input with voltage readout would also work.

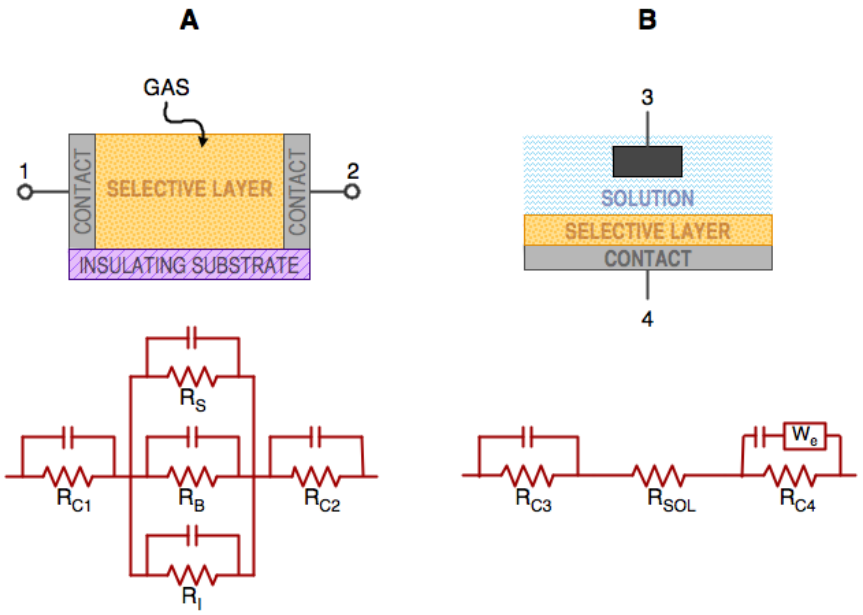

Figure 2.1.7: Conductometric sensor models [37].

Chemi-resistive materials are often found in two major categories: chemi-conductive polymer and chemo-resistive metals. Figure 2.1.8 illustrates a chemi-resistive sensor with interdigital electrodes on which the chemi-resistive polymer is applied. The resistance thermometer is added to help achieve thermal compensation.

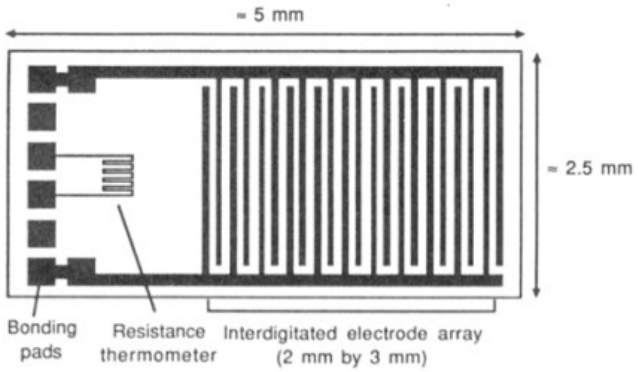

Figure 2.1.8: Interdigitated chemi-capacitive sensor with thermal compensation element [13].

In biosensing applications, chemi-resistive material can be the solution containing the analytes of interest, provided that the solution itself is conductive and the analytes would not suffer damage from electrical current. Figure 2.1.9 shows the platinum-based chemi-resistive sensor where the

enzyme-containing solution is directly applied on top of the two electrodes. In this instance, the electrical readout would reflect the enzyme concentration in the solution.

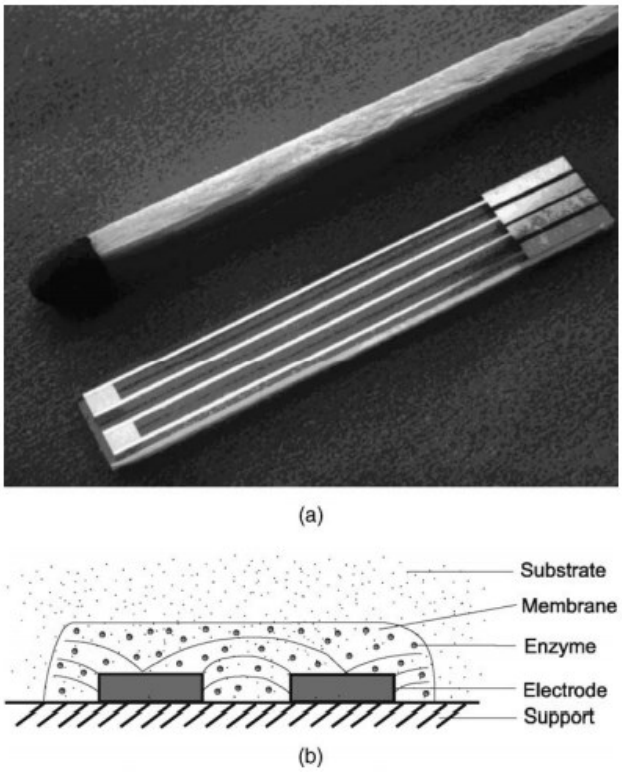

Figure 2.1.9: Platinum-based interdigitated conductometric enzymic biosensor [14].

Platinum is also an ideal sensing element for gaseous ethanol detection. The well-known DART sensor [38] implements a platinum-based fuel-cell inside the sensing chamber, whereby as the ethanol gas is injected into the sensing chamber, the proprietary electrolyte in the fuel cell absorbs the ethanol molecules and result in change in resistivity. Figure 2.1.10 illustrates the DART sensor operation principles.

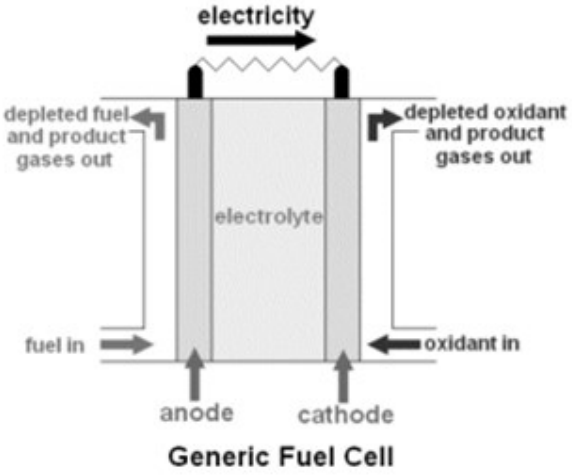

Figure 2.1.10: Generic fuel cell diagram with alcohol as the oxidant [39].

Figure 2.1.11 illustrates a chemi-resistive sensor where the chemi-resistive polymeric sensing material (PPV: poly(*p*-phenylene vinylene)) is deposited between the two aluminum electrodes. The water droplet is applied in the silicone pocket, and the resistivity of the PPV changes with respect to the pH level of the water droplet.

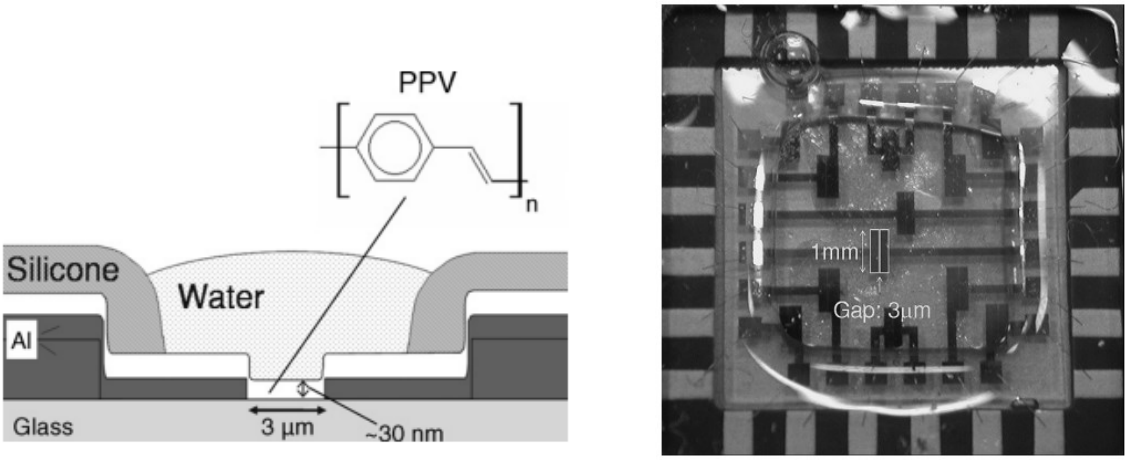

Figure 2.1.11: PPV-based liquid pH level chemi-resistive sensor [40].

2.1.3 Other Chemical Sensors

While their usage may be limited, some other chemical sensors have also seen their applications in research and laboratory purposes. Carbon-nanotube-based (CNT-based) sensors have been a popular research topic in the past decade, during which the single-wall CNT (SWCNT) was found to

be a great chemi-resistive material that can react to different gaseous and aqueous analytes with various levels of resistivity. With their miniscule size, CNTs can be grown or deposited onto the transistor as the conductive channel, thereby enabling the CMOS-CNT-based transistor to sense the presence of chemical analytes. Multi-wall CNTs (MWCNTs) have also been found to exhibit chemi-resistive sensing properties at a significantly lower level; however, high current treatments [18] were found to be highly effective in improving their sensing capability. The improvement was due to the damage introduced by the high current to the outer walls of the MWCNT, resulting in partial exposure of the innermost CNT wall, which has similar chemical sensing properties as the SWCNT. However, most CNT-based transistors are still using the SWCNT despite the significantly lower cost of fabricating MWCNT. Figure 2.1.12 shows the implementation of the CMOS-CNT chemical sensing transistor.

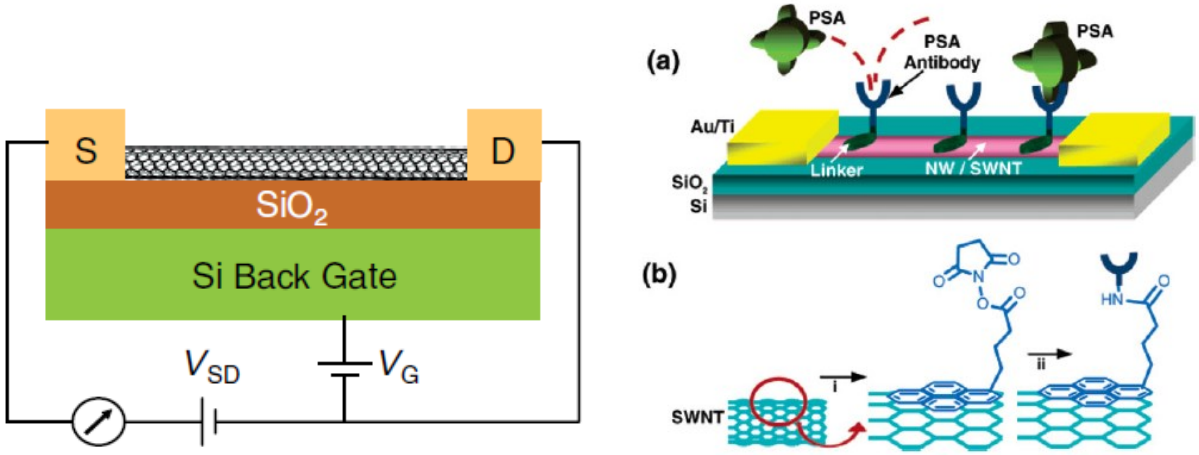

Figure 2.1.12: CNT-based chemical sensing transistor for antibody biosensing applications [18].

While most of the chemical sensing techniques are electric-property based, some novel sensor designs are mechanical- and opti-mechanical-based. Most of these sensing techniques are still in the early research stage or limited to in-lab use, but some of these sensor designs have reported down to ppt-range detection with chemi-sorbent polymeric sensing materials that have never been able to produce the same level of sensitivity when applied in chemi-capacitive or chemi-resistive configurations. Figure 2.1.13 illustrates the MEMS cantilever chemical sensor with the polymeric sensing material placed on the proof mass of the cantilever. As the analyte molecules get absorbed into the polymer, the total mass of the polymer drop increases, leading to mechanical reactions of the cantilever.

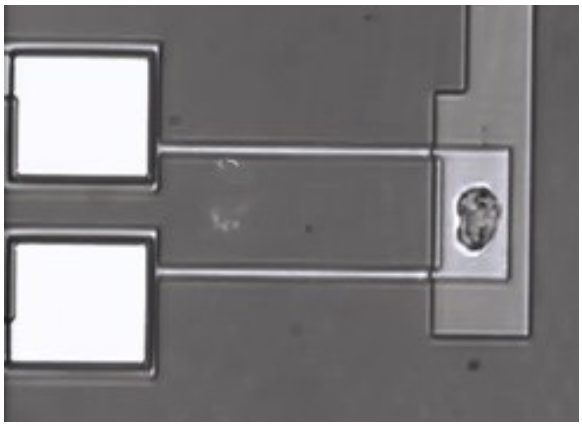

Figure 2.1.13: MEMS cantilever-based polymeric mass sorption chemical sensor [15].

The readout mechanism of the mass-based chemical sensor can be electrostatic, piezo-resistive, or optical. Figure 2.1.14 illustrates the circuit representation of the capacitive readout configuration of a cantilever chemical sensor.

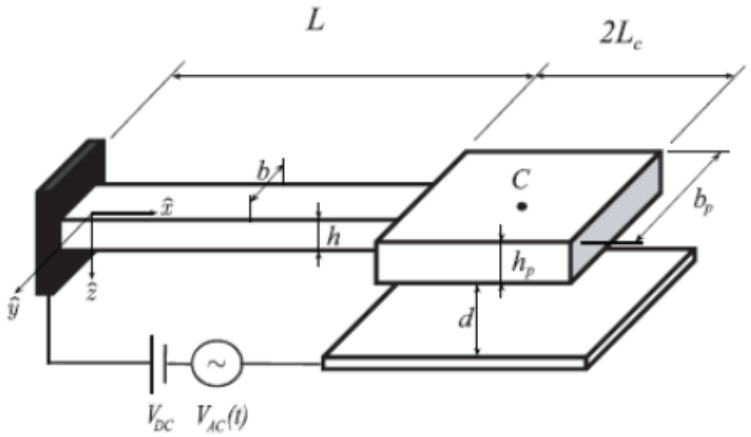

Figure 2.1.14: Electrostatic readout concept for the MEMS cantilever-based chemical sensor [16].

Lastly, Figure 2.1.15 illustrates the optical readout mechanism, where the bending of the cantilever due to the increase in polymer mass is measured by optical laser.

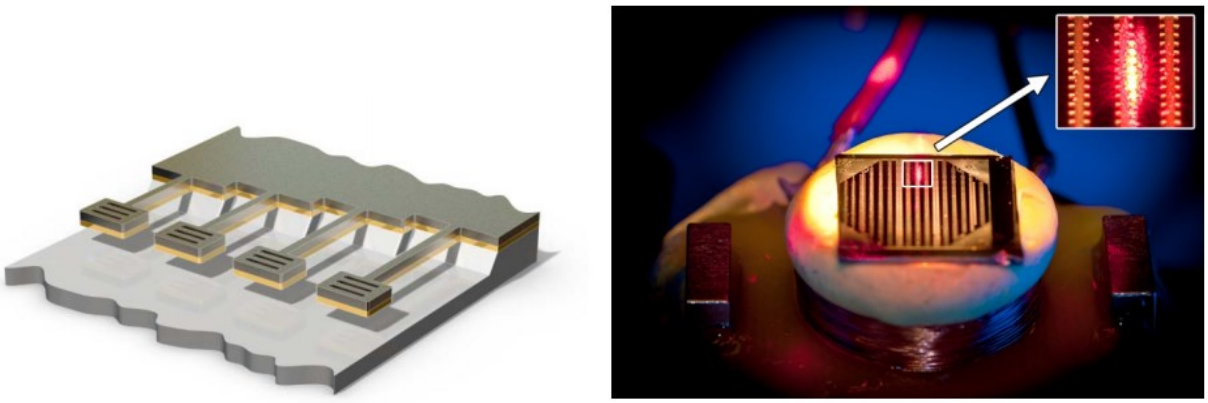

Figure 2.1.15: MEMS cantilever sensor array with laser array interferometric readout [17].

The electrostatic and piezo-electric mass sensors can both be operated in static and dynamic mode. In static mode, the sensor readout is measured in terms of the amount of deflection seen at the tip of the cantilever. In dynamic mode, the cantilever is driven by a periodic voltage excitation at its natural fundamental mode resonant frequency; any changes in mass at the cantilever tip would lead to a shift in mechanical resonant frequency. In general, the sensitivity of the sensor is at least one magnitude higher when operated in dynamic mode compared to that in static mode [26]. This effect of dynamic amplification is also applicable for RF resonant sensors.

2.1.4 Resonant Sensor

As described in previous sections, the concept of resonant sensor is to operate the sensing element or the entire sensor in the vicinity of its resonant frequencies, thereby exploiting the advantage of dynamic response amplification in order to improve the sensitivity of the sensor by at least one order of magnitude. The circuit model of an RF resonant sensor is illustrated in Figure 2.1.2, and the operation principle is illustrated in Figure 2.1.16.

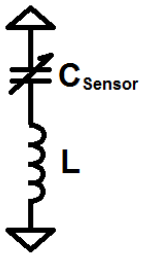

$$f_{0\ sensor} = \frac{1}{2\pi\sqrt{LC_{sensor}}}$$

Figure 2.1.16: Circuit model of an RF resonant sensor.

Considering Figure 2.1.16, a single-port RF resonator would have a similar reflection coefficient curve (S_{11}) at its centre frequency (f_0), which is dependent on the design dimensions. The depth and the width of the curve near resonance is a dimension-dependant and material loss-dependant behavior related to the quality factor (Q) and the loading of the resonator, which will be discussed in detail in Chapter 3. Based on the model in Figure 2.1.2, a shift in f_0 takes place whenever the reactance of the system changes. Furthermore, and as far as the resonant sensor with chemi-capacitive sensing element is concerned, a change in capacitance (ΔC_S) due to analyte exposure would inadvertently introduce a Δf_0. The magnitude of Δf_0 is dictated by the equation shown in Figure 2.1.2. Because of the inverse square-root relationship between f_0 and C_S, the change in C_S due to analyte exposure would translate into an even smaller centre frequency shift, which is undesirable in sensor applications.

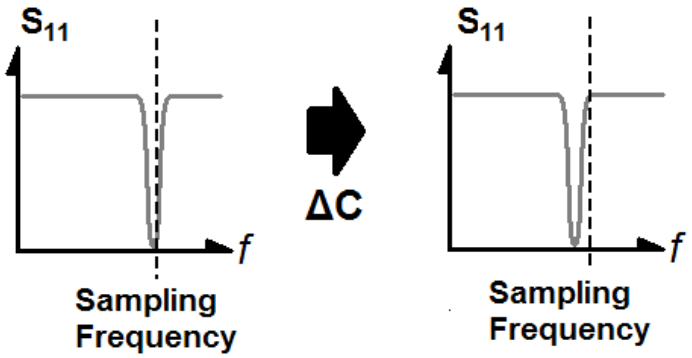

Figure 2.1.17: RF sensor readout in amplitude response (S_{11}) instead of centre frequency (f_0).

However, as illustrated in Figure 2.1.17, if the readout of the sensor is not taken with respect to Δf_0 but to the change in response amplitude (ΔS_{11}) instead, the small Δf_0 would translate into a large ΔS_{11}, thus providing a drastic improvement in the sensitivity of the sensor. The high sensitivity of S_{11} near the centre frequency of a resonator was well-studied in [29], and the sharper the dip of the S_{11} curve at f_0, the more significant the sensitivity improvement.

The concept of an RF resonant sensor was first patented in 1999 for wireless device integration [27, 28], followed by various works done in the performance improvement of resonant sensors design and the adaption of resonant sensors in various fields of application [41, 42]. In terms of performance improvement, the effort was mainly put to the adaption of RF resonant structures with higher quality factors and tuneable capacitive elements, which can be replaced with environment-sensitive sensing elements. Figure 2.1.18 illustrates an RF resonant air-flow detection sensor, implemented with the high-Q combline cavity filter capacitively loaded with elastic copper-coated

PDMS membrane and an attached air flow sensing beam. As the sensor experiences changes in air flow, the beam and membrane undergo deformation, leading to changes in the capacitances loading the resonators and, ultimately, changes in the insertion and return loss characteristics of the filter to achieve the flow detection purpose [43].

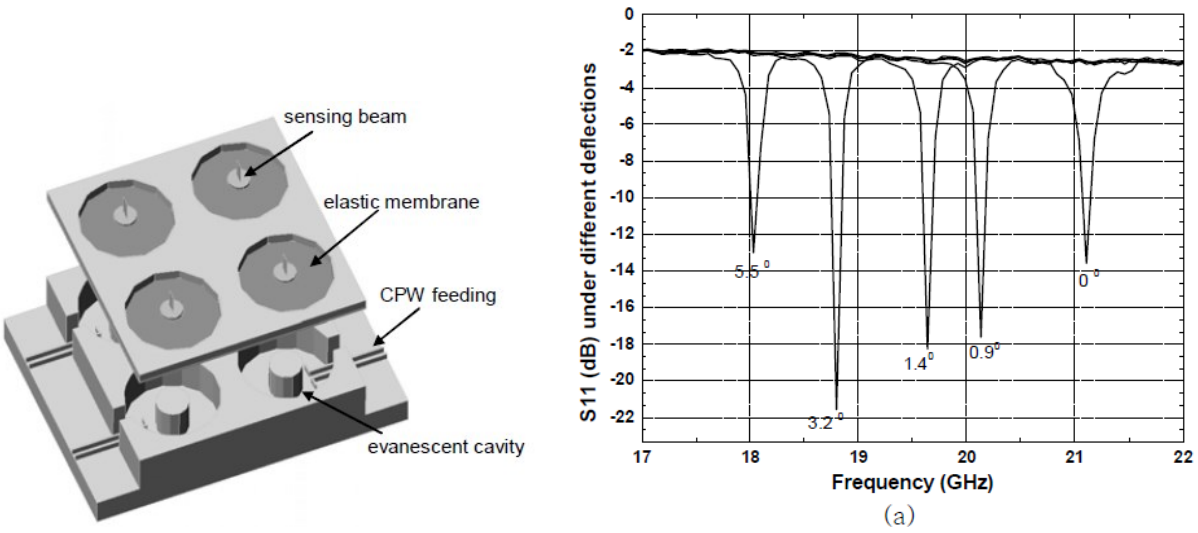

Figure 2.1.18: RF resonant cavity-based air flow sensor [43].

Figure 2.1.19 illustrates a liquid analyte concentration sensor implemented with an RF cavity resonator. The structure operates at 1.875 GHz and has seen a change in insertion loss in the range of -10 dB as the concentration of the solution in the cavity changes. However, due to the lossiness of the solution, the sensor is not capable of producing a strong signal. The insertion loss observed during sensor operations ranges between -25 dB and -40 dB.

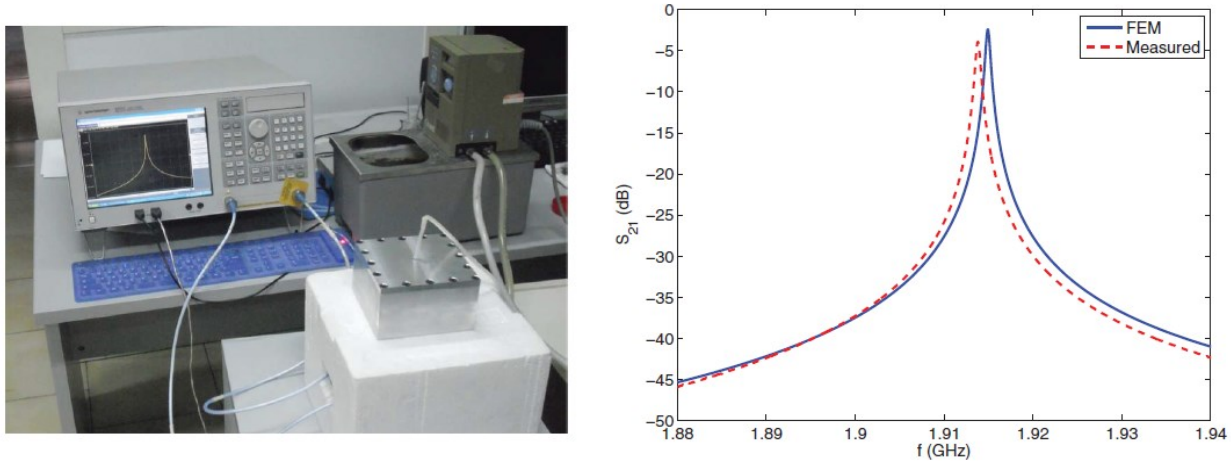

Figure 2.1.19: Liquid concentration sensor implemented with RF cavity resonator [44].

Figure 2.1.20 shows a LTCC-based wireless embedded resonant pressure sensor. The top and bottom membranes of the laminated pressure sensor carry two electrodes, allowing the pressure sensor to be operated as a pressure-controlled capacitor. Once again, the sensor is then connected to an inductive antenna coil with intrinsic parasite resistance, effectively forming the RLC resonant circuit illustrated in Figure 2.1.2. Then, as illustrated in Figure 2.1.21, the sensor is connected to an inductively coupled wireless readout circuit to provide a readout pathway.

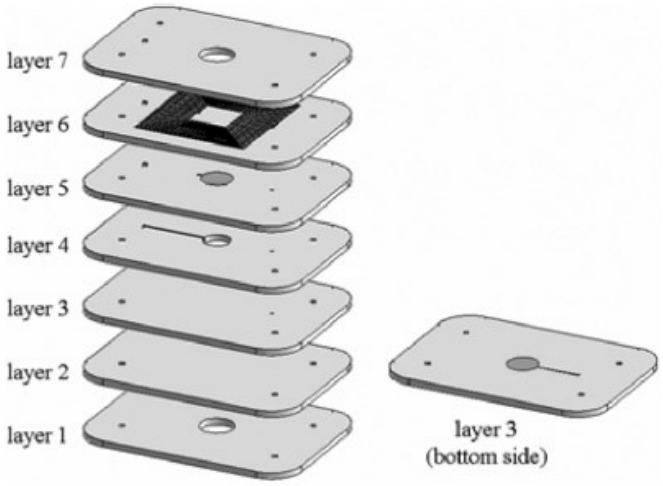

Fig. 1. Exploded 3D view of sensor model.

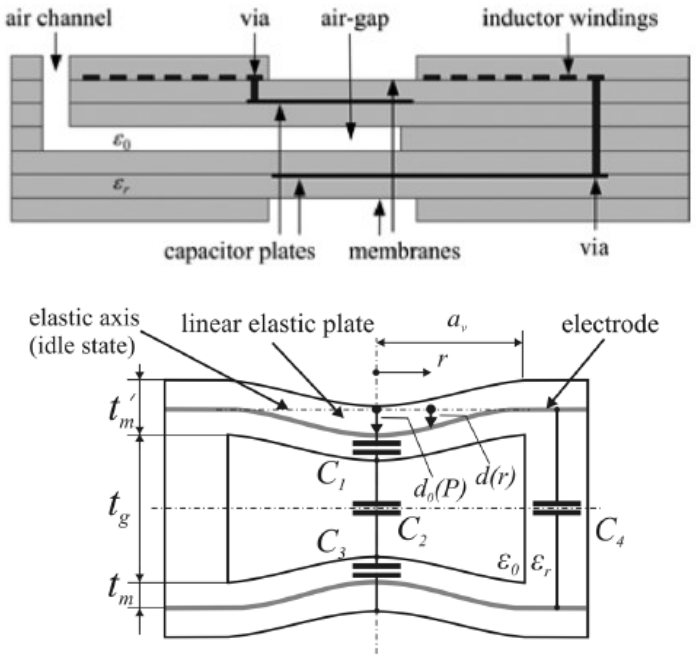

Figure 2.1.20: Design and fabrication of an LTCC-based resonant pressure sensor [45].

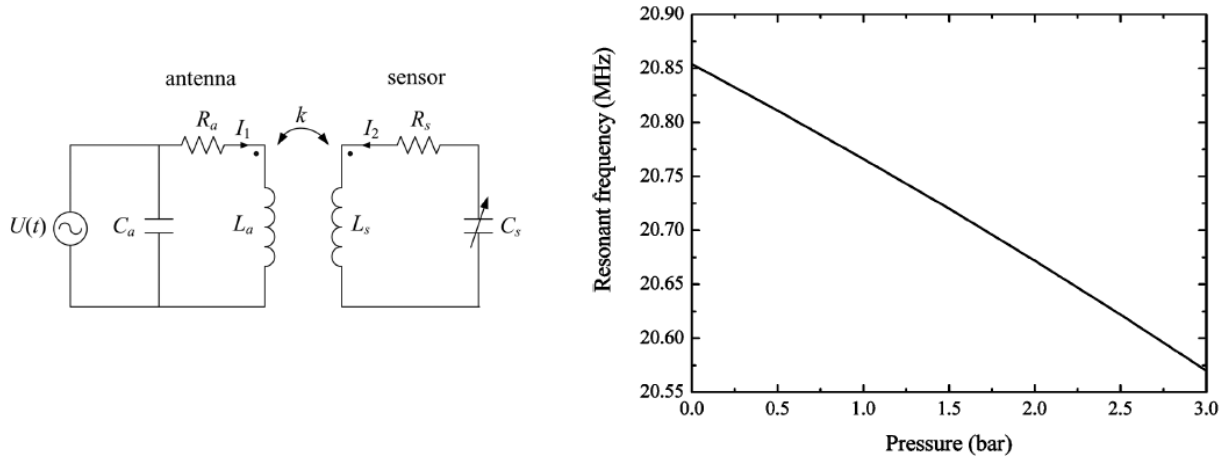

Figure 2.1.21: Inductive readout circuit model and the frequency response of the pressure sensor [44].

Lastly, the structure illustrated in Figure 2.1.22 is a moisture content sensor implemented with a planar microstrip resonator on a partial defected ground, allowing part of the electric field to see the material underneath the ground plate for sensing purpose. The material underneath the microstrip substrate showed significant changes in effective dielectric constant. Furthermore, with the square cutaway on the ground plane of the microstrip substrate, the resonator was capable of capturing the change with a reported Δf_0 in the range of 20 ~ 30 MHz at the f_0 of 600 MHz.

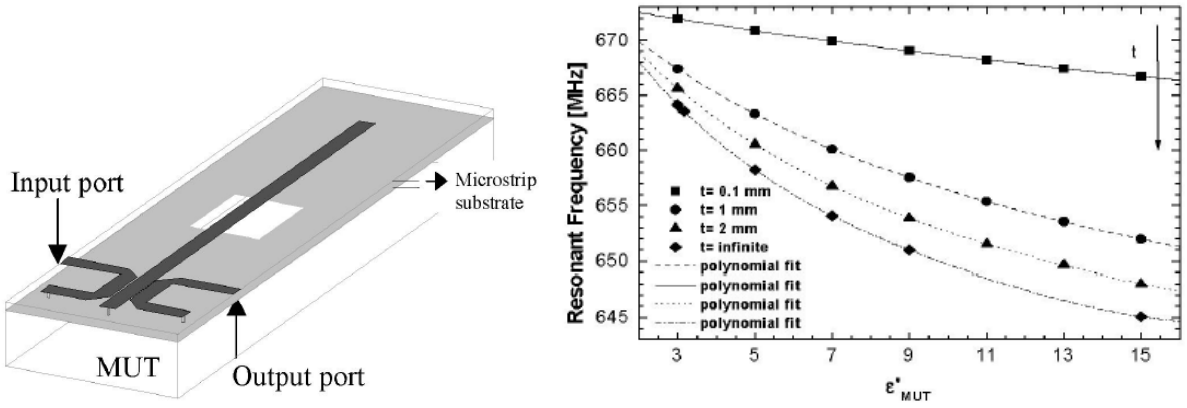

Figure 2.1.22: Moisture sensor implemented with defected-ground microstrip RF resonator [45].

2.1.5 Sensor Arrays

While individual sensors may have superior performance against specific groups of analytes, there is a general lack of sensing material that is responsive against one specific analyte of interest. The issue with analyte interference has been a major engineering barrier that prevents many sensors to reach their commercialization stage due to their lack of selectivity against certain analytes from a certain collection of interferents, which are often the chemical molecules with similar molecular structures as the target analyte.

As a result, for a chemical sensing device to fully capture the ambient parameters without ambiguity, multiple sensors must be brought together to form a sensor array (also known as an electronic nose illustrated in Figure 2.1.23) to help distinguish specific interferents from the analyte of interest. These individual sensors often have very different transient and steady-state response characteristics against the same analyte, and thus would be able to produce a response pattern for every analyte. This response pattern is known as the *Chemical Signature*, and should ideally be unique for all analytes that may come in contact with the sensor system [46].

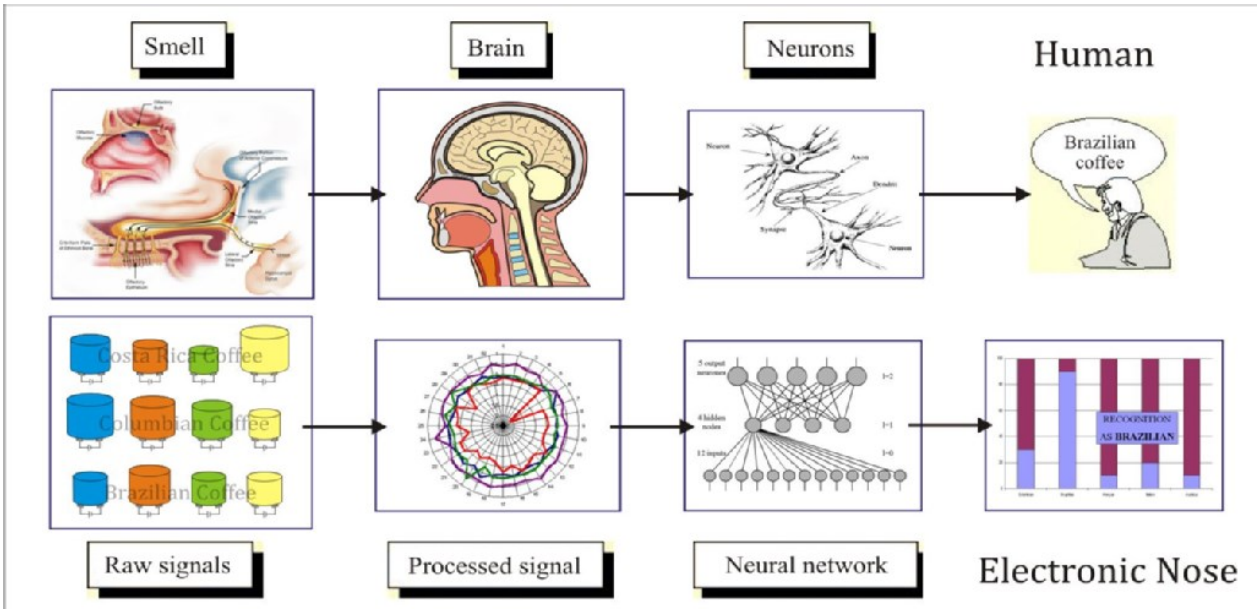

Figure 2.1.23: General concept of electronic nose implementing sensor array and pattern analysis [46].

Figure 2.1.24 illustrates the block diagrams of the conventional sensor systems implementing an array of different sensors. In parallel sampling configuration (left), the readout of each sensor is captured by its dedicated analog-to-digital converter (ADC), from which the digitized readout is sent to the data processing unit for post-readout analysis. In series configuration, the data processing

unit possesses only one ADC, which is sequentially switched across the entire sensor array to obtain the sensor readouts individually for data analysis.

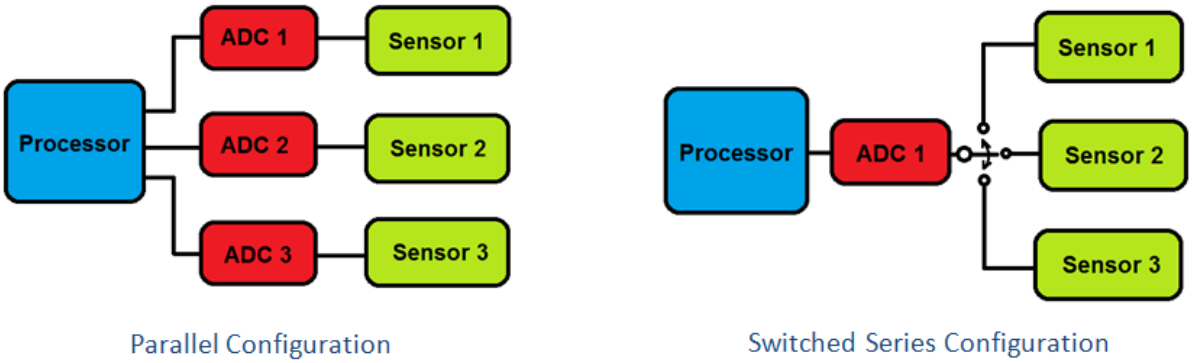

Figure 2.1.24: Parallel (left) and series (right) sensor readout configurations.

Figure 2-1-25 illustrates another application of sensor array to allow uniform sampling coverage across a large area of the sample. The array of resonant sensors is placed on top of the Nafion polymer film that is responsive against various chemical analytes present in the environment chamber. The sensors would see changes in characteristic impedance (Z_0) as the electrical properties of the Nafion film changes. When the readouts are required, an array of readout coils are brought in close vicinity of the array, and the responses of all the resonant sensors are individually captured through inductive coupling to the reader array, thereby providing a series of sensor readouts of the same sample under test from different locations around the testing chamber. Figure 2.1.26 indicates that the array is capable of detecting the presence of water, ethanol (EtOH), and acetonitrile (ACN).

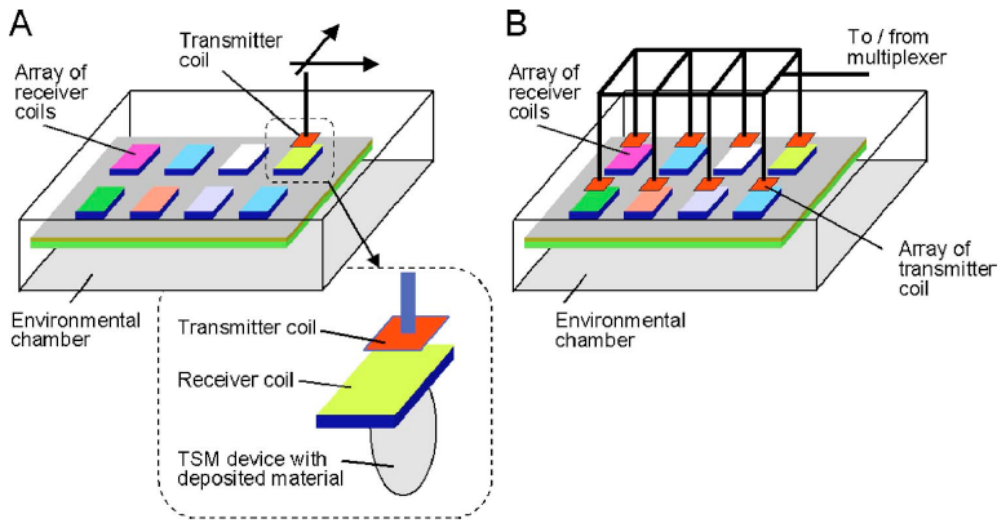

Figure 2.1.25: Wireless resonant sensor array on Nafion film with uniform environmental monitoring [46].

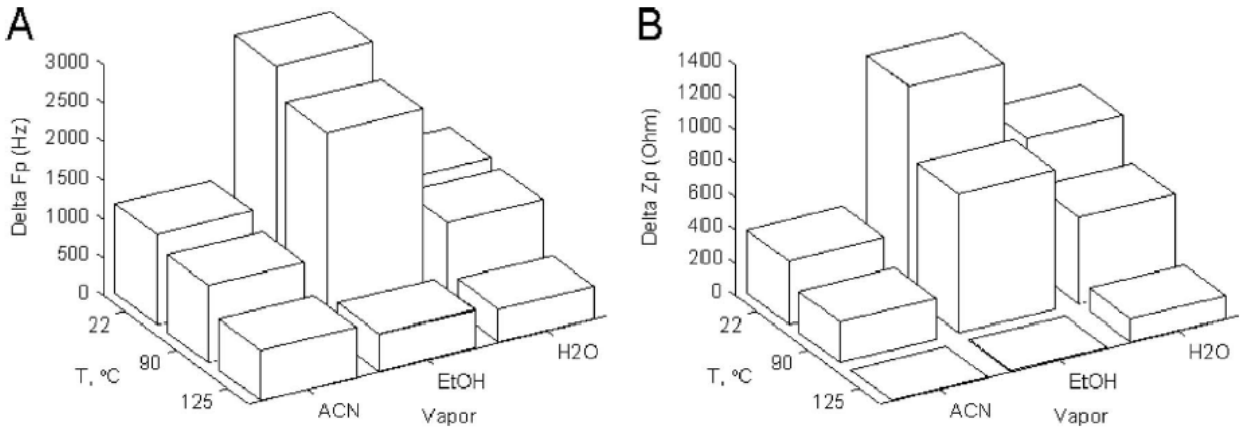

Figure 2.1.26: Response patterns of H_2O, EtOH, and ACN under Nafion resonant sensor array [46].

2.1.6 Sensor Performance Characterization

In order to fully characterize the sensor for future array and system integration, the following performance characteristic parameters [47] are introduced and will be used for sensor performance analysis.

A. Sensitivity

The baselines of the readout parameter of an RF resonant sensor at a given operation frequency can drastically vary based on the loaded Q of the sensor and the quality of the deposited polymeric

sensing material. As a result, the sensitivity of the sensor must be characterized by the relative percentage change in the response magnitude from the baseline. This normalization of the sensor output is used to compare different sensing materials.

B. Selectivity

With ethanol as the analyte of interest, the selectivity of the polymeric resonant sensor is quantized with Eq. 2.1 to measure the capability of the sensor in differentiating ethanol from other sample interferents through the sensor readout.

$$Selectivity = \frac{Ethanol\ \%\ Response}{Interferent\ \%\ Response} \tag{2.1}$$

C. Response and Recovery Time

The response time, $\mathbf{t_r}$, is measured in terms of the time for the sensor response to change from 10% to 90% of its projected steady-state response level upon analyte exposure, and the recovery time, $\mathbf{t_d}$, is measured in identical standard upon removal of analyte exposure. In addition, the response time constant, $\mathbf{t_c}$, is defined as the time the sensor takes to reach 70% of the projected steady-state response level [48]. These three parameters are used to capture the transient response characteristics of the resonant sensor.

D. Chemical Signatures

For future system integration purposes, the responses of the sensors carrying different polymeric sensing materials under the same gaseous analyte exposure can be reviewed together to determine a characteristic response pattern for the specific analyte. This pattern is defined as the chemical signature of the analyte on the polymeric resonant sensor group.

2.2 ETHANOL AS TRANSDERMAL BIOMARKER CHEMICALS

While numerous transdermal biomarkers have been found with correlations with the bodily condition of a human being, this part of the literature review will mainly focus on the presence of transdermal alcohol contents (TAC) and its correlation with blood alcohol content (BAC).

TAC has been known to exist since the early 1930s [4], and numerous research on the biological pathways of TAC emission from human skin and its correlation with BAC has been undertaken over the past three decades. With the invention of the transdermal alcohol sensing bracelet [4] in the

1980s, more thorough studies have been carried out to establish a solid relationship between TAC and BAC. As illustrated in Figure 2.2.1, early results have indicated that the transient behaviors of BAC and TAC resemble each other, with the response time of TAC slower than that of BAC by an average of 2.5 hours, and the recovery time of TAC 5.8 hours slower than that of BAC [5].

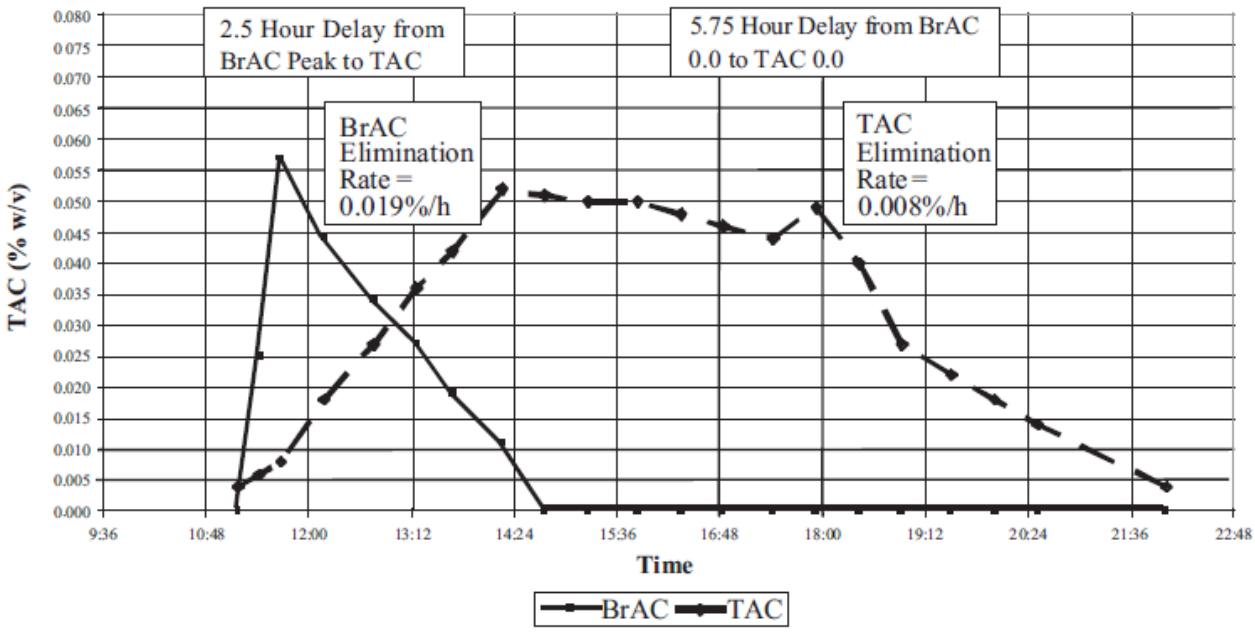

Figure 2.2.1: Transient response curves of BAC and TAC [5].

However, in the past decade, with the advancement of transdermal sensing technology, it was discovered that the peaking time of TAC lags behind that of BAC at an average of 30 minutes [6] to 1 hour [7], as illustrated in Figure 2.2.2, and that the onset of the TAC rising trend starts as quickly as 3 minutes after the intake of alcohol [1, 8], as illustrated in Figure 2.2.3. It was therefore concluded [2, 3] that TAC is a valid and useful biomarker to track BAC levels for medical or legislative purposes. However, the minimum required detection level of the TAC concentration for the BAC monitor application is currently held as the proprietary information by our industry collaborator, and therefore will not be disclosed in this thesis. The results presented in this thesis pertains to only ethanol concentration levels above 500ppm.

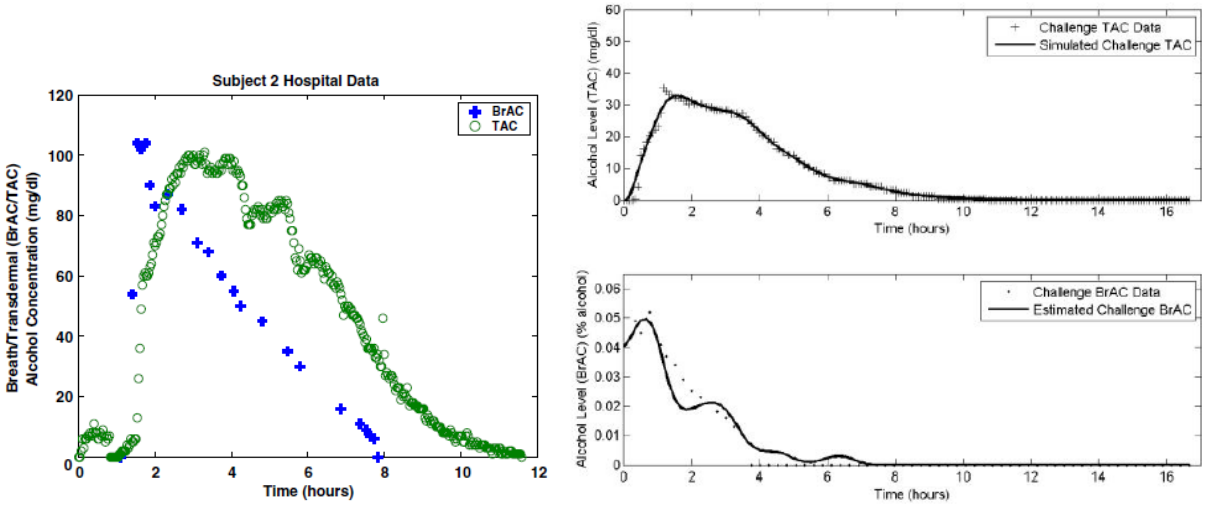

Figure 2.2.2: Response delay examples between BAC and TAC [6 (right), 7 (left)].

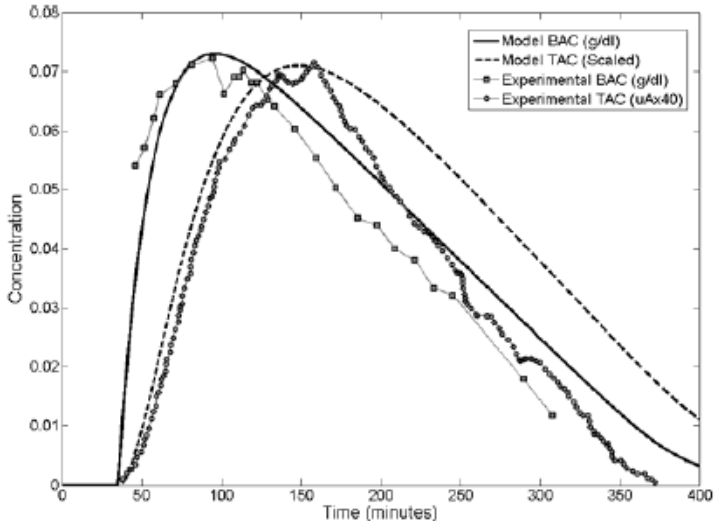

Figure 2.2.3: BAC and TAC transient curves illustrating 3-minute TAC response onset after onset of BAC increase [1].

Ethanol, however, is not the only transdermal biomarker that can be detected on the skin surface. Hundreds of different organic and non-organic analytes can be found on human skin, many of which are volatile organic compounds (VOC) that may directly interact with sensing materials. For example, for patients suffering diabetic ketoacidosis, isopropyl alcohol has been found as a transdermal biomarker [2]. Since isopropanol and ethanol are both alcohol, differentiating TAC from transdermal isopropanol contents would require careful sensor system design. Another example is the common odor compound nonanal (also known as nonanaldehyde or Aldehyde C-9), a transdermal human metabolism by-product that attracts mosquitoes. The amount of transdermal

nonanal compounds produced by the human body is related to dietary habit and genetic reasons [3]. Table 2.2.1 presents a collection of selected transdermal chemical species that can be found on human skin [3].

Table 2.2.1: Selected Transdermal Chemical Species Found on Human Skin (VOC Highlighted in Yellow) [3]

Peak No.	Volatile Organic Chemicals (VOCs)			
	Person A	***Person B***	***Person C***	***Person D***
1	Cyclopentasiloxane, decamethyl-	Cyclopentasiloxane, decamethyl-	Cyclopentasiloxane, decamethyl-	Cyclopentasiloxane, decamethyl-
2	D-Limonene	2-Propanol, 1-methoxy-	Dodecane	Dodecane
3	Dodecane, 4,6-dimethyl-	D-Limonene	D-Limonene	D-Limonene
4	Cyclohexasiloxane, dodecamethyl-	Dodecane, 4,6-dimethyl-	Dodecane, 4,6-dimethyl-	Dodecane, 4,6-dimethyl-
5	Hexadecane	Cyclohexasiloxane, dodecamethyl-	Cyclohexasiloxane, dodecamethyl-	Cyclohexasiloxane, dodecamethyl-
6	1-Heptanol, 2,4-diethyl-	Pentadecane	1-Undecene, 7-methyl-	Dodecane, 4,6-dimethyl-
7	2-Isopropyl-5-methyl-1-heptanol	2-Isopropyl-5-methyl-1-heptanol	2-Isopropyl-5-methyl-1-heptanol	1-Undecene, 7-methyl-
8	Tetradecane	Heneicosyl heptafluorobutyrate	5-Hepten-2-one, 6-methyl-	2-Isopropyl-5-methyl-1-heptanol
9	Cycloheptasiloxane, tetradecamethyl-	Tetradecane	Tetradecane	5-Hepten-2-one, 6-methyl-
10	Ethanol, 2-butoxy-	Cycloheptasiloxane, tetradecamethyl-	Cycloheptasiloxane, tetradecamethyl-	Tetradecane
11	Heneicosane	Ethanol, 2-butoxy-	Ethanol, 2-butoxy-	Nonanal
12	Trichloroacetic acid, 2-ethylhexyl ester	Eicosane	Heptadecane	Ethanol, 2-butoxy-
13	Acetic acid	Formamide, N,N-diethyl-	Formamide, N,N-diethyl-	Eicosane
14	2-Propenoic acid, 2-ethylhexyl ester	Acetic acid	2-Propenoic acid, 2-ethylhexyl ester	Formamide, N,N-diethyl-
15	1-Hexanol, 2-ethyl-	2-Propenoic acid, 2-ethylhexyl ester	1-Hexanol, 2-ethyl-	2-Propenoic acid, 2-ethylhexyl ester
16	2-Propanol, 1-(2-methoxypropoxy)-	1-Hexanol, 2-ethyl-	Benzaldehyde	1-Hexanol, 2-ethyl-
17	Cyclooctasiloxane, hexadecamethyl-	Cyclooctasiloxane, hexadecamethyl-	4-Cyanocyclohexene	2-Propanol, 1-(2-methoxypropoxy)-
18	4-Cyanocyclohexene	4-Cyanocyclohexene	Hexadecane	Benzaldehyde
19	Octadecane	Octadecane	3-(2-Methoxymethoxy ethylidene)-2,2 dimethylbicyclo[2.2.1]heptane	4-Cyanocyclohexene
20	(-)-Isolongifolol, acetate	3-Methoxymethoxy-6,6 dimethyl-2-methylene-bicyclo[3.1.1]heptane	Butanoic acid	Hexadecane
21	Cyclohexanol, 5-methyl-2-(1-methylethyl) (1.alpha. 2. beta., 5.alpha.)-(.+/-.)-	Cyclohexanol, 5-methyl-2-(1-methylethyl)-, [1S-(1.alpha. 2. alpha., 5.beta.)]-	Cyclohexanol, 5-methyl-2-(1-methylethyl)-, (1.alpha. 2. beta., 5.alpha.)-(.+/-.)-	1H-3a,7-Methanoazulen-6-ol, octahydro-3,6,8,8-tetramethyl-, acetate, [3R-(3.alpha.,3a.beta.,6.alpha.,7.beta., 8a.alpha.)]-
22	Tetramethylbutanedinitrile	Cyclononasiloxane, octadecamethyl-	Tetramethylbutanedinitrile	Menthol
23	Octadecane	Heptadecane	Octadecane	Tetramethylbutanedinitrile
24	Octadecane	Oxime-, methoxy-phenyl-_	Oxime-, methoxy-phenyl-_	Heptadecane
25	Hexanoic acid	Naphthalene, 1,2,3,5,6,8a-hexahydro-4,7-dimethyl-1-(1-methylethyl)-, (1S-cis)-	Nonadecane	Naphthalene
26	Propanoic acid, 2-methyl-, 3-hydroxy-2,4,4-trimethylpentyl ester	Heneicosane	Hexanoic acid	Nonadecane
27	Propanoic acid, 2-methyl-, 2,2-dimethyl-1-(2-hydroxy-1-methylethyl)propyl ester	Propanoic acid, 2-methyl-, 3-hydroxy-2,4,4-trimethylpentyl ester	Propanoic acid, 2-methyl-, 3-hydroxy-2,4,4-trimethylpentyl ester	Propanoic acid, 2-methyl-, 3-hydroxy-2,4,4-trimethylpentyl ester
28	3-Chloropropionic acid, dodec-9-ynyl	Propanoic acid, 2-methyl-, 2,2-dimethyl-1-(2-hydroxy-1-methylethyl)propyl ester	Propanoic acid, 2-methyl-, 2,2-dimethyl-1-(2-hydroxy-1-methylethyl)propyl ester	Propanoic acid, 2-methyl-, 2,2-dimethyl-1-(2-hydroxy-1-methylethyl)propyl ester
29	Glycerin	Chloroacetic acid, dodec-9-ynyl ester	Chloroacetic acid, dodec-9-ynyl ester	3-Chloropropionic acid, dodec-9-ynyl
30	Triethylene glycol	Triethylene glycol	Triethylene glycol	Triethylene glycol

2.3 POLYMERIC SENSING MATERIALS

The sensing materials used in this thesis research were selected and / or synthesized, based on their reactiveness against ethanol, from the large pool of available polymeric sensing materials protected under the non-disclosure agreement with the industrial collaboration partners. As a result, the contents reviewed under this subsection will only cover the general polymer properties pertaining to the polymeric sensing materials used in this thesis research.

It is well known that the polymeric sorption mechanism has two possible pathways: absorption and adsorption. The former pathway accommodates the analyte compounds temporarily within the polymer, and the latter only allows the compounds to temporarily attach to the polymer on the polymer surface, as illustrated in Figure 2.3.1. Both pathways can lead to certain level of changes to the physical and electrical properties of the polymer, thereby making the polymer sensitive to those analytes that can be absorbed or adsorbed by the polymer.

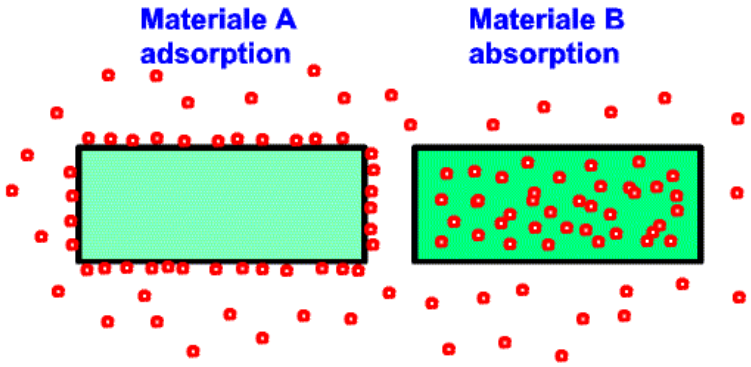

Figure 2.3.1: Comparison of absorption and adsorption [50].

The amount of a specific analyte compound the polymer is capable of accommodating inside the polymer body or on the surface of the polymer would determine the level of reactiveness of the polymer against this analyte. This polymeric nature arises mainly from the number of free polar boding sites along the polymer chain. At the initial polymerization stage, monomers gather up and form smaller polymer chains. Depending on the physical properties of the monomer, either the electrical dipoles or radical groups will form along the polymerized chain to allow temporary polar bonding, as illustrated in Figure 2.3.2 [51]. Towards the end of the polymerization stage, the long polymer chains either align with each other or buckle up on themselves to minimize the net electrostatic force from these dipoles or radical groups [52]. The viscosity of the polymer is directly dependent on the polymer chain size and on the extent of self-buckling and polymer alignment [53].

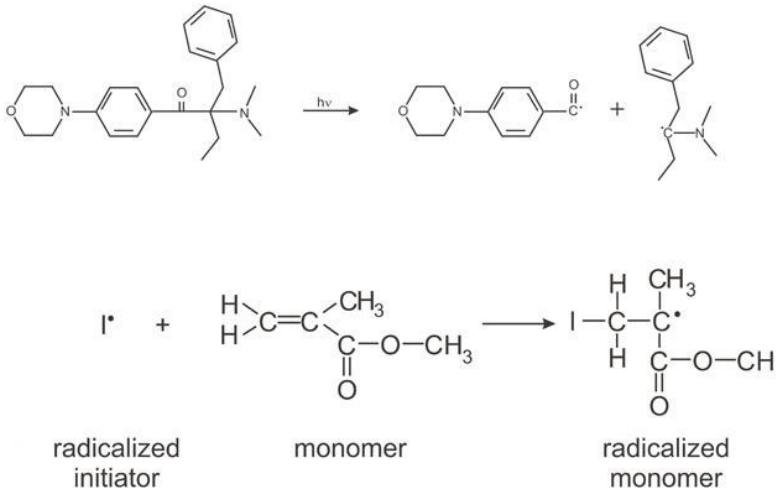

Figure 2.3.2: Example illustration of methyl methacrylate polymerization process with radical group formation [51].

The analyte adsorption occurs when the analyte compound forms a temporary polar bond with one of the unoccupied radical groups or dipoles along the polymer chain on the surface of the polymer. This sorption mechanism introduces a minimal amount of physical change to the polymer because the analytes have a negligible effect on the arrangement of the chains within the polymer, and thus do not affect the physical volume or the level of viscosity of the polymer. However, as far as the electrical properties of the polymer are concerned, the effective dielectric constant (ε_{eff}) of the polymer would potentially experience noticeable changes depending on the properties of the analyte. In general, the analyte adsorption process would temporarily cancel out the free-dangling electrical forces on the surface of the polymer, thus reducing the ε_{eff}. If the analyte itself has additional dipoles or radical groups, however, the free-dangling electrical force could potentially cause a net increase in ε_{eff}. As a final note, an analyte is more likely to be adsorbed by more stable polymers [19].

The process of analyte absorption takes place as the analyte compounds are allowed to work its way into the polymer and occupy the bonding sites in between the polymer chains. This process is much more involving, as the physical and the electrical properties of the polymer would potentially see drastic changes. When the analyte is lightly absorbed, only a small quantity of the analyte temporarily resides within the polymer, mostly near the surface of the polymer. In this case, the spatial occupation of the analyte compounds between the chains has a minimal effect on self-buckling and the inter-polymer alignment arrangement, and thus would not affect the physical

properties of the polymer. The electrical properties of the polymer are affected in the same way as those in the adsorption process. However, as the level of analyte absorption increases, the spatial occupation of the analyte becomes increasingly significant because the polymer chains are pushed further apart, forcing the polymer chains to unbuckle and change their alignments with respect to each other. At this stage, the physical volume of the polymer increases, and the coupled changes in physical and electrical properties of the polymer lead to higher responsiveness of the polymer against the absorbed analyte. This effect is known as polymer swelling, and is only achievable when the analyte compound has a sufficient level of chemical affinity with the polymer [19].

When the polymer is exposed to analytes with very high levels of affinity, the physical occupation of the analyte compounds in between the chain introduces enough physical stress to straighten the polymer chain, leading to significant drop in polymer viscosity. In this case, the phenomenon of polymer reflow takes place, and the sensor carrying the polymer may potentially lose its sensitivity due to the outflow of the polymeric sensing material from the sensor site. Analytes that are known to be effective solvents of the polymer would more likely cause polymer reflow.

Finally, certain polymers (i.e., Polyaniline [21]) are optimal for going through the co-polymerization process [22] or doping process [23] to enhance or inhibit analyte sorption. Polymeric sensors targeting specific group of analytes may take advantage of the polymer customization process to improve the sensitivity and the selectivity of the sensor.

CHAPTER 3

PLANAR RF RESONANT POLYMER-BASED GAS SENSOR

3.1 INTRODUCTION

Chapter 3 introduces a novel undercoupled RF resonant sensor platform that enables gaseous phase chemical detection for passive sensor-embedded RF devices and RFIDs. The resonant sensor is implemented with an interdigital chemi-capacitor and a transmission-line inductor, thus only requiring a simple two-layer fabrication process. Its superior sensitivity at RF frequencies arises from the benefits of response amplification near resonance, as well as the shorter wavelength at radio-frequencies. Furthermore, the interdigital capacitor allows polymeric sensing materials to be directly deposited on top, thereby improving fabrication repeatability. The sensor prototypes are loaded with six different polymeric sensing materials (OV225, OV275, SC201(SXFA), P25DMA, P25DMA with 20% NiO dopant, and P25DMA with 20% ZnO dopant) that aim to detect certain pre-preparatory transdermal biomarkers including gaseous phase ethanol, methanol, benzene, and acetone. Their respective responses are recorded in terms of three distinctive RF parameters (resonant frequency shift [Δf_0], response amplitude change [ΔS_{11}], and response delay change [ΔGD_{11}]), from which the sensitivities of these sensors are determined and their selectivities with

respect to the sample gas analytes are subsequently characterized. Finally, evaluation of the response signatures of the polymeric sensing materials to each gas analyte enables the future development of sensor array systems that can distinguish desired analytes from unwanted interferents.

3.2 RESONANT SENSOR DESIGN AND THEORY

Resonant sensors yield a much higher sensitivity than static sensors, as the sensor response near resonance is drastically affected by the shift in resonant frequency (f_0) of the sensor [29]. Fig. 3.2.1 illustrates the circuit model and the coplanar waveguide (CPW) realization of an inductor-capacitor (LC) resonant sensor implemented with interdigital chemi-capacitor as the sensing element. The input coupling section, indicated as port 1 in the figure, is where the high frequency signals are delivered into the resonant sensor, and where the reflected high frequency signals are captured for sensor readout.

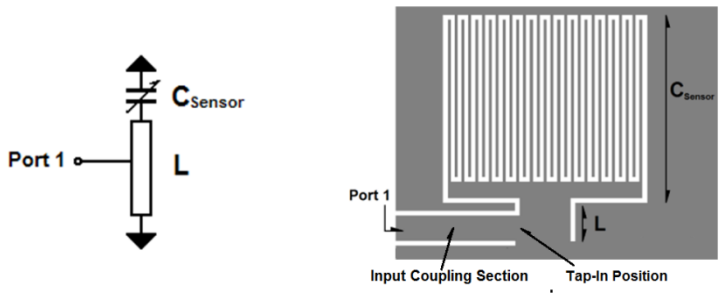

Fig. 3.2.1: Combline LC-based RF resonant sensor model (Left) and its CPW implementation (Right).

The resonant sensor captures changes in environmental parameters of interest through capacitance variations arising from changes in the dielectric constants (ε_r) and volume of the functional polymer. Even though parallel-plate chemi-capacitors are commonly known to yield better performance as sensing elements, the performance of interdigital chemi-capacitors is highly dependent on the operation frequency. As illustrated on the left side of Fig. 3.2.2, at DC and low-frequency AC, a sizeable portion of the fringing electric field passes through the substrate. This portion of the field does not see any changes in electrical and physical properties of the functional polymer and thus is merely a 'dead weight' that degrades the sensing performance. This drawback, however, becomes increasingly negligible for higher operation frequencies.

As illustrated on the right side of Fig. 3.2.2, the electric field is highly concentrated at the conductor surface at RF, as the wavelength of the propagating electromagnetic (EM) wave approaches the dimension of the thin-film interdigital chemi-capacitor [30], thus allowing significantly more field lines to pass through the polymeric sensing material. Based on the Ansoft High-Frequency Structure Simulator (HFSS) simulation results at the selected operation frequency of 6.7 GHz, 95% or more of the electric field is confined within 5μm both above and below the conductor surface between the capacitor fingers of the interdigital capacitor. Accompanied by the relative ease of polymer deposition and simple fabrication, the interdigital chemi-capacitor is a more preferred design choice for RF resonant sensor applications.

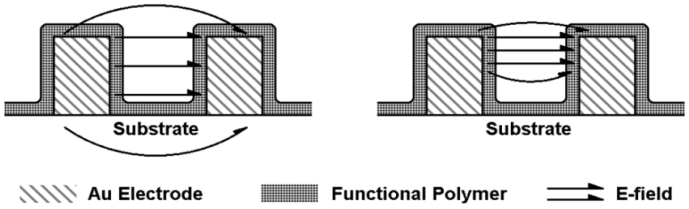

Fig.3.2.2: Electric field distribution around the polymer-coated interdigital chemi-capacitor electrodes at low frequencies (left) and RF frequencies (right).

The changes in sensor capacitance (ΔC_{Sensor}) are relatively small. In view of the resonant frequency, $f_0 = 1 / (2\pi(L \cdot C_{Sensor})^{0.5})$, a small ΔC_{Sensor} would translate into an even smaller Δf_0. However, as illustrated in Fig. 3.2.3, for a resonant sensor being sampled at an arbitrary frequency near f_0, the response amplitude (S_{11}) and the response delay ($GroupDelay_{11}$, or GD_{11}) both see drastic changes under a relatively small Δf_0, or small ΔC_{Sensor}. This phenomenon of response amplification effectively validates the use of resonant sensor at RF for its capability of capturing small ambient parameter variations, of which the conventional chemi-capacitive sensing elements that operate at low frequencies are incapable. Eq. 3.1 and Eq. 3.2 respectively outlines the S_{11} and f_0 sensitivity model for a parallel RLC-resonant sensor implementing a chemi-capacitive element with a characteristic impedance of Z_0.

$$\frac{\delta f_0}{\delta C_{Sensor}} = -(4\pi\sqrt{LC_{Sensor}{}^3})^{-1} \tag{3.1}$$

$$\frac{\delta S_{11}}{\delta C_{Sensor}} = \frac{-j4\pi f Z_0}{Z_{in}{}^2(Z_{in}+Z_0)^2} \quad where \quad Z_{in} = (\frac{1}{R} + j2\pi f C_{Sensor} - \frac{j}{2\pi f L}) \tag{3.2}$$

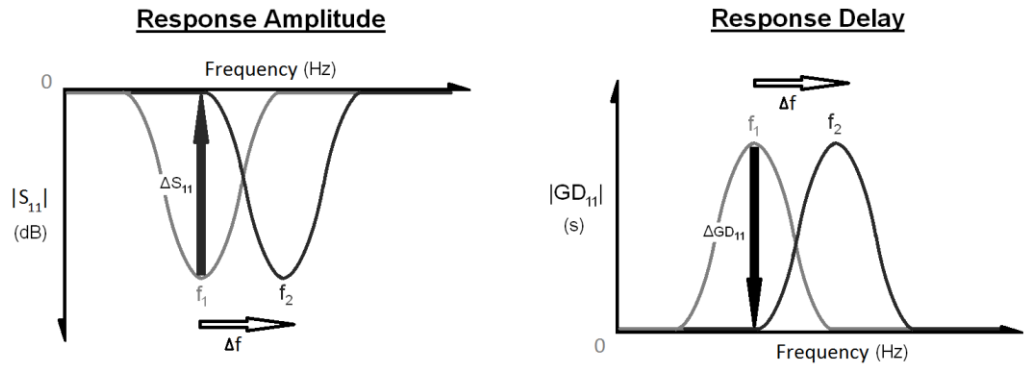

Fig. 3.2.3: Large ΔS11 and ΔGD11 result from a small Δf_0 upon chemical exposure to the resonant sensor.

However, the magnitude of ΔS_{11} and ΔGD_{11} are not solely dependent on the amount of Δf_0. The sharpness of the response peak at resonance is also dependent on it and is a direct attribute of the loaded quality factor (Q) of the resonator that results from the physical design properties of the input coupling section, such as the resonator size or the structural materials. All resonating structures have their maximally achievable Q defined as the unloaded Q factor; the higher the loading from the input coupling section, the lower the loaded Q drops from the unloaded Q. As a result, designing the input coupling section with the minimum feasible loading to the resonator results in an optimized loaded Q. This would consequently sharpen the resonant peaks for both S_{11} and GD_{11}, thereby increasing the sensitivity of the sensor. Upon Δf_0, a reasonably undercoupled resonator always sees a more drastic response change than an overloaded resonator does [29]. As an example, the desired undercoupled resonant sensor illustrated in Fig. 3.2.1 can be achieved with a carefully chosen tap-in position between the input coupling section from port 1 and the inductor (L) section of the resonant sensor. HFSS simulations of this RF resonant sensor, with an assumed unloaded Q of ~80, indicate that a 5% $\Delta\varepsilon_r$ of the polymeric sensing material would only result in ~2% Δf_0, but would give a highly noticeable 25% change in S_{11} and GD_{11}. The percentage normalization is done with Eq. 3.3 as shown below.

$$\%\Delta f_0 = \frac{f_{0(x\ ppm)} - f_{0(0\ ppm)}}{f_{0\ (0\ ppm)}} \times 100\%$$

$$\%\Delta S_{11} = \frac{S_{11(x\ ppm)} - S_{11(0\ ppm)}}{S_{11(0\ ppm)}} \times 100\% \qquad \%\Delta GD_{11} = \frac{GD_{11(x\ ppm)} - GD_{11(0\ ppm)}}{GD_{11(0\ ppm)}} \times 100\%$$

(3.3)

3.3 FABRICATION OF RESONANT SENSOR

Fig. 3.3.1 illustrates the fabrication process of the RF resonant sensor carried out on a 3" glass wafer. A 30μm Cr - 70μm Au electroplating seed layer was deposited through e-beam evaporation, followed by a 9-μm electroplating mold constructed with a positive thick-film resist of AZ9260 that defines the pattern of the resonant sensor as well as the CPW transmission line. It is important to note that AZ9260 requires at least one full hour of rehydration process after soft bake at 90°C, as do many other thick-film photoresists. A sufficiently rehydrated AZ9260 resist coating would guarantee a minimum feature size of approximately 10 μm and a consistent development time of approximately 13 minutes at 30 °C with a magnetic stir bar agitation at 500 rpm. Lack of sufficient rehydration would detrimentally reduce the photosensitivity of the resist closer to the substrate surface due to the uneven distribution of moisture within the film, and would lead to failure in resist development. Post-exposure baking and post-development baking are not recommended for AZ9260, as it may lead to resist cracking.

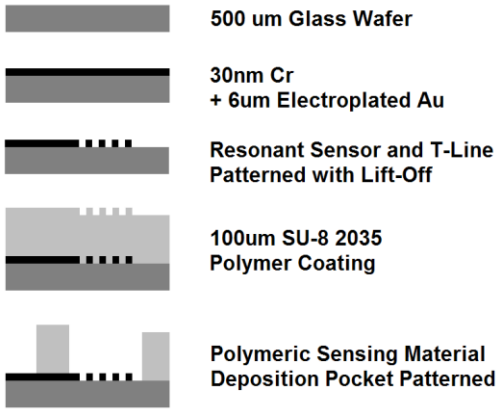

Fig. 3.3.1: Sample fabrication process of the thick-film RF resonant sensor with polymer deposition pocket.

The 6-μm gold layer was plated at a rate of ~50nm/min to ensure minimal current crowding on the mold edge. This rate was optimized based on the caustic solvent resistance of the AZ9260 mold, as AZ9260 can also suffer surface cracks under prolonged immersion in the basic gold-plating solution, leading to gold metal growth on unwanted areas of the wafer.

The Cr-mask liftoff process and the subsequent seed layer removal were then used to minimize the fabrication error in the interdigital electrode gaps. AZ9260, unlike most AZ negative photoresist-based electroplating molds, dissolves instead of peel off from the substrate in Kwik-Strip remover

during the lift-off process. This difference arises from the fact that most negative photoresists intended for electroplating are designed to form a thin dissolvable layer between the substrate surface and the cured resist in order to guarantee a physical resist lift-off in the stripper solution. However, the curing mechanism of the positive photoresists cannot accommodate the formation of such a layer. Due to this limitation, the thickness of the plated metal, including that of the current-crowding edges, is recommended to be at least 1 μm less than the mold thickness to ensure the success of the Cr-mask lift-off process.

Finally, the polymer deposition pocket made of 100um-thick SU-8 2035 was patterned to ensure consistent polymer deposition on the chemi-capacitor and to protect the rest of the RF components from polymer overflow. The fabricated sensors are shown in Fig. 3.3.2.

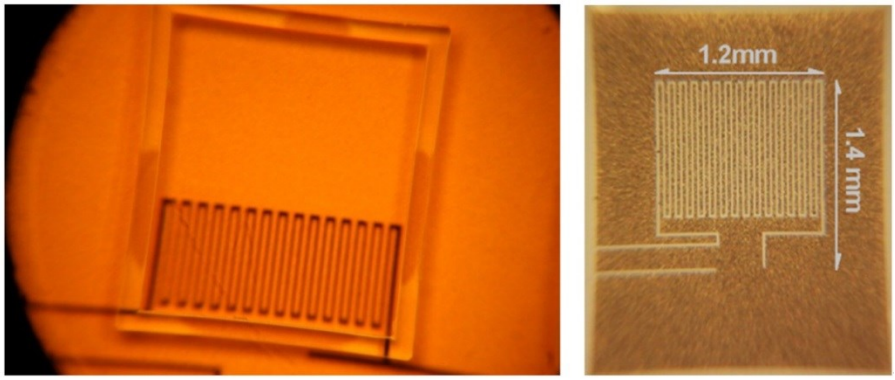

Fig. 3.3.2: Fabricated RF resonant sensor with SU-8 polymer pocket.

3.4 POLYMERIC SENSING MATERIALS PREPARATION AND DEPOSITION

Two different families of polymeric sensing materials were prepared for functionalizing the RF resonant sensor. The first family consists of the siloxane-based functional polymers, in which OV225 and OV275 are readily available from Ohio Valley Chemical Specialities and SC201 (SXFA) is available from SeaCoast Science. The siloxane polymers are known to be highly sorbent towards alcohol and ketone groups, and can be easily dissolved in common ketone-based solvents such as acetone and dioxane, or alcohol-based solvents such as isopropanol and methanol. When exposed to target analytes, the siloxane-based polymers increase in volume due to analyte absorption, and the dielectric constants of the polymers change due to the occupation of the polar bonding sites by analyte molecules along the siloxane polymer chain. The coupled effect of electrical and physical

property variations helps make the siloxane-based polymers a good polymeric sensing material for the RF interdigital chemi-capacitive resonant sensor. Table 3.4.1 enumerates the physical properties of the three siloxane-based polymers to be deposited onto the sensor.

Table 3.4.1: Electrical and Physical Properties of OV225, OV275, and SXFA

	Nominal Relative Permittivity	Viscosity (cP)	Nominal Stable Thermal Range (˚C)
OV225	11.5	~100,000	-100 ~ 250
OV275	33.0	> 1 Million	-100 ~ 250
SXFA	16.0	~80,000	-100 ~ 150

Table 3.4.2 enumerates the solvent dilution recipes that have been tested for polymer deposition on the sensor. The deposition tools used for polymer dispensaries are a hand-held micropipette, as shown in Fig. 3.4.1; a mechanical positioner-controlled micropipette, as shown in Fig. 3.4.2; and a Sonoplot Microplotter station, as shown in Fig. 3.4.3.

Table 3.4.2: Polymer Dilution Recipes and the Respective Deposition Parameters

Polymeric Sensing Material	Dilution Solvent (HPLC-Grade)	Dilution Ratio (w.t. %)	Dilution Result	Deposition Temp. (°C)	Deposition Tools*	Curing
OV-225	Acetone	>0.01	Dissolved	-10	A, B	80°C, 30m
	Dioxane		Dissolved	25	A, B, C	110°C, 4h
	Ethanol		Emulsified	25	N/A	N/A
	Methanol		Dissolved	-10	A, B	80°C, 30m
OV-275	Acetone	>0.01	Dissolved	-10	A, B	80°C, 30m
	Dioxane		Partly Dissolved	25	A, B, C	110°C, 4h
	Ethanol		Emulsified	25	N/A	N/A
	Methanol		Emulsified	25	N/A	N/A
SXFA	Acetone	>0.01	Dissolved	-10	A, B	80°C, 30m
	Dioxane		Dissolved	25	A, B, C	110°C, 4h
	Ethanol		Emulsified	25	N/A	N/A
	Methanol		Dissolved	-10	A, B	80°C, 30m

* A) Hand-Held Micropipette, B) Mechanical Positioner-Controller Micropipette, C) Sonoplot Microplotter.

Fig. 3.4.1: VWR 1uL hand-held micropipette.

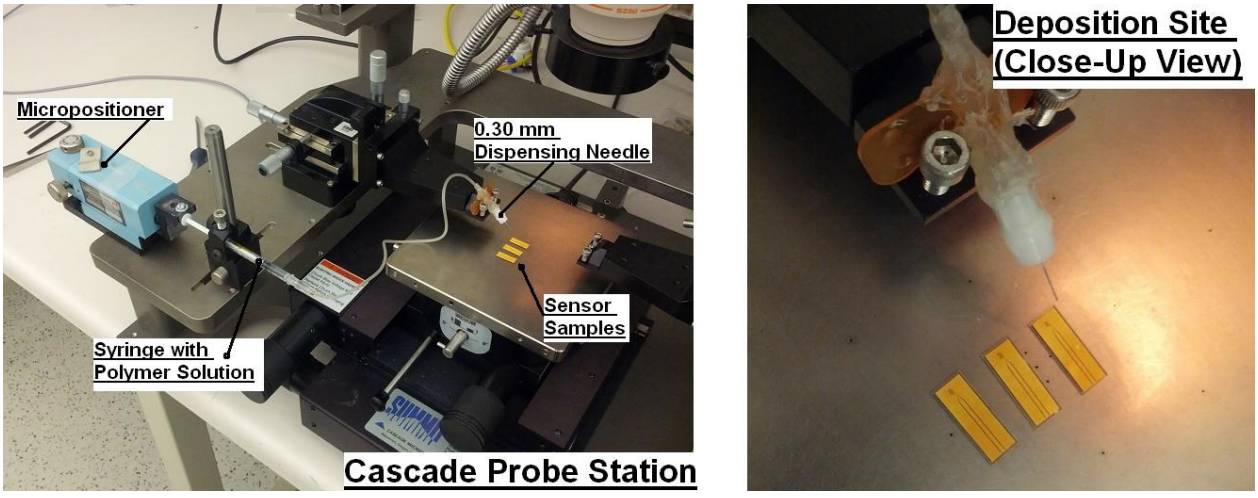

Fig.3.4.2: Cascade probe station with mechanical positioner-controlled micropipette.

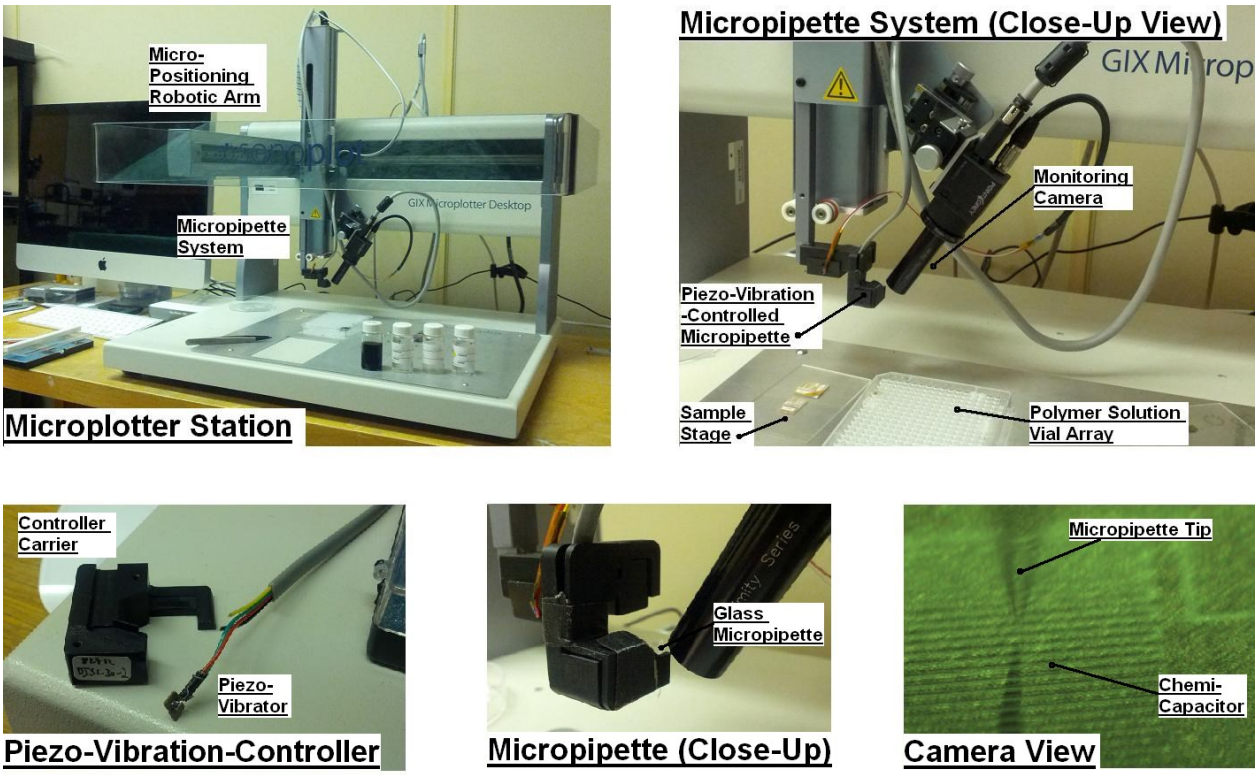

Fig. 3.4.3: Sonoplot™ microplotter station.

Through the trials presented in Table 3.4.2, the solvent of acetone was found to be the most suitable for dissolving the siloxane-based polymeric sensing materials. Acetone has been found to be able to dissolve polymers with high molecular weight and viscosity (e.g., OV-275), while other solvents were not able to fully dissolve OV-275. The low evaporation temperature of acetone (~43°C) ensures fast curing, and baking can be carried out well below the breakdown temperature of all the polymers. The only two drawbacks in using acetone as a solvent are: a) its limited deposition time, as acetone evaporates at a steady rate even within the pipette; and b) its incompatibility with the Sonoplot microplotter due to mechanical limitations of the plotter system. Ether was another alternative solvent under initial consideration, but due to its very high volatility and boiling temperature of less than 40°C, ether was found to evaporate at a rate too fast to allow reliable polymer deposition.

Dioxane was another alternative of acetone that had the advantage of higher boiling temperature (~98°C). It was initially found to be a great solvent that enables the use of Sonoplot microplotter for more precise and controllable polymer deposition. However, the polymeric sensing materials, after

being cured at ~110°C for 4 hours, demonstrated a significant reduction in sensing capability. Since the curing temperature of 110°C was well below the documented breakdown temperature of siloxane polymers, this compromised performance was concluded to be the result of incomplete curing. Further curing tests at higher temperatures were carried out, and the curing was never found to be completed below the temperature of 150°C, which is the breakdown temperature of SXFA. As a result, dioxane was deemed unsuitable for our application.

Finally, ethanol and methanol were only capable of dissolving siloxane polymers with lower molecular weights (OV-225 and SXFA) and would merely emulsify OV-275. Consequently, the alcohol solvents were not chosen for our application.

The second family of polymeric sensing material consists of a polyaniline-based polymer known as P25DMA, and two of its derivatives with metal-oxide dopants: nickel-oxide (NiO) and zinc-oxide (ZnO). This series of the polymer is currently included as a proprietary asset of our industrial collaborator; as a result, the detail information on the synthesis and material characterization of P25DMA will not be disclosed in the thesis. As illustrated in Fig. 3.4.4, the dopants were added to functionalize the polyaniline polymer chain, allowing the polymer to gain improved sensitivity against specific analytes. These polymers were synthesized by chemical specialists at the Advanced Polymer Institute at the University of Waterloo, and the chemical properties as well as the respective dilution recipes of the polymers are provided in Table 3.4.3, with N-Methyl-2-Pyrrolidone (NMP) as the primary solvent.

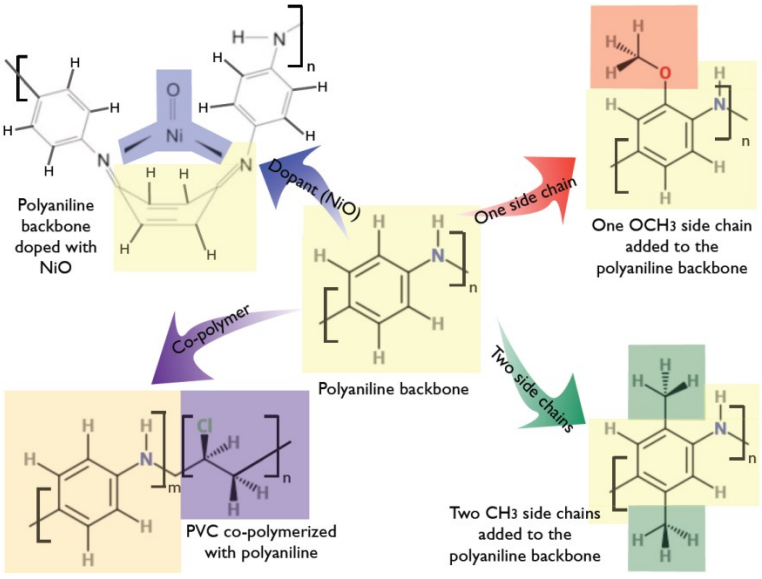

Fig. 3.4.4: General principle of polyaniline functionalization [54].

Table 3.4.3: P25DMA Family Material Properties

Polyaniline Family	Functionalization	Physical Form	Nominal Stable Thermal Range (˚C)	Solvent
P25DMA	N/A	Black Powder	-20 ~ 100	NMP, Agitation 1 ~ 3 w.t.%
P25DMA, 20% NiO-Doped	Enhanced Ethanol Detection	Dark Purple Powder	-20 ~ 100	NMP, Agitation 1 ~ 3 w.t.%
P25DMA, 20% ZnO-Doped	Inhibited Ethanol Detection	Dark Green Powder	-20 ~ 100	NMP, Agitation 1 ~ 3 w.t.%

The deposition of the NMP-diluted P25DMA polymers can be done on all three dispensary systems. The curing process must be carried out in the furnace at 85°C for at least 12 hours to ensure full evaporation of NMP (boiling point at 232°C), and to protect the polymers from suffering thermal damage. The deposited polymers can be easily identified by their colour, as shown in Fig. 3.4.5.

Fig. 3.4.5: Colour difference of the P25DMA family solutions
(left – P25DMA, centre – P25DMA 20% NiO, right – P25DMA 20% ZnO).

The deposition processes for the siloxane families of polymeric sensing materials have encountered the challenge of non-uniform polymer coatings on the fingers of the interdigital chemi-capacitor. Such deposition artifacts can adversely impact the sensitivity of the sensors as well as the repeatability of the sensor fabrication and functionalization process. As an example, Fig. 3.4.6 illustrates the non-uniform polymer coating of OV-275 on the sensor fingers with two deposition coatings.

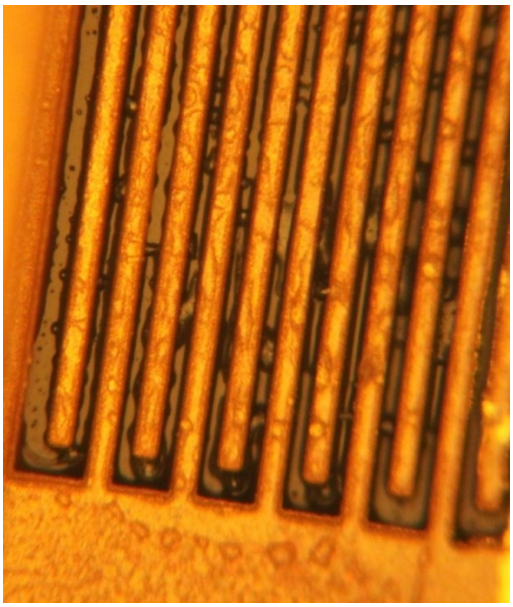

Fig. 3.4.6: Prominent non-uniform coating of OV-275 on interdigital capacitor fingers.

Fig. 3.4.7 and Fig. 3.4.8 show the non-uniform coating of OV-225 and SXFA on the capacitive fingers. It is evident that the agglomeration of the polymer around the capacitive finger after curing is highly dependent on the molecular weight of the siloxane polymer family, with OV-275, the polymer with the highest molecular weight and viscosity, yielding the worst non-uniform coating. A simple method to improve the problem is to dilute the polymer solution well below 0.01 w.t.% and apply multiple coatings to reduce the amount of polymer agglomeration.

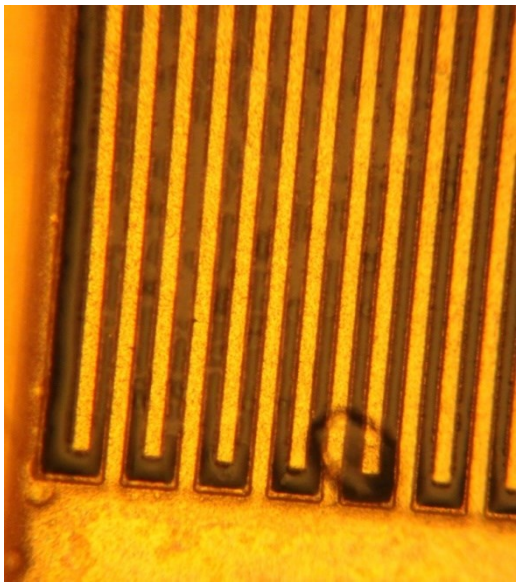

Fig. 3.4.7: Visible non-uniform coating of OV-225 on interdigital capacitor fingers.

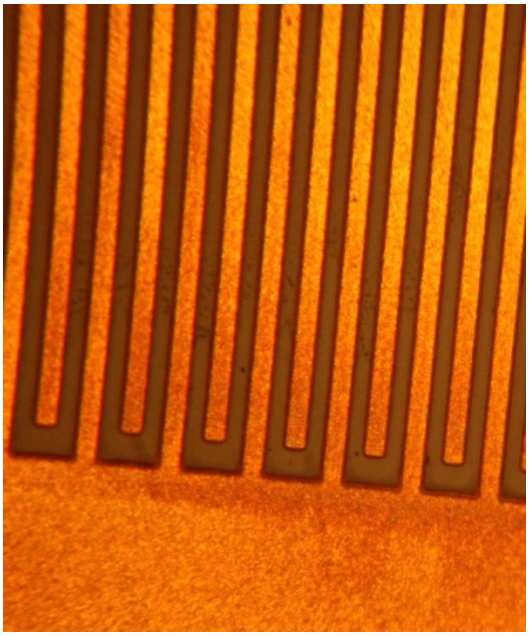

Fig. 3.4.8: Light but visible non-uniform coating of SXFA on interdigital capacitor fingers.

On the contrary, the polyaniline family has not experienced the polymer agglomeration problem, as illustrated in Fig. 3.4.9. Nevertheless, NMP is incapable of fully dissolving large pieces of polyaniline crystals, resulting in occasional large pieces of crystalline being deposited on the sensor area, as demonstrated by the one on the lower left corner of Fig. 3.4.9. The solution to this problem is under development at the Advanced Polymer Institute.

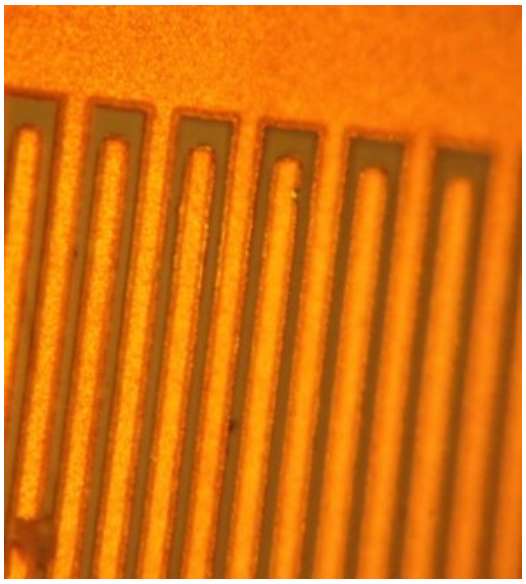

Fig. 3.4.9: Uniform P25DMA polymer coating with crystal piece artifact (lower left corner).

Finally, the capacitor sections of the sensor are put under constant inspections during the polymer coating process as well as after the curing process to ensure satisfactory results are achieved. The RF performance of the sensor as a whole had also been monitored with a dedicated vector network analyzer to ensure no physical damages were introduced during the deposition process.

3.5 CHEMICAL CHARACTERIZATION SYSTEM

The sensors were individually connected to an Agilent 8719ES Vector Network Analyzer (VNA) and then placed into the multipurpose gas analyte chemical testing system [48], as shown in Fig. 3.5.1.

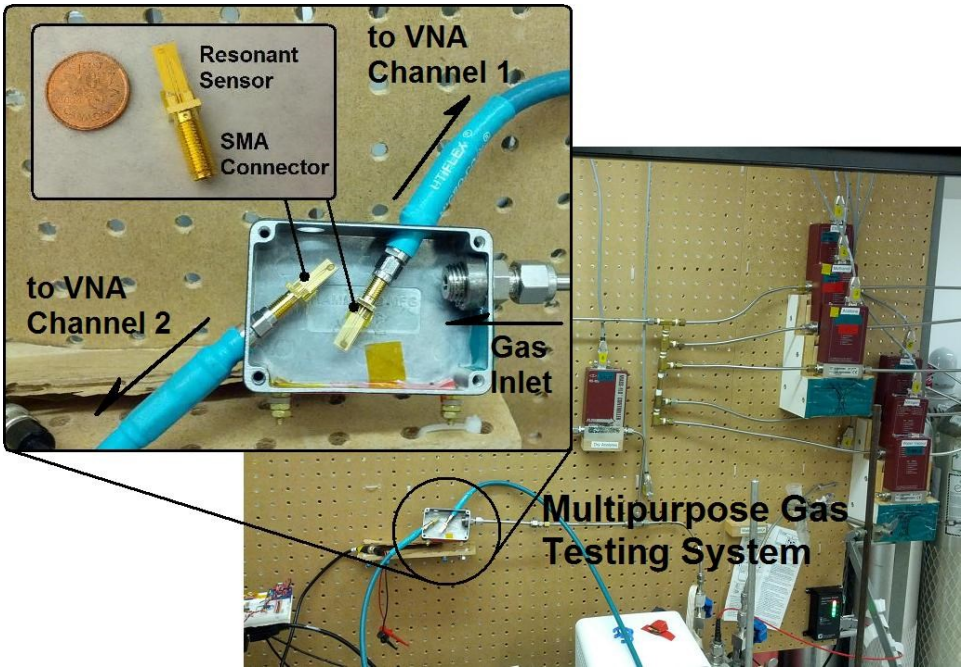

Fig. 3.5.1: Experimental set-up with the chemical gas testing system.

The testing chamber shown in Fig. 3.5.2 receives a constant inflow of gas mixture at a flow rate of 200 sccm from the MFC (mass flow controller) network, regardless of the presence or absence of analyte under testing. In the absence of analyte gases, the gas inflow is controlled at 200 sccm of pure nitrogen gas, which produces a baseline reading. When analyte gases are delivered to the testing chamber, the gas inflow is maintained at 200 sccm, with the analyte gases mixed in controlled proportions with nitrogen gas to produce the desired analyte concentration. This set-up effectively eliminates any mechanical interference with sensor response during analyte gas swapping, and guarantees that all the response curves recorded on the VNA are purely due to chemical interactions between the polymer and the analytes. The chamber is kept at atmospheric pressure (1 atm) with no pressure sealing between the lid and the chamber body, and three sidewall openings with diameters larger than the gas inlet ensure no back-pressure build-up inside the chamber. Under an environment-controlled fume-hood for consistent sensor characterization conditions, the system operates at a room temperature of 22˚C (with no active heating or cooling) and a constant humidity of 80%. The sensor shown in Fig. 3.5.2 is the first generation sensor design, where the sensor is fabricated with CPW feed lines to be wire-bonded to the CPW-to-SSMA housing. Fig. 3.5.3 shows the second generation sensors, where the sensors have the properly-designed CPW feed lines that can allow direct SMA connector installation through silver epoxy bonding. The results shown in the thesis are all collected from the second-generation sensors.

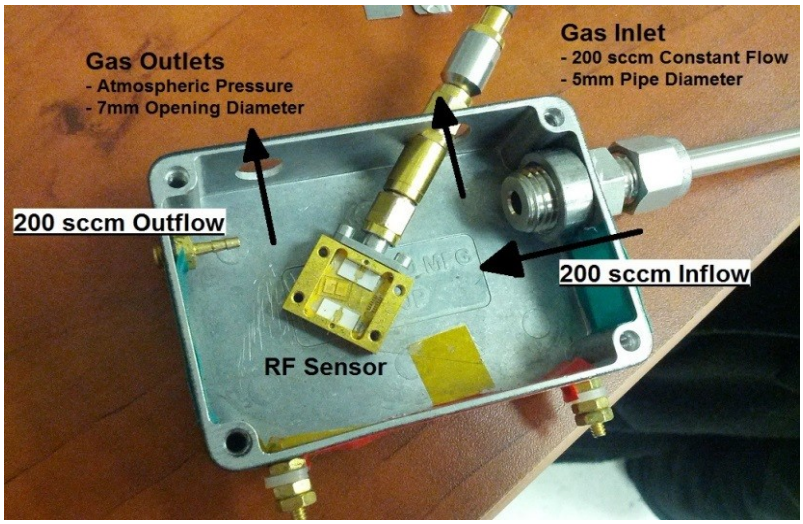

Fig. 3.5.2: Chamber gas flow diagram illustrating atmospheric chamber pressure and zero pressure buildup.

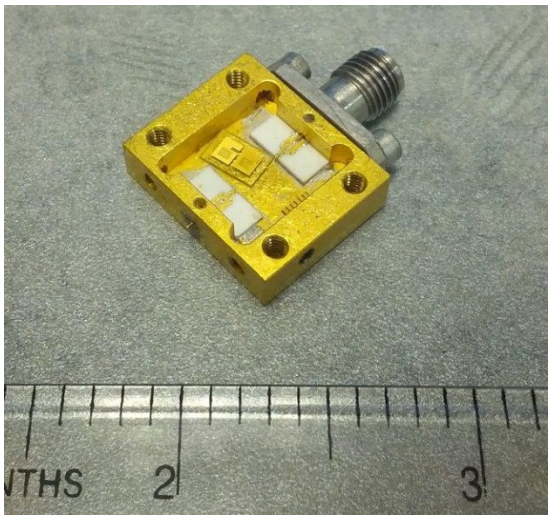

Fig. 3.5.3: First-generation (SSMA housing with CPW wire-bond) sensors under testing.

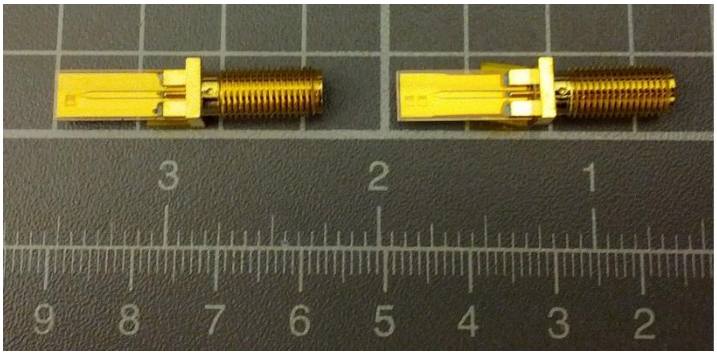

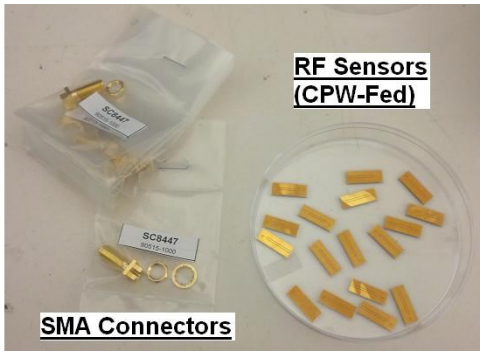

Fig. 3.5.4: Second-generation (direct epoxy-bonded SMA connector) sensors under testing.

The sensors were then exposed to gaseous ethanol, methanol, and benzene at 5 discreet concentrations (5000 ppm, 2500 ppm, 1250 ppm, 625 ppm, and 0 ppm), all of which were proportionally pre-mixed with nitrogen by the MFC network from the 5000 ppm analyte gas cylinder provided by Praxair, before being fed at 200 sccm into the testing chamber. The sensors were purged with pure nitrogen flow for 10 minutes before and after gas analyte exposure, and the steady state responses of the sensors were captured 5 minutes after the gas analytes were delivered into the chamber. At each sampling point, the centre frequency (f_0), the response amplitude (S_{11}), and the response delay (GD_{11}) were recorded.

The transient response of the sensor was captured in an 8-minute step stimulation span. The gas analyte was delivered to the chamber at t = 0 with a concentration of 5000 ppm and a constant flow rate of 200 sccm, and S_{11}, and GD_{11} were recorded every 15 seconds, which was the shortest interval achievable by the VNA. At t = 4 minutes, the gas analyte was turned off, and the nitrogen purge began. The entire 8-minute span provided a panoramic perspective of the response and recovery characteristics of the RF resonant sensor.

All data points were collected with at least four independent replicates for determining the tolerance range as well as response linearity.

3.6 SAMPLE MEASUREMENTS AND ANALYSIS

This section outlines the method of collecting and analyzing the RF response of a single sensor, and the subsequent extractions of the performance parameters of the sensor. All the results summarized in sections 3.7 and 3.8 were obtained through the same measurement and analysis methods.

3.6.1 Single-Trial Measurements and Sensor Response Analysis

With the experimental set-up introduced in the previous section, the reflection coefficient (S_{11}) curve and the group delay curve (GD_{11}) of the sensor are recorded with the VNA. The cursors on the VNA display are set up to monitor the S_{11} and GD_{11} near the resonant frequency of the sensor, where the change in response magnitude is expected to be the largest.

Fig. 3.6.1 to Fig. 3.6.5 are a sequence of five VNA screen captures of the S_{11} response of an OV-275 RF resonant sensor exposed to five discrete concentrations of gaseous ethanol, as outlined the in the previous section. Cursor #1 is set up to monitor the approximated centre frequency of the sensor; cursors #2 and #5 are set up to monitor the -3dB frequency of the sensor response at the initial exposure of 5000 ppm, and cursors #3 and #4 monitor the -9.56dB frequency and -5dB frequency of the initial exposure, respectively. All S_{11} magnitudes were arbitrarily selected to monitor the S_{11} curve movements upon analyte exposures.

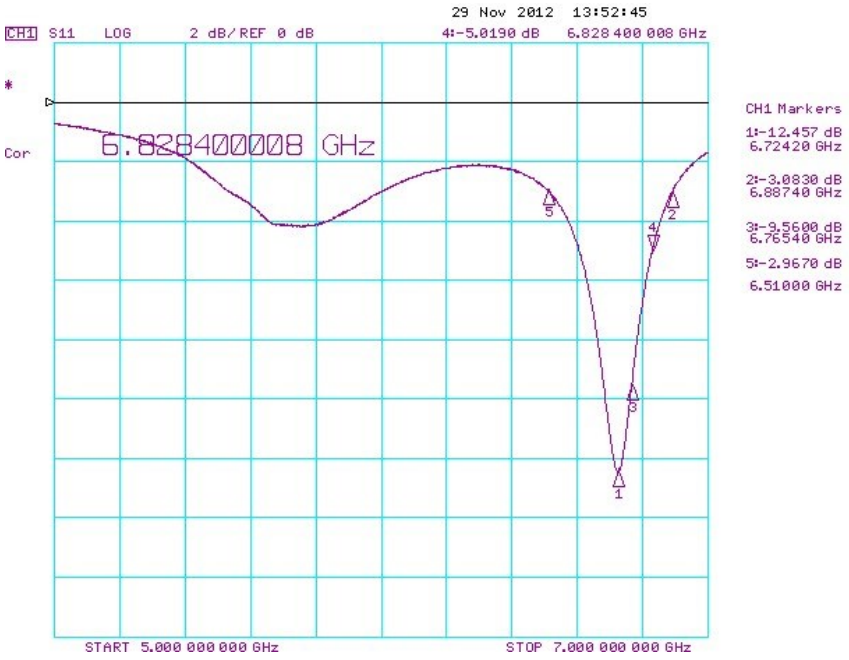

Fig. 3.6.1: S_{11} response of OV-275 sensor with 5000 ppm ethanol exposure.

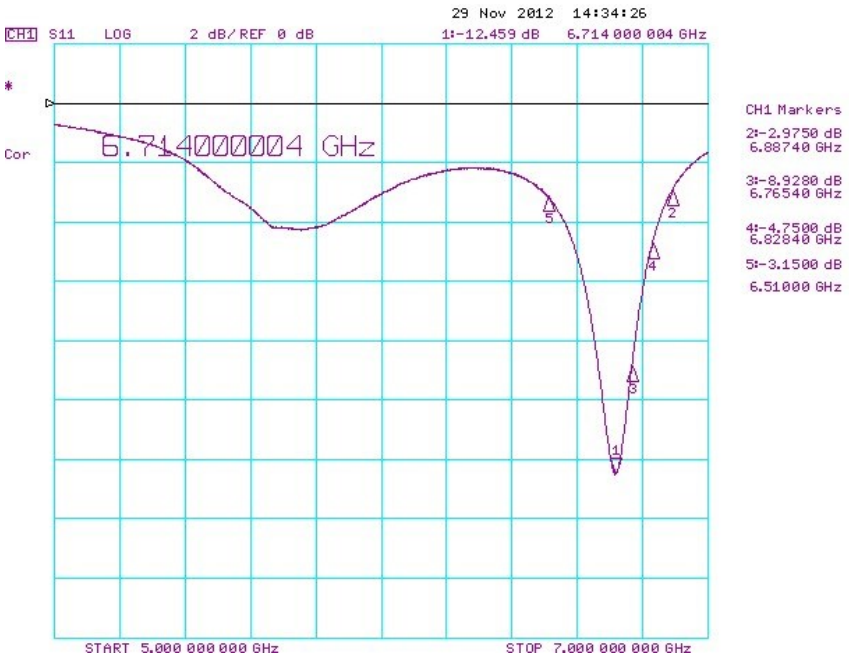

Fig. 3.6.2: S_{11} response of OV-275 sensor with 2500 ppm ethanol exposure.

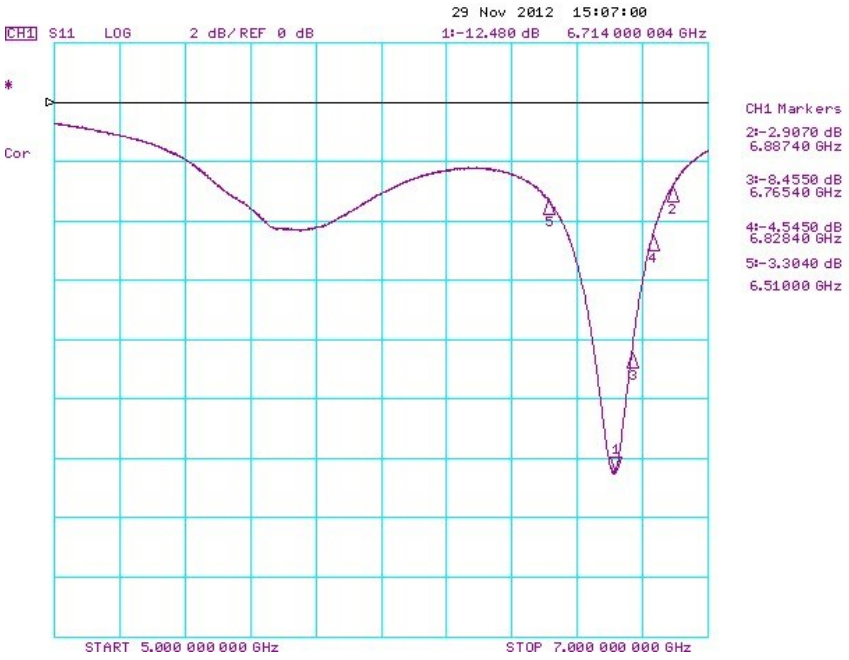

Fig. 3.6.3: S_{11} response of OV-275 sensor with 1000 ppm ethanol exposure.

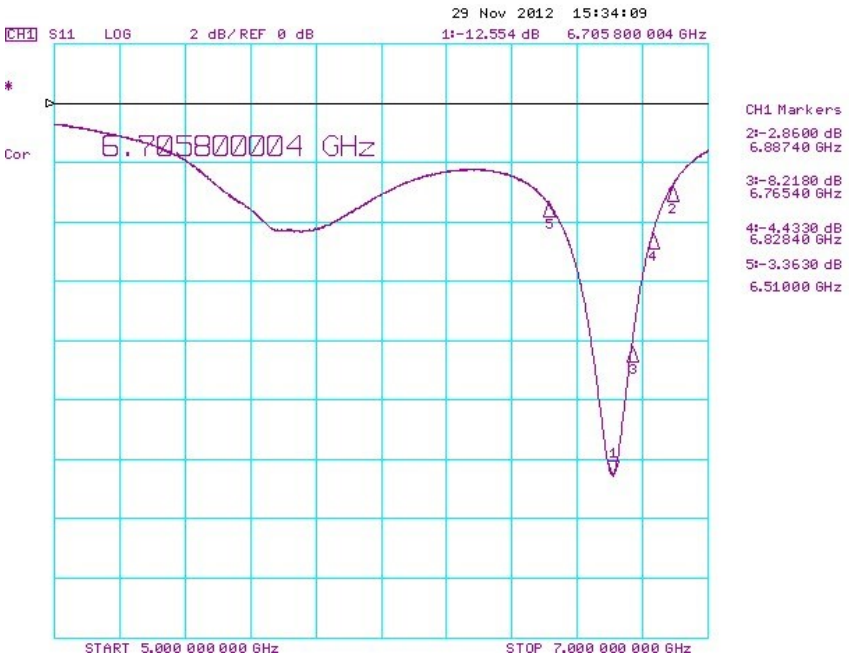

Fig. 3.6.4: S_{11} response of OV-275 sensor with 500 ppm ethanol exposure.

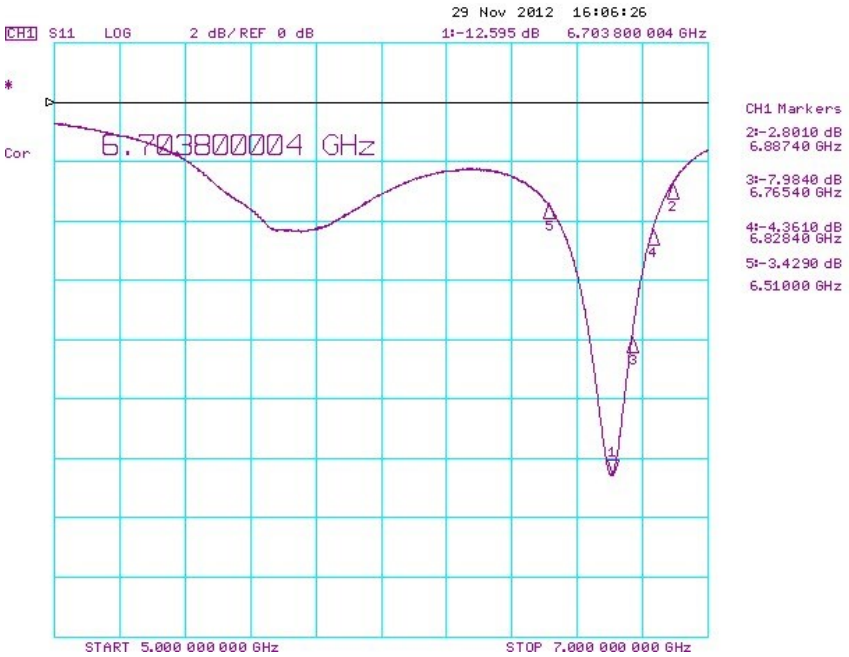

Fig. 3.6.5: S_{11} response of OV-275 sensor with zero ethanol exposure.

As the first approximation on the VNA screen captures, cursor 1 recorded a total frequency shift of ~21 MHz at the centre frequency of 6.7 GHz ($\Delta f_0 \sim 0.31\%$), but the total change in S_{11} magnitude monitored by cursor 3 was recorded to be ~1.58 dB ($\Delta S_{11} \sim 19.8\%$). This result clearly verifies the improvement in sensitivity from operating the sensor in resonant mode.

Fig. 3.6.6 and Fig. 3.6.7 are the Excel graphical summary of the exported S_{11} and GD_{11} curves from VNA. With clearer zoom-in views on the curves, the recorded total resonant frequency shift is 21.25 MHz ($\Delta f_0 \sim 0.32\%$), and the total change in S_{11} amplitude at the original cursor 3 position (6.7654 GHz) is 1.674 dB ($\Delta S_{11} \sim 20.90\%$). Similarly, the total change in GD_{11} recorded at the cursor 3 position is 1.24 ns ($\Delta GD_{11} \sim 49.4\%$). All the normalized percentage changes are calculated with Eq. 3.3.

All of the trials recorded in the steady state and transient response analysis follow the same methodology to extract the sensor responses in terms of the centre frequency shift (Δf_0), the change in reflection coefficient amplitude (S_{11}), and the change in response group delay (GD_{11}).

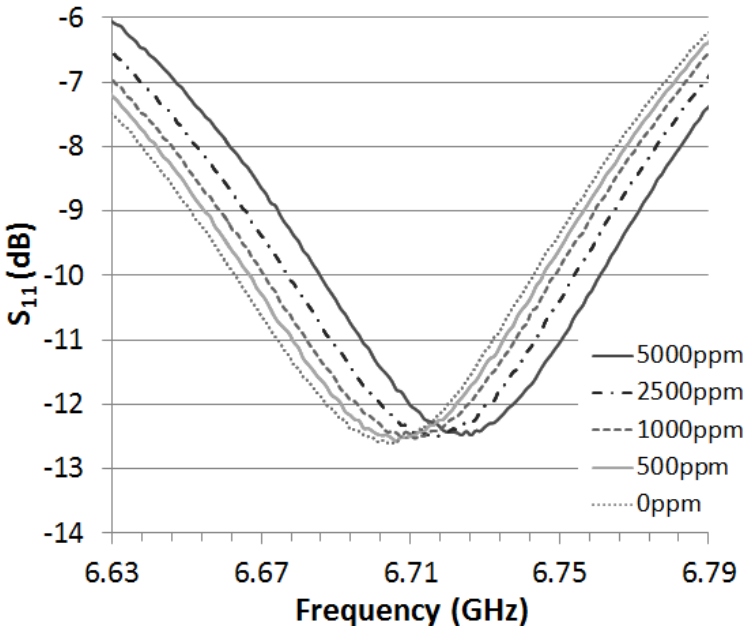

Fig. 3.6.6: Summary of S_{11} response curves of OV-275 sensor.

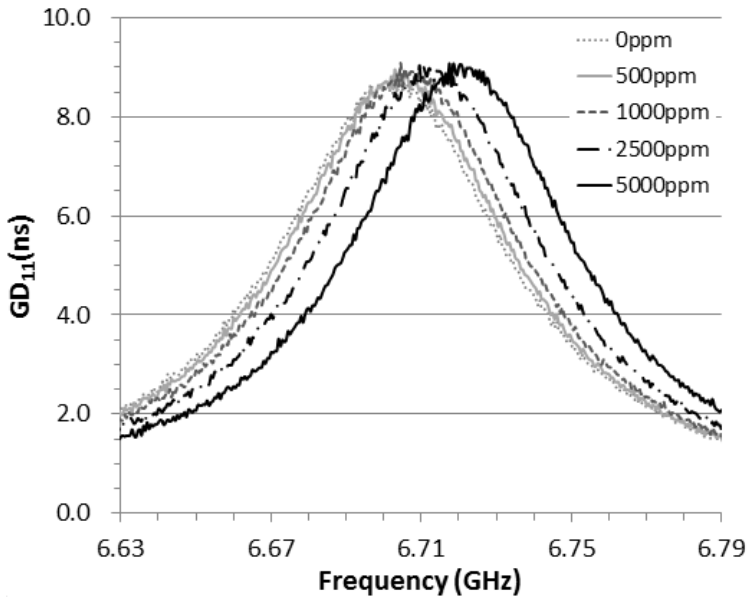

Fig. 3.6.7: Summary of GD_{11} response curves of OV-275 sensor.

3.6.2 Multi-Trial Sensor Response Analysis and Sensitivity Estimation

In order to examine the repeatability of the sensing performance and to obtain the linear estimation of the sensitivity curve for all the sensors, each sensor is tested under the exposure of a specific analyte in the concentration levels outlined in section 3.5 for at least 10 trials. Five selected trials that exhibit the highest collective linearity are then used for the linear approximation of the sensitivity curve. Fig. 3.6.8 to Fig. 3.6.10 illustrate a sequence of three examples of sensitivity curve approximations for the OV-275 sensor response against methanol exposure in terms of normalized shift in centre frequency ($\%\Delta f_0$), normalized change in S_{11} near centre frequency ($\%\Delta S_{11}$), and normalized change in GD_{11} near centre frequency ($\%\Delta GD_{11}$), respectively.

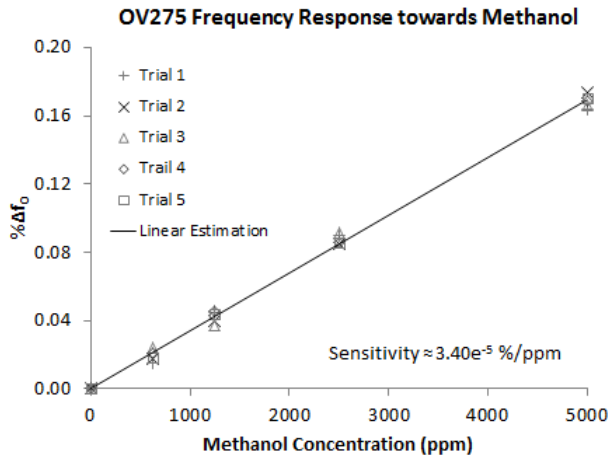

Fig. 3.6.8: OV275 normalized steady-state resonant frequency responses (%Δf_0) under methanol exposure.

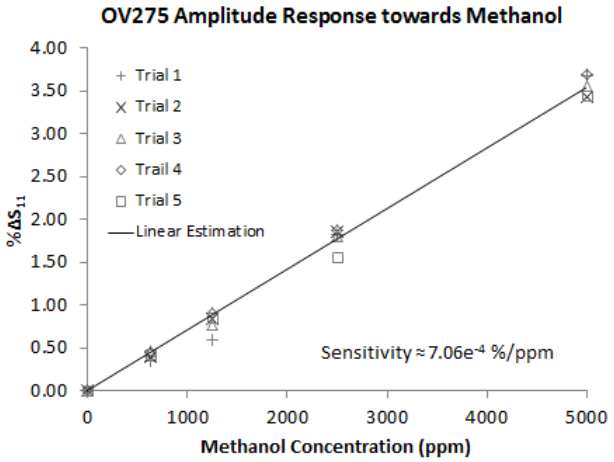

Fig. 3.6.9: OV275 normalized steady-state amplitude responses (%ΔS_{11}) under methanol exposure.

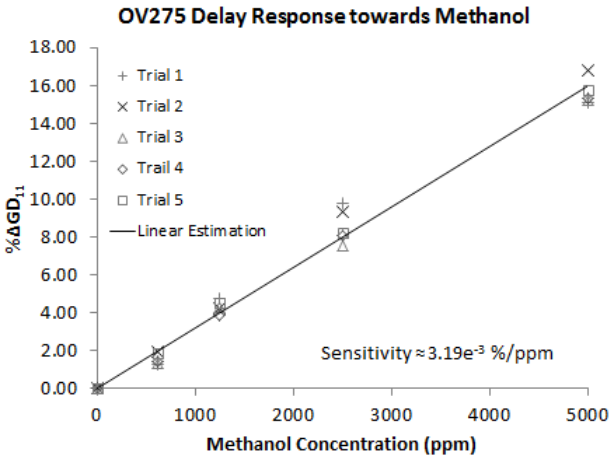

Fig. 3.6.10: OV275 normalized steady-state delay responses (%ΔGD_{11}) under methanol exposure.

From the three data sets, the OV-275 sensor has been characterized with three sensitivity parameters: A) Δf_0 sensitivity of 3.40E-5 %/ppm, B) ΔS_{11} sensitivity of 7.06E-4 %/ppm, and C) ΔGD_{11} sensitivity of 3.19E-3 %/ppm.

These sensitivity parameters are to be compared against those from other sensors under the exposures of different analyte gases, thereby obtaining the selectivity of the sensors with Eq. 2.1.

Fig. 3.6.11 to Fig. 3.6.13 illustrate another set of performance analysis for P25DMA under the exposures of ethanol. The P25DMA sensor under the exposures of ethanol has demonstrated the Δf_0 sensitivity of 1.47E-4 %/ppm, the ΔS_{11} sensitivity of 1.56E-3 %/ppm, and the ΔGD_{11} sensitivity of 3.30E-3 %/ppm.

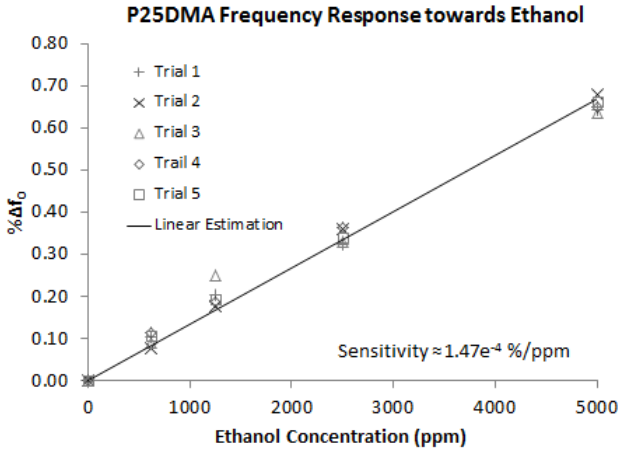

Fig. 3.6.11: P25DMA normalized steady-state resonant frequency responses (%Δf_0) under ethanol exposure.

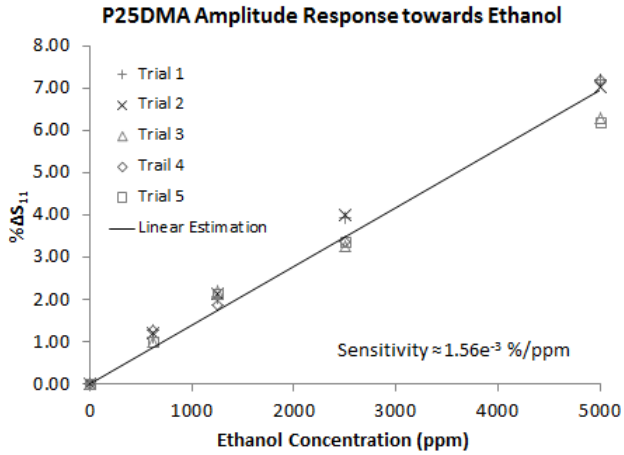

Fig. 3.6.12: P25DMA normalized steady-state amplitude responses (%ΔS_{11}) under ethanol exposure.

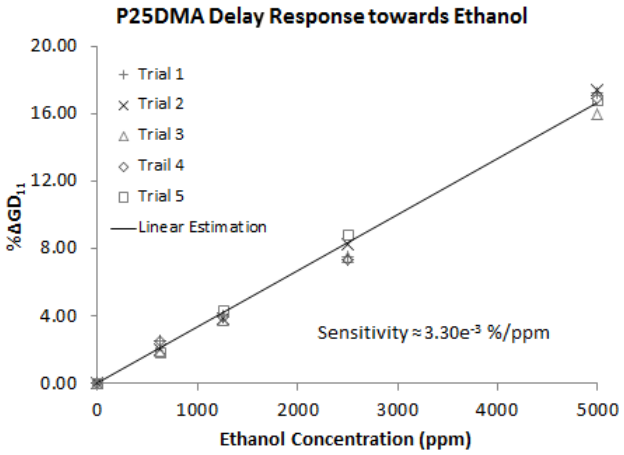

Fig. 3.6.13: P25DMA normalized steady-state delay responses (%ΔGD_{11}) under ethanol exposure.

Due to the large amount of data involved in characterizing the sensitivity of the sensors, the data presented in section 3.7 and section 3.8 are highly condensed and would only show the families of estimated sensitivity curves for cross-comparison purposes.

3.6.3 Baseline Drift and Noise Floor Calibration

Finally, prior to the full steady-state and transient characterizations of the resonant sensors, the baseline drift of the sensors were characterized under a constant nitrogen purge for 60 minutes. The S_{11} response of the sensor is recorded at an interval of 5 minutes. The percentage change of the S_{11} amplitude recorded near the resonant frequency is summarized in Fig. 3.6.14. The curve indicates a total initial baseline drift of 2% for the first 35 minutes of purge, but has stabilized afterwards. At the stabilized state, the sensor has seen less than a 0.2% fluctuation in S_{11} amplitude. As a result, all of the sensors were placed under a nitrogen purge for at least 40 minutes prior to the start of the experiment to ensure minimal baseline drift interference, and any recorded S_{11} shifts larger than 0.5% (2.5-times of the noise floor) were considered a valid sensor response. The recorded average noise throughout all the trials has a minimum interference of approximately 1ppm on the sensor reading [48].

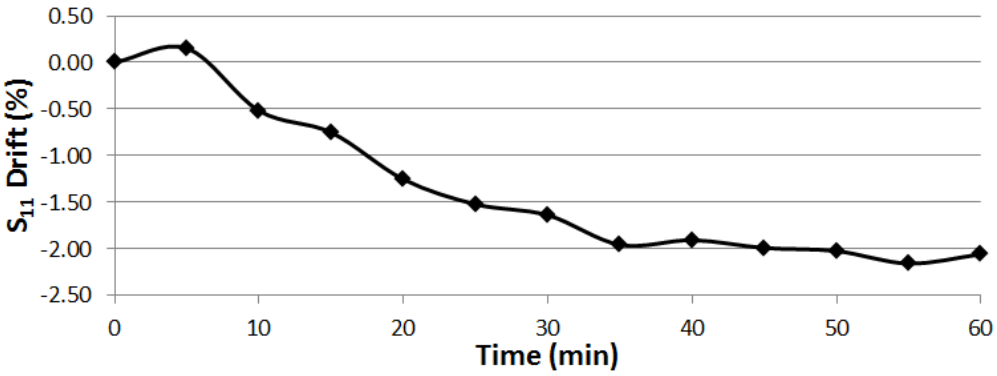

Fig. 3.6.14: Baseline drift and noise floor characterization of a selected RF resonant sensor under 60-minute nitrogen purge.

3.7 STEADY-STATE CHARACTERIZATION

3.7.1 Steady-State Resonant Frequency Shifts

A shift in f_0 resulting from the interaction between the polymeric sensing material and the gas analyte introduces changes in both S_{11} and GD_{11}. Fig. 3.7.1 to Fig. 3.7.3 show the normalized steady-state $\%\Delta f_0$ sensitivity curves for the siloxane-family sensors under exposure to methanol, ethanol, benzene and acetone, respectively. Figure 3.7.4 to Fig 3.7.6 show the sensitivity curves of the polyaniline-family sensors under the same exposure sequence.

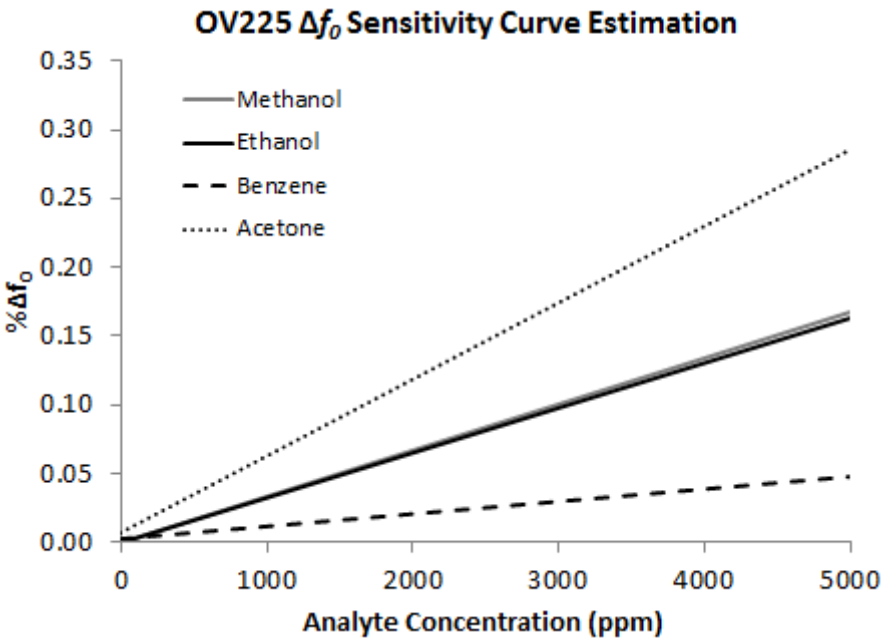

Fig. 3.7.1: OV225 %Δf_0 sensitivity curves under four gas analyte exposures.

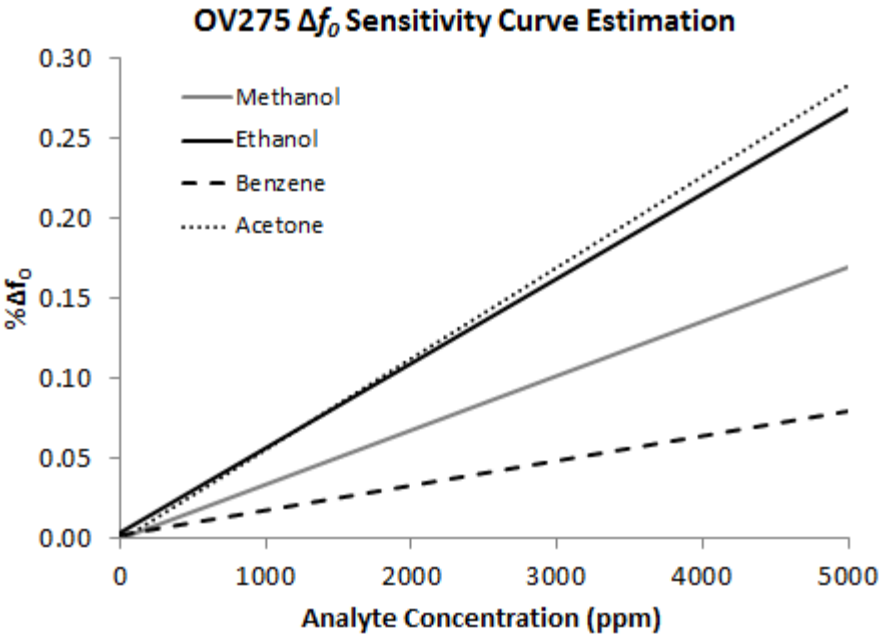

Fig. 3.7.2: OV275 %Δf_0 sensitivity curves under four gas analyte exposures.

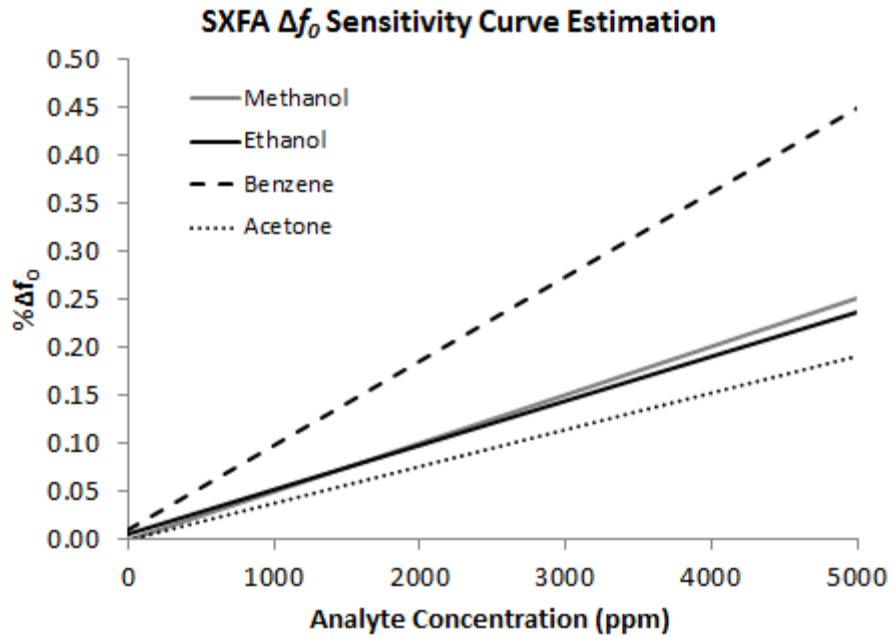

Fig. 3.7.3: SXFA %Δf_0 sensitivity curves under four gas analyte exposures.

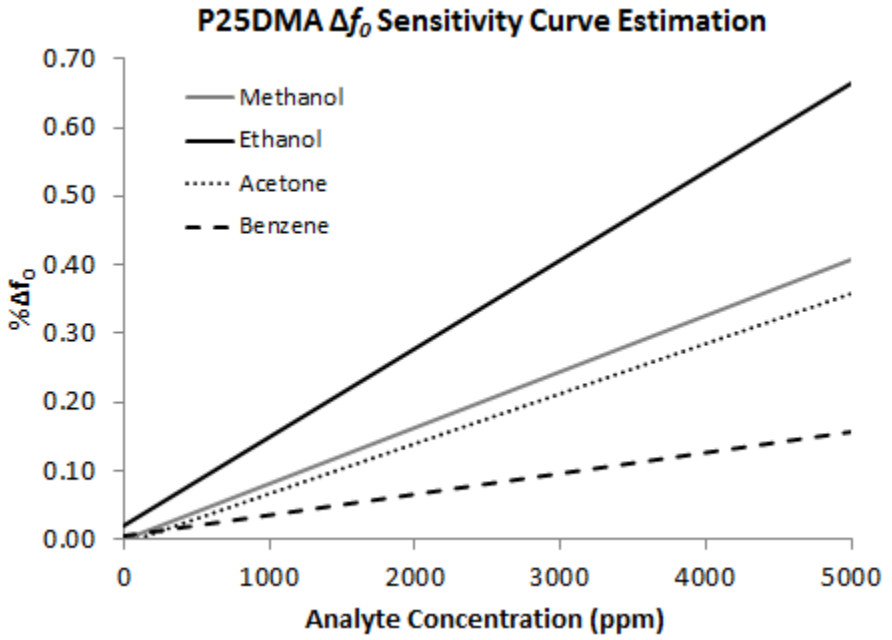

Fig. 3.7.4: P25DMA %Δf_0 sensitivity curves under four gas analyte exposures.

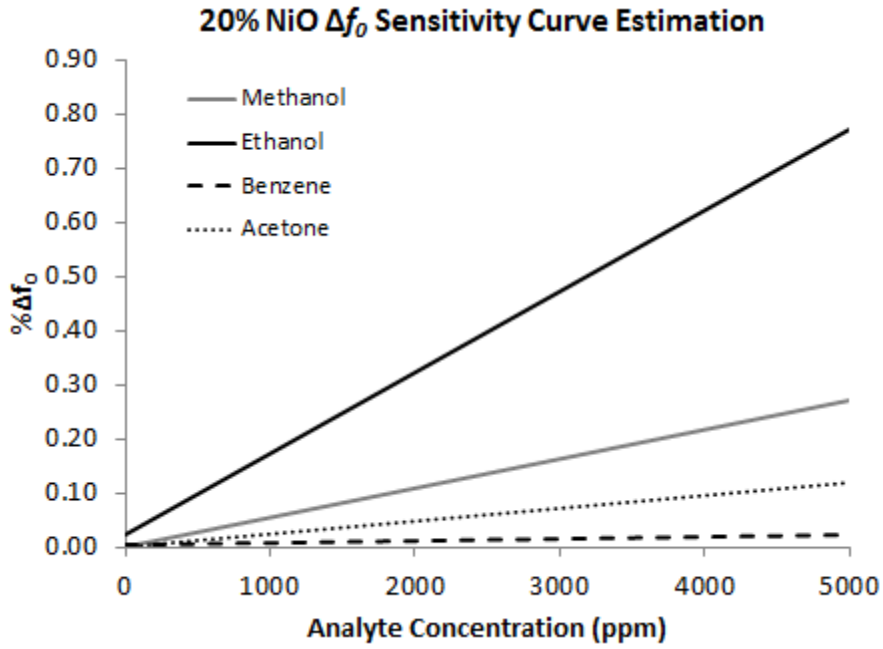

Fig. 3.7.5: P25DMA 20% NiO-Doped %Δf_0 sensitivity curves under four gas analyte exposures.

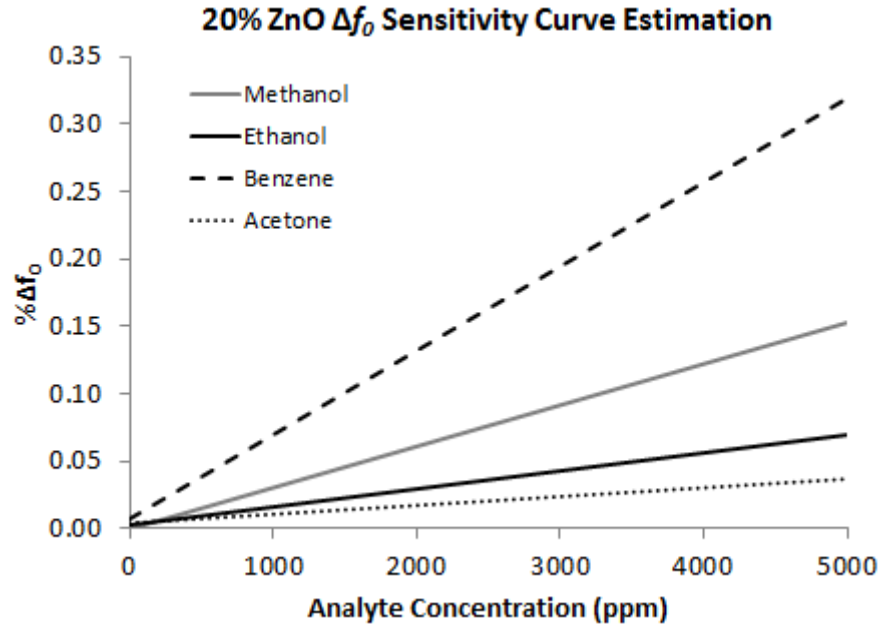

Fig. 3.7.6: P25DMA 20% ZnO-Doped% Δf_0 sensitivity curves under four gas analyte exposures.

The sensitivity values of each polymer to the analyte gases are summarized in Table 3.7.1 in terms of normalized percentage frequency shift. Across the entire table, only P25DMA 20% NiO-doped

shows a Δf_0 sensitivity level above 10^{-4} %/ppm; all other sensitivities recorded are in the 10^{-5} %/ppm range. It is worth noting that within the capability of our multipurpose chemical testing system, we are not able to precisely determine the concentration at which any of the sensors reach saturation, as no significant saturation responses were observed from the response curves within the range of 0-5000 ppm.

It is important to indicate that the following sensor testing conditions resulted in certain responses below the noise floor of the system. Furthermore, the sensitivity curves as well as their respective sensitivities are calculated based on the data points above the noise floor at the exposures of higher analyte concentrations.

1) OV225 against Benzene
2) OV275 against Benzene
3) P25DMA 20% NiO-doped against Benzene
4) P25DMA 20% ZnO-doped against Acetone

Table 3.7.1: Resonant Sensor Sensitivity Against the Three Gases in Terms of Normalized Frequency Shift

f_0 Sensitivity % Normalized	Methanol	Ethanol	Benzene	Acetone
OV225	3.72e^{-5} %/ppm	3.14e^{-5} %/ppm	1.17e^{-5} %/ppm	6.35e^{-5} %/ppm
OV275	3.33e^{-5} %/ppm	5.91e^{-5} %/ppm	1.71e^{-5} %/ppm	5.56e^{-5} %/ppm
SXFA	4.87e^{-5} %/ppm	5.09e^{-5} %/ppm	9.70e^{-5} %/ppm	3.73e^{-5} %/ppm
P25DMA	8.78e^{-5} %/ppm	1.47e^{-5} %/ppm	3.44e^{-5} %/ppm	6.82e^{-5} %/ppm
P25DMA 20% NiO	5.69e^{-5} %/ppm	1.67e^{-4} %/ppm	8.50e^{-6} %/ppm	2.45e^{-5} %/ppm
P25DMA 20% ZnO	3.23e^{-5} %/ppm	1.61e^{-5} %/ppm	6.75e^{-5} %/ppm	1.07e^{-5} %/ppm

3.7.2 Steady-State Amplitude Response

The response of a resonant sensor near resonance is known to be highly amplified when its ΔS_{11} and ΔGD_{11} are sampled instead of Δf_0. Fig. 3.7.7, to Fig. 3.7.12 show the normalized steady-state $\%\Delta S_{11}$ sensitivity curves of the six sensors against the four gas analytes.

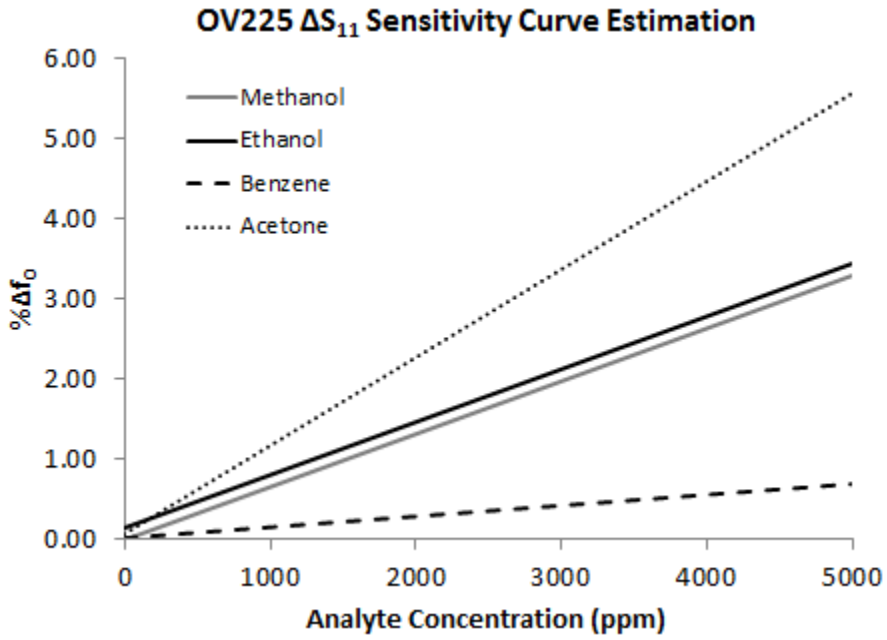

Fig. 3.7.7: OV225 $\%\Delta S_{11}$ sensitivity curves under four gas analyte exposures.

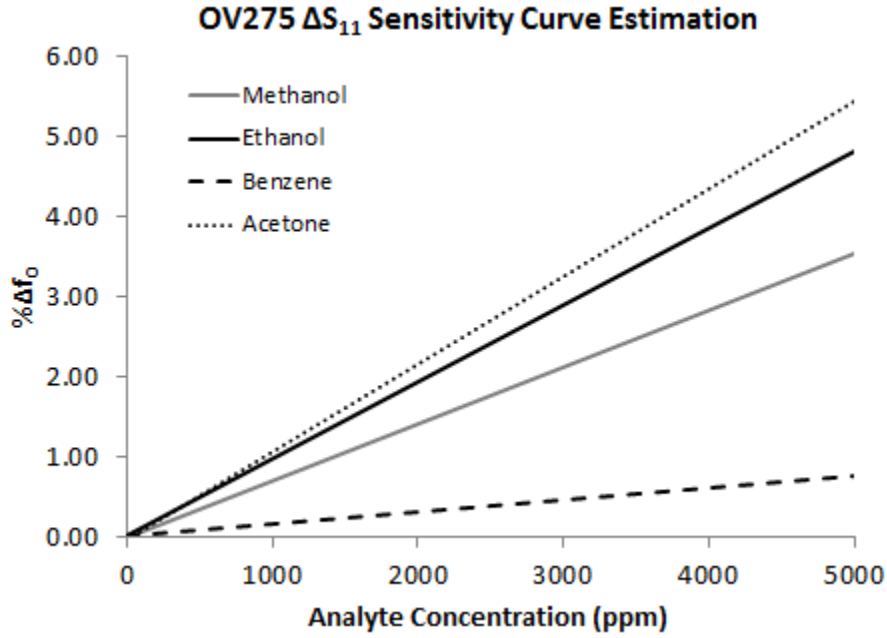

Fig. 3.7.8: OV275 $\%\Delta S_{11}$ sensitivity curves under four gas analyte exposures.

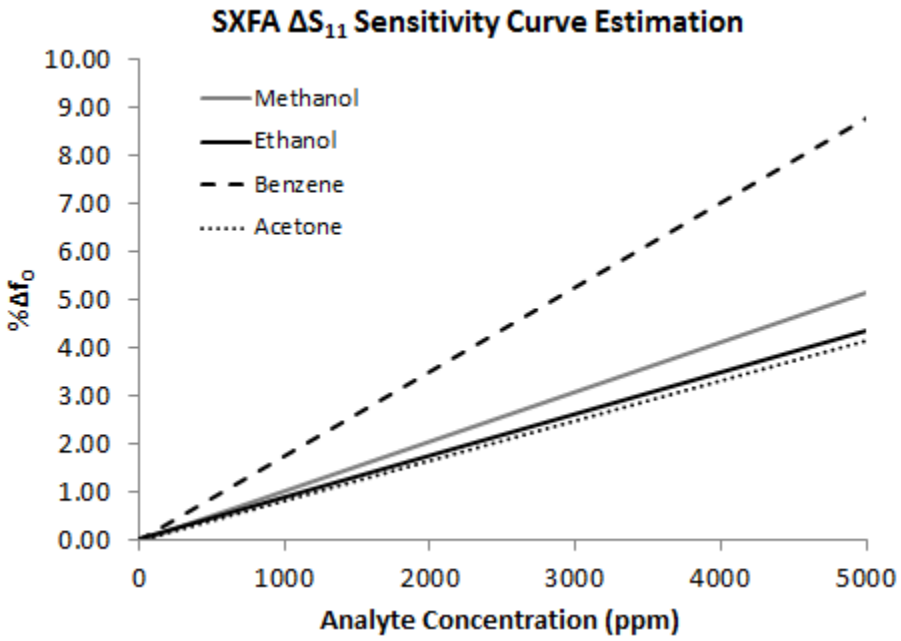

Fig. 3.7.9: SXFA %ΔS_{11} sensitivity curves under four gas analyte exposures.

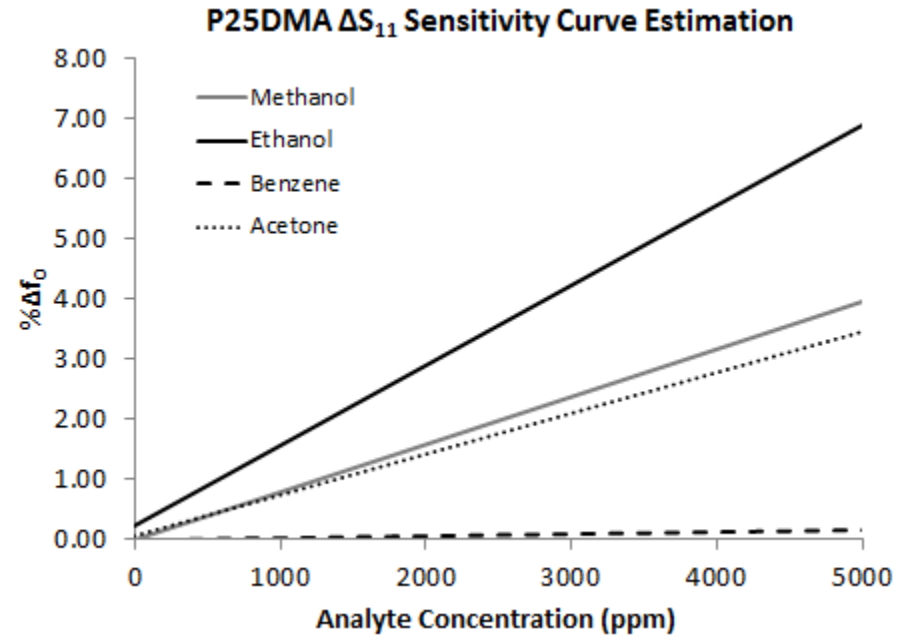

Fig. 3.7.10: P25DMA %ΔS_{11} sensitivity curves under four gas analyte exposures.

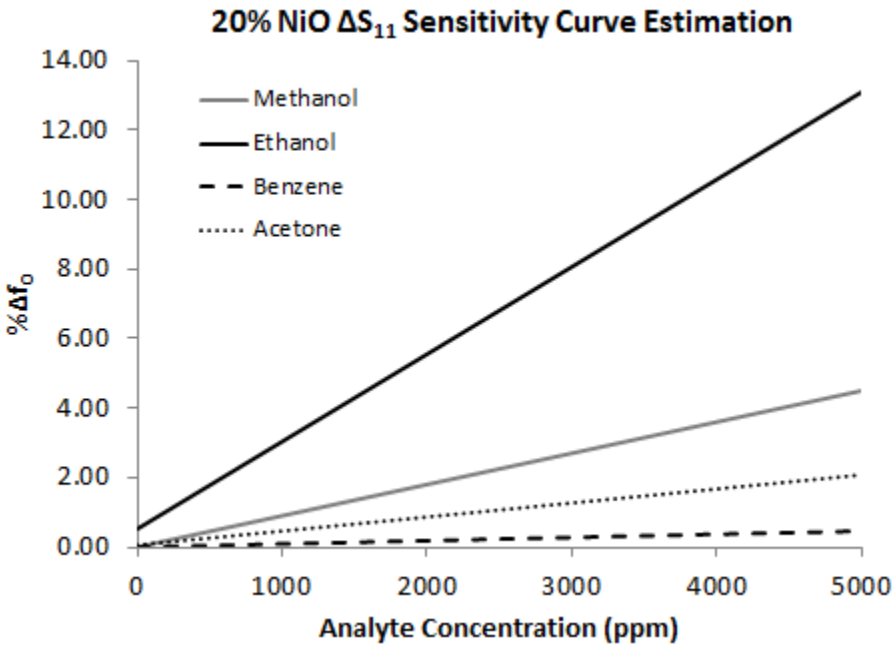

Fig. 3.7.11: -P25DMA 20% NiO-doped %ΔS_{11} sensitivity curves under four gas analyte exposures.

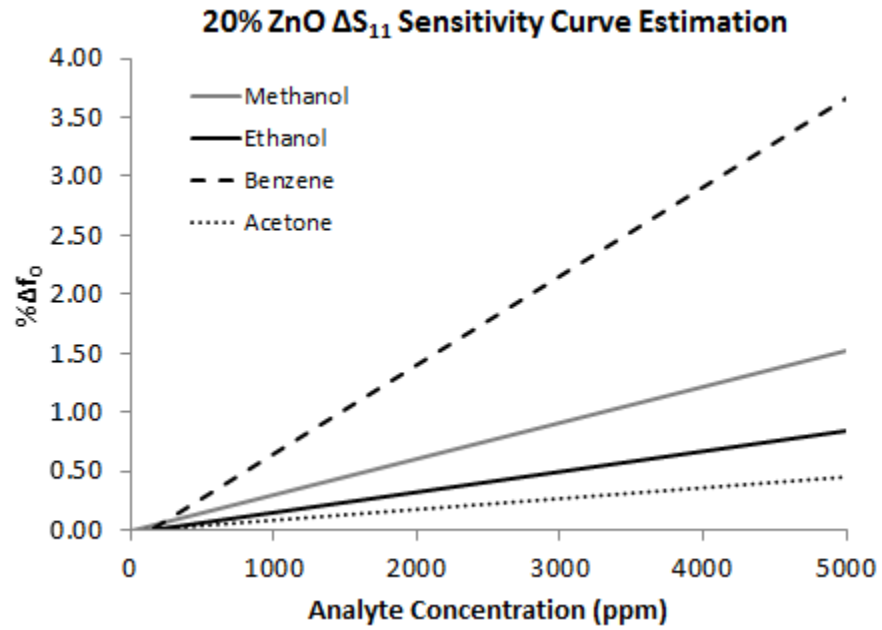

Fig. 3.7.12: P25DMA 20% ZnO-doped %ΔS_{11} sensitivity curves under four gas analyte exposures.

The amplitude response (%ΔS_{11}), as theory predicted, exhibited a much higher sensitivity under a small Δf_0. All ΔS_{11} sensitivity levels recorded are at least of one order of magnitude larger than their respective Δf_0 sensitivity levels, thereby validating the advantage of using the resonant sensor configuration. The collective data has also indicated that P25DMA and the 20% NiO-doped derivative have very high sensing performance against ethanol, and the 20% ZnO-doped derivative has been successfully customized to terminate the sensitivity of the P25DMA polyaniline chain against ethanol and other alcohol compounds. All siloxane polymers are highly responsive against acetone, as acetone is the better solvent compared to methanol and ethanol. Table 3.7.2 summarizes the normalized steady-state amplitude responses of the sensors against the gas analytes.

Table 3.7.2: Resonant Sensor Sensitivity Against the Three Gases in Terms of Normalized Amplitude Responses

S_{11} Sensitivity % Normalized	Methanol	Ethanol	Benzene	Acetone
OV225	6.71e^{-4} %/ppm	8.02e^{-4} %/ppm	1.47e^{-4} %/ppm	1.16e^{-3} %/ppm
OV275	6.81e^{-4} %/ppm	9.56e^{-4} %/ppm	1.70e^{-4} %/ppm	1.07e^{-3} %/ppm
SXFA	1.01e^{-3} %/ppm	9.08e^{-4} %/ppm	1.69e^{-3} %/ppm	8.17e^{-4} %/ppm
P25DMA	7.80e^{-4} %/ppm	1.56e^{-3} %/ppm	3.71e^{-5} %/ppm	7.39e^{-4} %/ppm
P25DMA 20% NiO	9.16e^{-4} %/ppm	3.15e^{-3} %/ppm	8.65e^{-5} %/ppm	4.77e^{-4} %/ppm
P25DMA 20% ZnO	2.83e^{-4} %/ppm	1.46e^{-4} %/ppm	6.33e^{-4} %/ppm	8.64e^{-5} %/ppm

3.7.3 Steady-State Delay Response

The other parameter expected to be highly sensitive to small ΔC, and the resultant Δf_0, is the response delay, GD_{11}. Fig. 3.7.13 to Fig. 3.7.18 show the normalized steady-state $\%\Delta GD_{11}$ sensitivity curves of the six sensors against the four gas analytes.

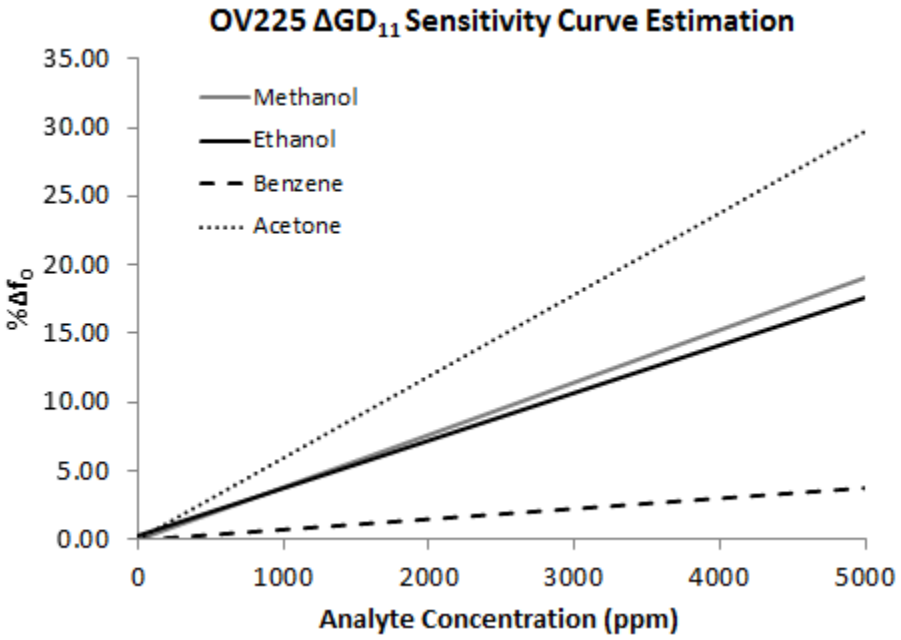

Fig. 3.7.13: OV225 $\%\Delta GD_{11}$ sensitivity curves under four gas analyte exposures.

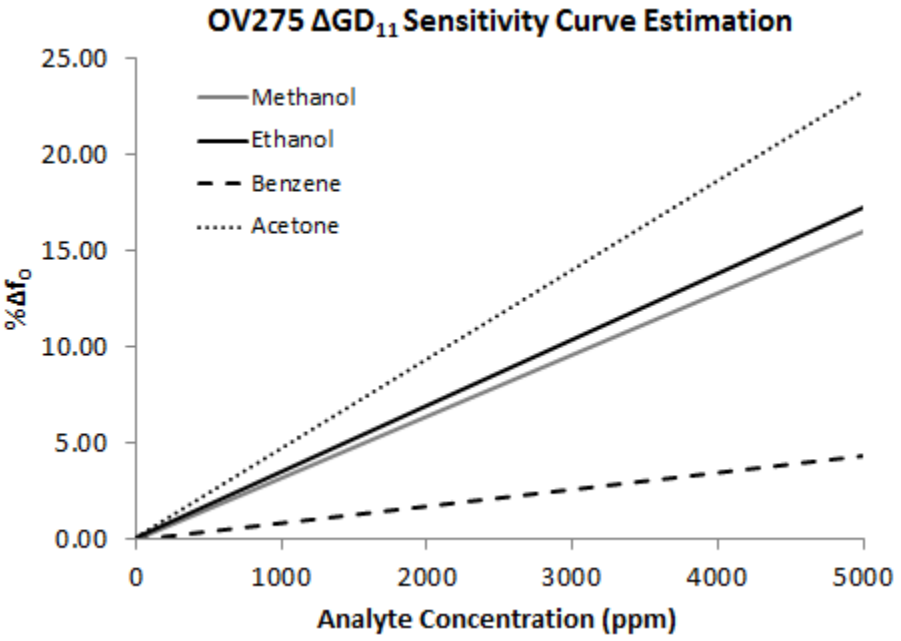

Fig. 3.7.14: OV275 $\%\Delta GD_{11}$ sensitivity curves under four gas analyte exposures.

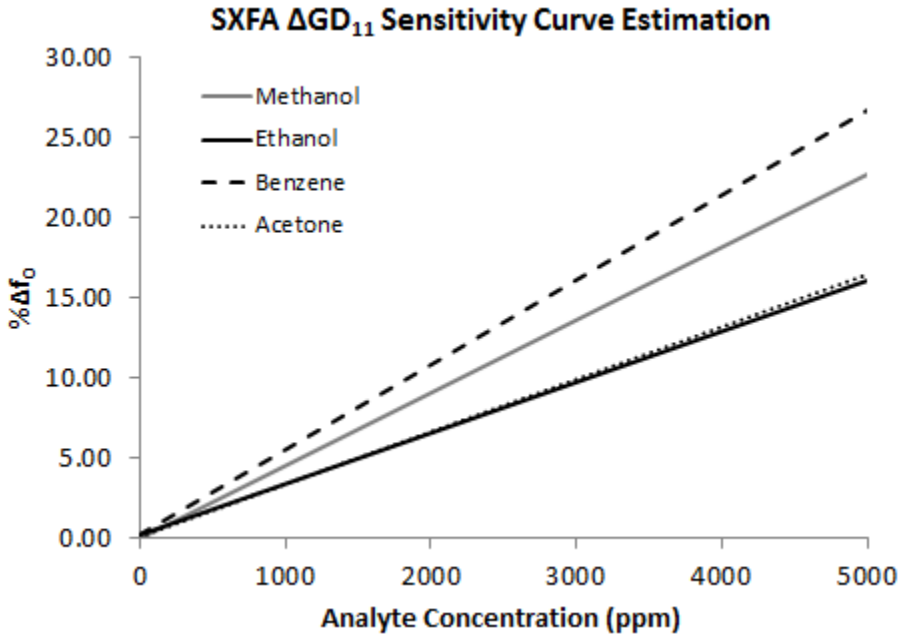

Fig. 3.7.15: SXFA $\%\Delta GD_{11}$ sensitivity curves under four gas analyte exposures.

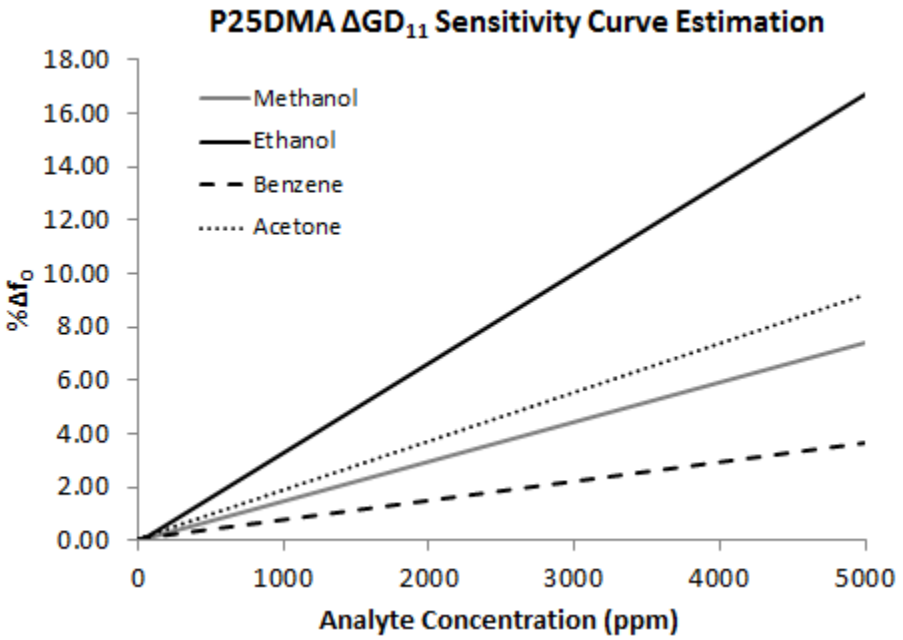

Fig. 3.7.16: P25DMA $\%\Delta GD_{11}$ sensitivity curves under four gas analyte exposures.

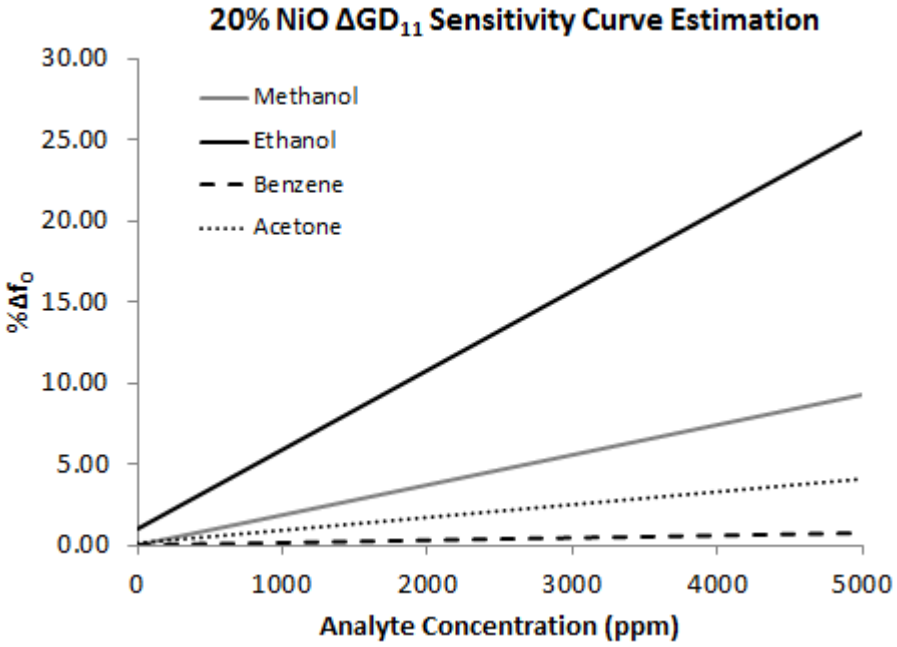

Fig. 3.7.17: P25DMA 20% NiO-doped %ΔGD_{11} sensitivity curves under four gas analyte exposures.

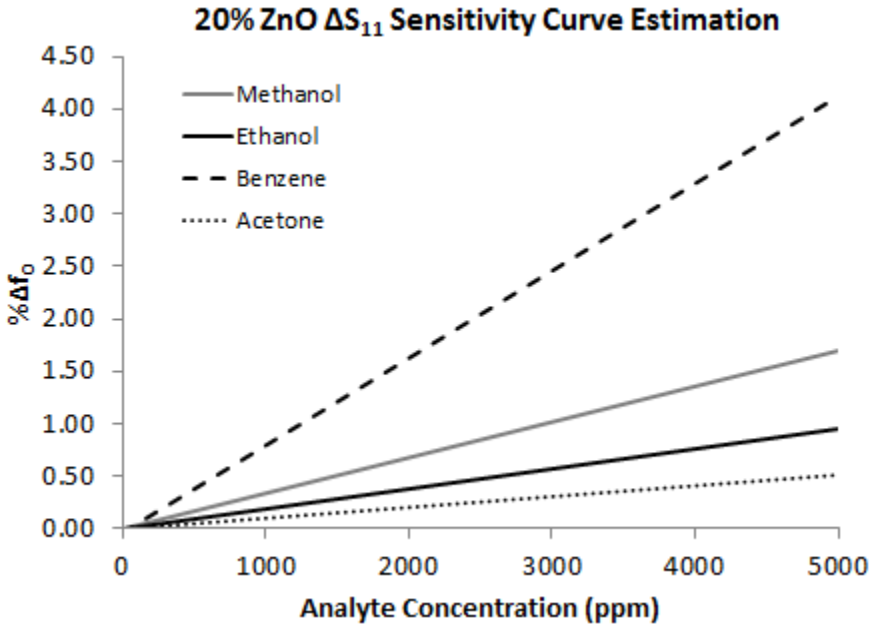

Fig. 3.7.18: P25DMA 20% ZnO-doped %ΔGD_{11} sensitivity curves under four gas analyte exposures.

The delay responses (GD_{11}) of the sensors have also shown very high sensitivity levels against gas analytes, with certain cases exhibiting even higher sensitivities than those obtained from S_{11}. It is important to note that the GD_{11} data points have seen more significant variations among different batches of sensors. This large discrepancy is due to variations in resonator coupling, which is mainly affected by the baseline capacitance of the chemi-capacitor after polymeric sensing functionalization. The problem of inconsistency could be improved by constant VNA characterization after each deposited layer of polymeric sensing material to ensure consistent coupling is achieved. In other words, the sensor performance should be unified by performance calibration, not by consistency in the thickness of the polymeric sensing material coating. Table 3.7.3 summarizes the normalized steady-state delay responses of the sensors against the gas analytes.

Table 3.7.3: Resonant Sensor Sensitivity Against the Three Gases in Terms of Normalized Delay Responses

GD_{11} Sensitivity % Normalized	**Methanol**	**Ethanol**	**Benzene**	**Acetone**
OV225	$3.65e^{-3}$ %/ppm	$3.70e^{-3}$ %/ppm	$7.55e^{-4}$ %/ppm	$5.84e^{-3}$ %/ppm
OV275	$3.14e^{-3}$ %/ppm	$3.55e^{-3}$ %/ppm	$8.62e^{-4}$ %/ppm	$4.67e^{-3}$ %/ppm
SXFA	$4.75e^{-3}$ %/ppm	$3.35e^{-3}$ %/ppm	$5.59e^{-3}$ %/ppm	$3.34e^{-3}$ %/ppm
P25DMA	$1.44e^{-3}$ %/ppm	$3.30e^{-3}$ %/ppm	$7.58e^{-4}$ %/ppm	$1.86e^{-3}$ %/ppm
P25DMA 20% NiO	$1.91e^{-3}$ %/ppm	$5.63e^{-3}$ %/ppm	$1.68e^{-4}$ %/ppm	$8.79e^{-4}$ %/ppm
P25DMA 20% ZnO	$3.37e^{-4}$ %/ppm	$1.91e^{-4}$ %/ppm	$7.92e^{-4}$ %/ppm	$1.03e^{-4}$ %/ppm

3.8 TRANSIENT-STATE CHARACTERIZATION

The transient analysis is conducted with ΔS_{11} and ΔGD_{11}, since these two parameters yield higher sensitivities compared to Δf_0. Fig. 3.8.1 to Fig. 3.8.6 show the ΔS_{11} transient responses of the six sensor prototypes against the four gas analytes.

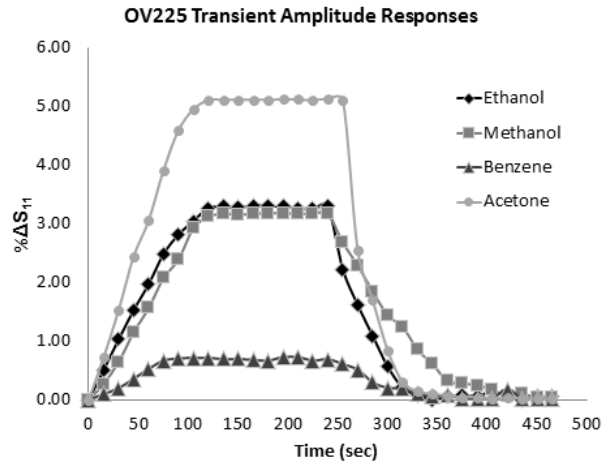

Fig. 3.8.1: Normalized transient amplitude responses ($\%\Delta S_{11}$) of OV225 sensor against four gas analytes.

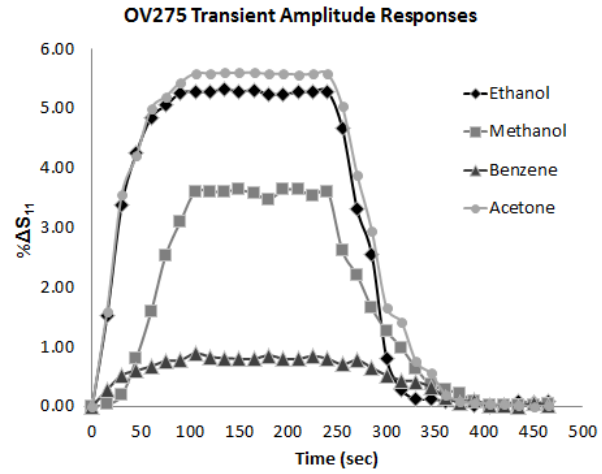

Fig. 3.8.2: Normalized transient amplitude responses ($\%\Delta S_{11}$) of OV275 sensor against three gas analytes.

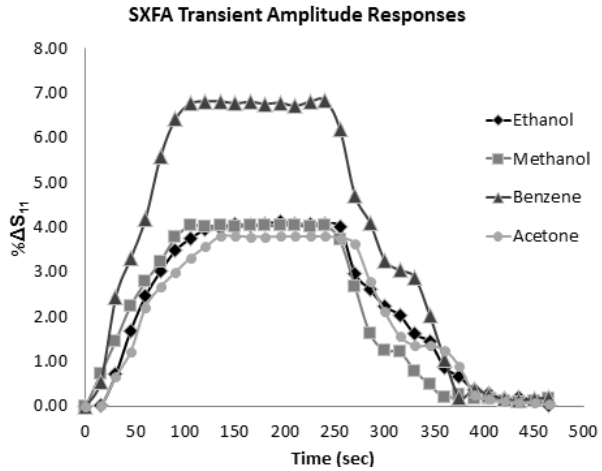

Fig. 3.8.3: Normalized transient amplitude responses (%ΔS_{11}) of SXFA sensor against three gas analytes.

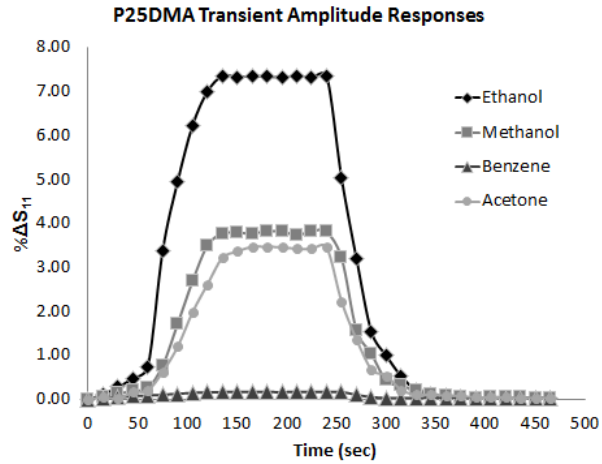

Fig. 3.8.4: Normalized transient amplitude responses (%ΔS_{11}) of P25DMA sensor against four gas analytes.

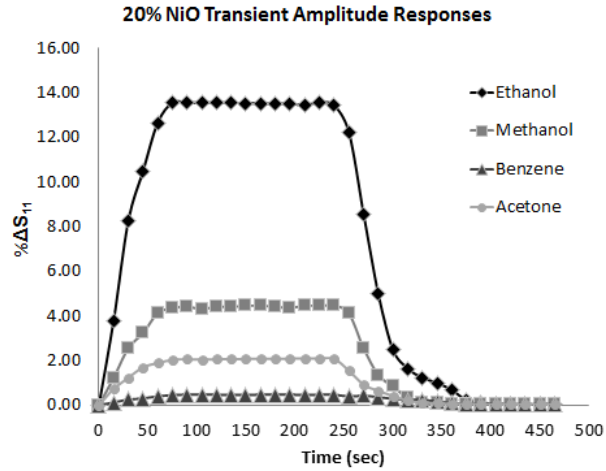

Fig. 3.8.5: Normalized transient amplitude responses (%ΔS_{11}) of 20% NiO sensor against three gas analytes.

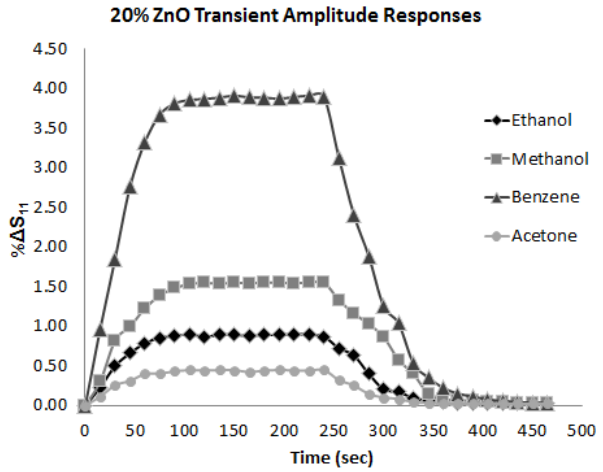

Fig. 3.8.6: Normalized transient amplitude responses ($\%\Delta S_{11}$) of 20% ZnO sensor against three gas analytes.

The transient responses not only illustrate the response and recovery characteristics of each polymer against the gas analytes, but also indicate the transient chemical signature of the four gas analytes on the polymeric sensing materials. The response and recovery time constants are summarized in Table 4. Next, Fig. 3.8.7 to Fig. 3.8.12 show the ΔGD_{11} transient responses of the six sensor prototypes against the four gas analytes.

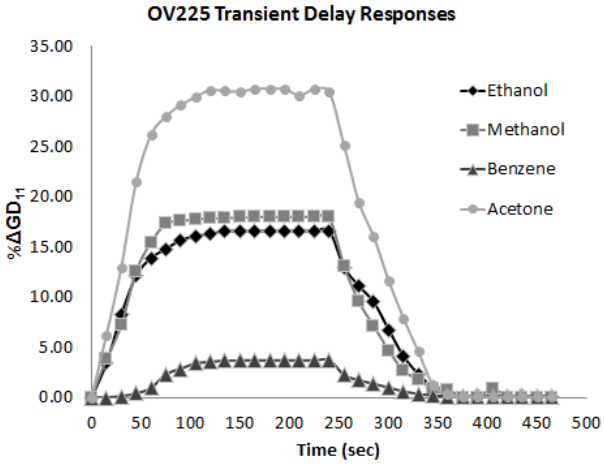

Fig. 3.8.7: Normalized transient delay responses ($\%\Delta GD_{11}$) of OV225 sensor against three gas analytes.

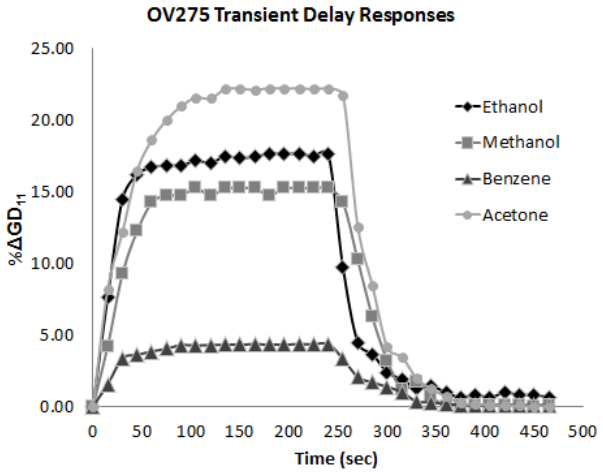

Fig. 3.8.8: Normalized transient delay responses ($\%\Delta GD_{11}$) of OV275 sensor against three gas analytes.

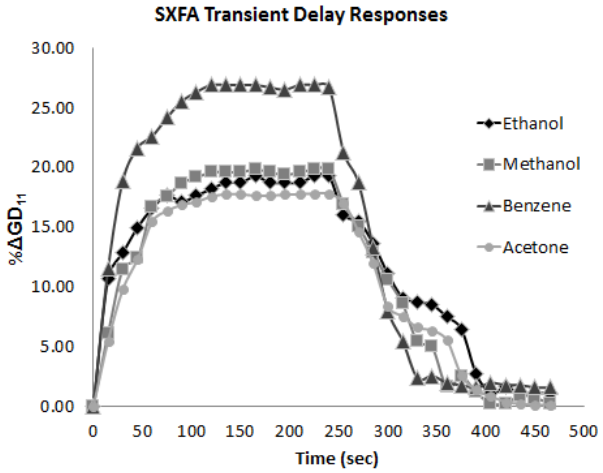

Fig. 3.8.9: Normalized transient delay responses ($\%\Delta GD_{11}$) of SXFA sensor against three gas analytes.

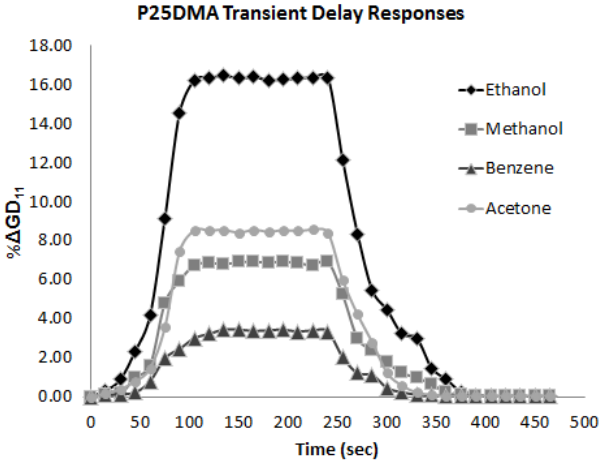

Fig. 3.8.10: Normalized transient delay responses ($\%\Delta GD_{11}$) of P25DMA sensor against three gas analytes.

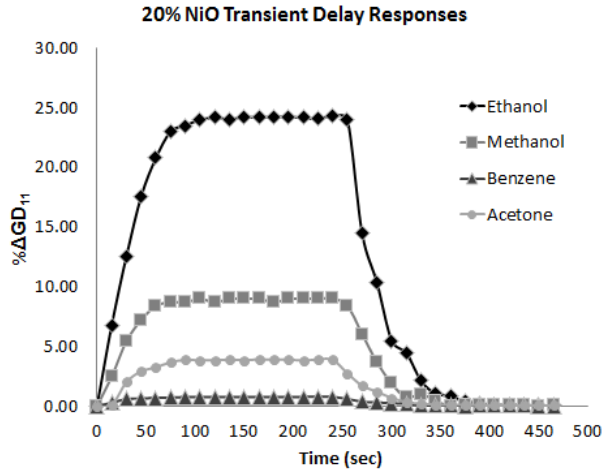

Fig. 3.8.11: Normalized transient delay responses ($\%\Delta GD_{11}$) of 20% NiO sensor against three gas analytes.

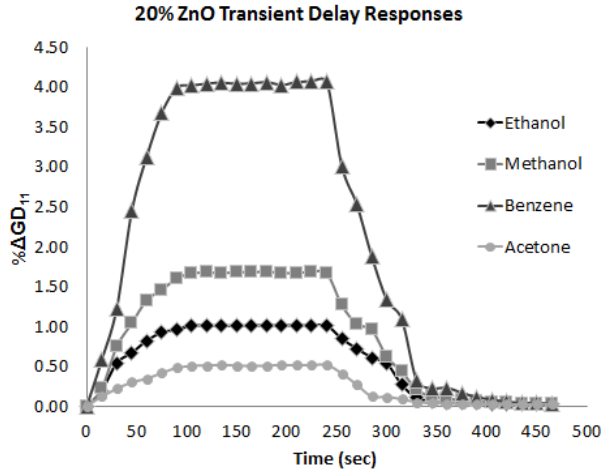

Fig. 3.8.12: Normalized transient delay responses ($\%\Delta GD_{11}$) of 20% ZnO sensor against three gas analytes.

Finally, the response and recovery time characteristics of the six polymeric sensing materials are summarized in Table 3.8.1. Since the smallest time step achievable by the VNA was 15 seconds, the characteristics were determined in 15 second units. Generally, the polyaniline family has exhibited a faster response and recovery time against the gaseous analytes compared to the siloxane family. Moreover, the recovery time of the siloxane family has exhibited significant variations not only among different analytes, but also among different trials of the same analyte exposures. This phenomenon is the result of multiple sorption mechanisms of the siloxane-based polymers, where absorption and adsorptions can take place simultaneously at different bonding locations in the polymer, thus slowing down the release of the analytes from the polymer during the recovery process. The variation in recovery time has also been observed for the polyaniline family, but at a lower extent. To improve the consistency of the recovery process of the polymer, light heating may

be applied to the polymer to help accelerate the analyte release process. Finally, the transient performance of these polymeric sensing materials was found to deteriorate with time. The siloxane-based polymers have lost their sensing performance after an average of 6 months after deposit. Similarly, the polyaniline-based crystalline polymers have seen a drop in sensing performance but have not fully lost their responsiveness against the analytes for the 1-year experiment period.

Table 3.8.1: Estimated Response and Recovery Characteristics of the Six Resonant Sensors

	Transient Characteristics	Methanol	Ethanol	Benzene	Acetone
OV225	*Response Time,* t_r	75s	75s	60s	75s
	Recovery Time, t_d	105s	45s	90s	45s
	Response Time Constant, τ	60s	60s	45s	60s
OV275	*Response Time,* t_r	75s	75s	75s	75s
	Recovery Time, t_d	90s	135s	135s	90s
	Response Time Constant, τ	45s	60s	60s	60s
SXFA	*Response Time,* t_r	75s	75s	75s	90s
	Recovery Time, t_d	90s	120s	105s	105s
	Response Time Constant, τ	60s	45s	45s	60s
P25DMA	*Response Time,* t_r	45s	60s	105s	60s
	Recovery Time, t_d	60s	60s	45s	60s
	Response Time Constant, τ	30s	60s	75s	45s
P25DMA 20% NiO-Doped	*Response Time,* t_r	45s	45s	60s	45s
	Recovery Time, t_d	45s	60s	90s	60s
	Response Time Constant, τ	30s	30s	45s	30s
P25DMA 20% ZnO-Doped	*Response Time,* t_r	75s	60s	60s	60s
	Recovery Time, t_d	90s	90s	90s	75s
	Response Time Constant, τ	45s	30s	30s	45s

3.9 SELECTIVITY AND CHEMICAL SIGNATURES

The selectivities of the six polymeric sensing materials (OV225, OV275, SXFA, P25DMA, P25DMA with 20% NiO-Doped, and P25DMA with 20% ZnO-Doped) with respect to the target analyte of ethanol against the three interferents, methanol, benzene, and acetone (measured at 5000 ppm for each gas analyte) are evaluated with Eq. 2.1. They are then presented in three normalized RF characteristic parameters, $\%\Delta f_0$, $\%\Delta S_{11}$, and $\%\Delta GD_{11}$, as shown in Fig. 3.9.1 to Fig. 3.9.6. Furthermore, the chemical signatures of the four analytes on the sensing materials are also summarized in the respective figures.

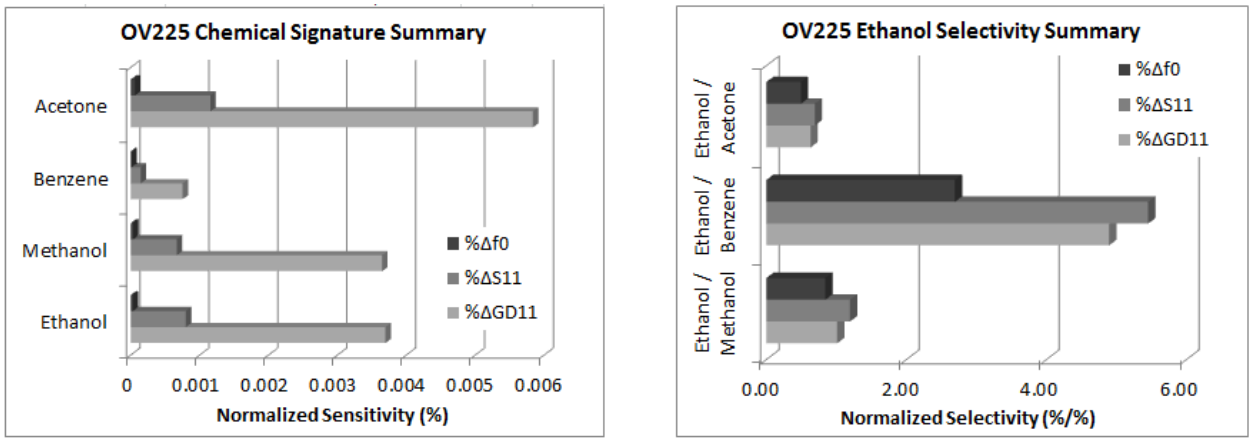

Fig. 3.9.1: Chemical signature summary (left) and selectivity summary (right) for OV225 resonant sensor.

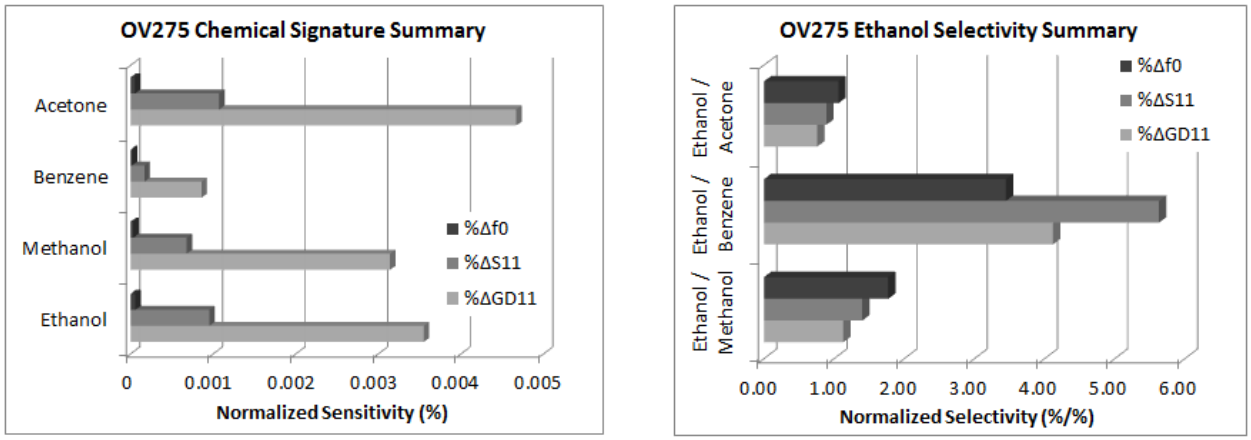

Fig. 3.9.2: Chemical signature summary (left) and selectivity summary (right) for OV275 resonant sensor.

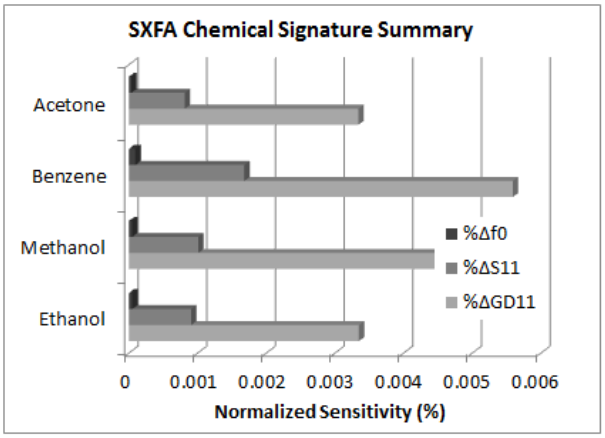

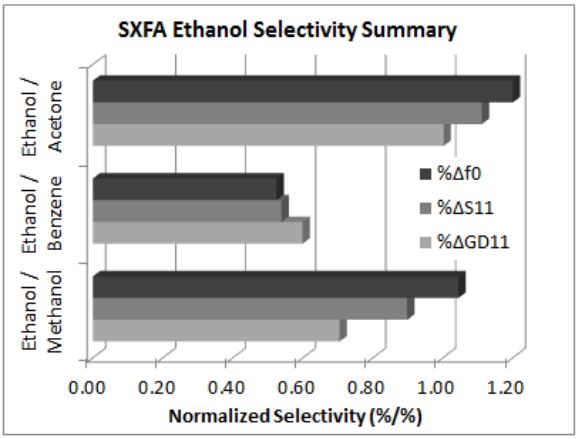

Fig. 3.9.3: Chemical signature summary (left) and selectivity summary (right) for SXFA resonant sensor.

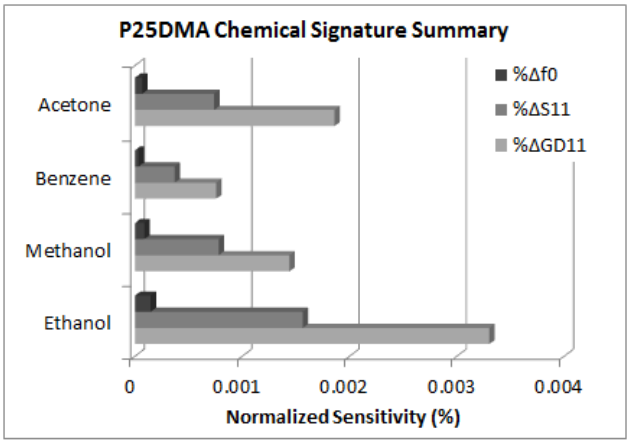

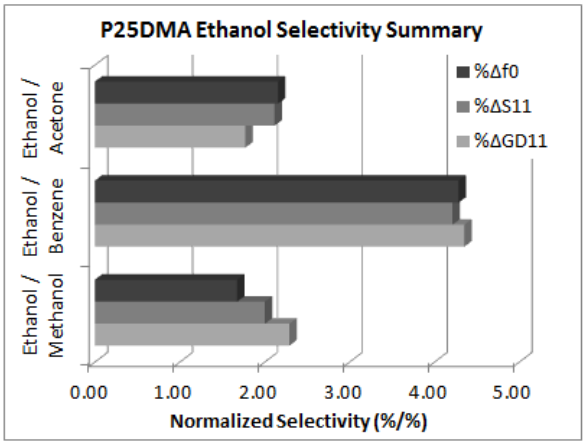

Fig. 3.9.4: Chemical signature summary (left) and selectivity summary (right) for P25DMA resonant sensor.

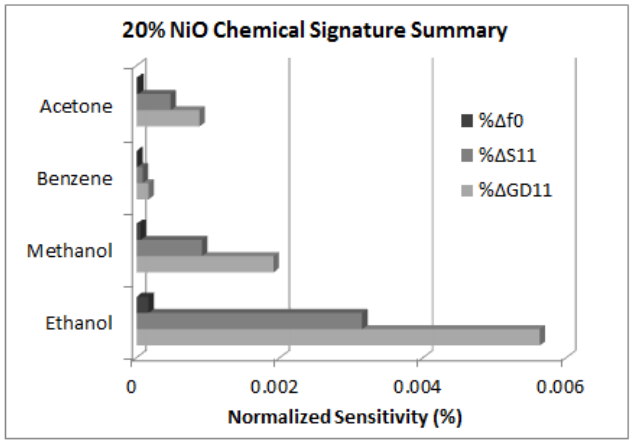

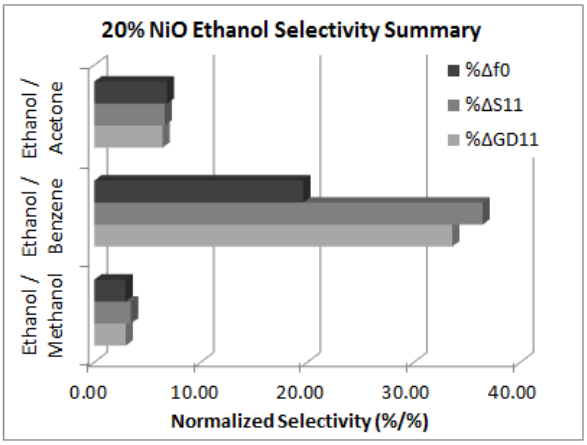

Fig. 3.9.5: Chemical signature summary (left) and selectivity summary (right) for 20% NiO resonant sensor.

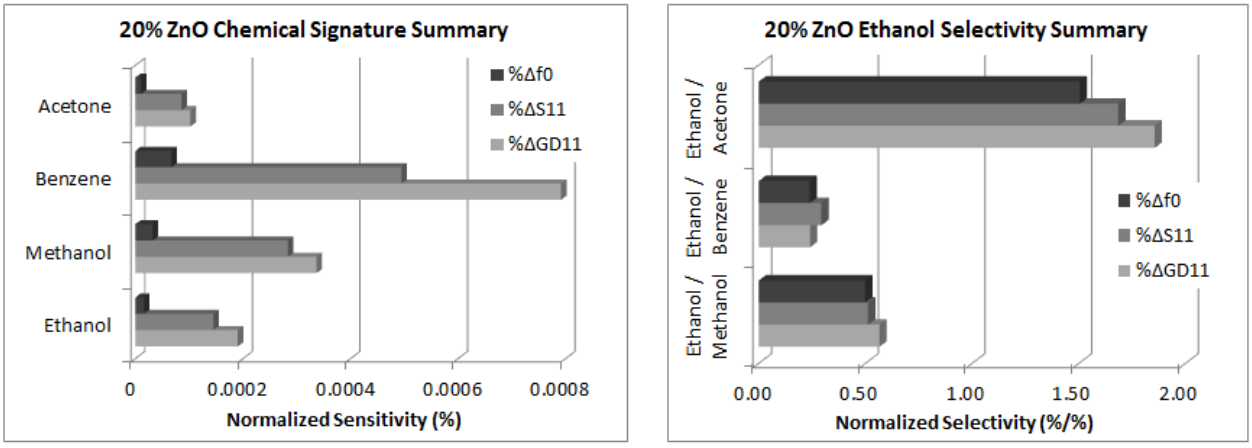

Fig. 3.9.6: Chemical signature summary (left) and selectivity summary (right) for 20% ZnO resonant sensor.

From the selectivity analysis above, several meaningful interpretations can be made to help predict the behaviors of the individual sensors to be integrated into arrays in the next chapter. As far as the application of ethanol identification is concerned, in the siloxane sensors, OV225 and OV275 are both very selective against benzene, but cannot clearly differentiate methanol from ethanol. Both OV-series siloxane polymers are, however, showing selectivity less than one against acetone, indicating that both polymers are more responsive towards acetone than towards the alcohol compounds. SXFA, on the other hand, shows higher responsiveness against benzene, but cannot clearly differentiate ethanol, methanol, and acetone from each other. Among the three siloxane polymers, OV275 is the best polymer for identifying the presence of ethanol; the other two can be used in conjunction to help identify the presence of benzene.

In contrast, the polyaniline crystalline sensors exhibited significantly higher selectivities against their targeted analytes. The general form of P25DMA showed high selectiveness towards ethanol against benzene, an acceptable selectivity of two-to-one against acetone and methanol. The 20% NiO-doped derivative showed even more enhanced ethanol selectivity against other analytes, and the 20% ZnO-doped derivative demonstrated very low responsiveness towards ethanol. Both of these phenomena agree with the intended functionalization goals presented in Table 3.4.3, where the NiO-doped P25DMA is designed for enhanced ethanol response and ZnO-doped P25DMA for inhibited ethanol response. All three polymers from the polyaniline family can be used in combination to detect the presence of ethanol and the interferents presented in this chapter.

3.9 SUMMARY

RF resonant sensors with six polymeric sensing materials (OV225, OV275, SXFA, P25DMA, P25DMA with 20% NiO-dopant, and P25DMA with 20% Zno-Dopant) were characterized with four gas analytes – methanol, ethanol, benzene and acetone – in terms of Δf_0, ΔS_{11}, and ΔGD_{11}. Based on their steady-state behaviour, the gas analytes and the polymeric sensing materials exhibited unique response signatures and selectivity characteristics, which is useful for post-readout chemical signature analysis and for the construction of sensor arrays for various field applications. The transient responses captured the response and recovery characteristics of the sensors. The polymeric sensing materials from the polyaniline family exhibited a shorter response and recovery time than the siloxane family. With constant nitrogen purge at room temperature, all the sensing materials, especially the siloxane-based ones, exhibited an inconsistent recovery time among different experimental trials; this issue can be resolved by slight temperature elevation on the polymer to help accelerate the desorption process. The advantages of the undercoupled resonant sensor are clearly illustrated by the measured ΔS_{11} and ΔGD_{11}, both of which are at least one order of magnitude larger than the respective Δf_0. To improve on the consistency of the sensor response in future prototype fabrication, the RF characteristics should be inspected between every deposited layer of the polymeric sensing material coating. Finally, the selectivity analysis indicated that all six polymers have a certain level of capability to differentiate specific analytes from others. Thus, as far as the sample application is concerned, all six polymeric sensing materials can be deposited onto sensor arrays for epidermal ethanol detection and the detection of benzene, methanol and acetone as interferents.

CHAPTER 4
3D CAVITY-BASED HIGH SENSITIVITY CHEMICAL SENSOR

4.1 INTRODUCTION

This chapter presents an alternative RF resonant sensor structure implemented with the combline mode cavity resonator. The design of the polymeric sensing material-based cavity resonator sensor allows seamless integration with existing chemical and biomarker sensing systems with sample delivery pipeline networks. Both the 3D design presented in this chapter and the planar design in Chapter 3 can be integrated into sensor arrays for electronic nose applications.

The concept of an RF resonant sensor was patented in the late 1990s for wireless device applications [27]. In subsequent work, the planar RF resonant sensors were employed in various gaseous and aqueous sensing applications [28, 45]. These works mainly focused on implementing the chemi-capacitive sensing elements to the capacitive component of a planar RF resonator. However, the planar resonators are fundamentally limited by their lower Q-factors; accompanied by

the high loss of the sensing materials used in these designs, the resultant sensors can only achieve an average resonant amplification factor of approximately 100 (calculated by $\%\Delta S_{11}$ / $\%\Delta f_0$) [20].

While material loss is an inevitable issue with cavity resonators, they naturally have a significantly higher Q than planar resonators [29], and thus can potentially be used as resonant sensors for high-sensitivity applications. The RF resonant cavity has been used as a liquid analyte concentration sensor in [44], where the cavity was injected with a constant flow of liquid analyte solution. The shift in resonant frequency (f_0) of the cavity indicated the change in analyte concentration in the solution. A 4-pole combline RF filter was modified in [43] for high-precision chamber airflow detection by replacing the housing cap with a thin copper-polymer bilayer membrane to allow mechanical interactions with the airflow.

With these works in mind, this chapter presents a polymeric sensing material-coated combline cavity resonant gaseous analyte sensor designed to be integrated with chemical gas pipelines for the detection of volatile organic compounds (VOCs) and their respective concentrations. The resonant sensor is designed to accommodate gaseous analyte inflow into the cavity body, allowing the analyte to influence the polymeric sensing materials coated on the combline post, thereby affecting the f_0 of the resonant sensor. With the high Q of the cavity resonator, the small shift in f_0 translates into a significant change in the return loss (S_{11}) of the resonant sensor, thus achieving an in-line gas sensor with high sensitivity for various different chemical and biomedical applications, including wearable devices.

4.2 POLYER-COATED COMBLINE RESONANT CHEMICAL SENSOR

Fig. 4.2.1 illustrates a conventional combline cavity resonator with the tip of the metal post coated with polymeric sensing material. The electric field in the combline resonator concentrates mainly around the post and the gap between the top of the post and the housing ceiling. Any changes in the dielectric constant of the polymeric materials would result in a shift in f_0. [29]

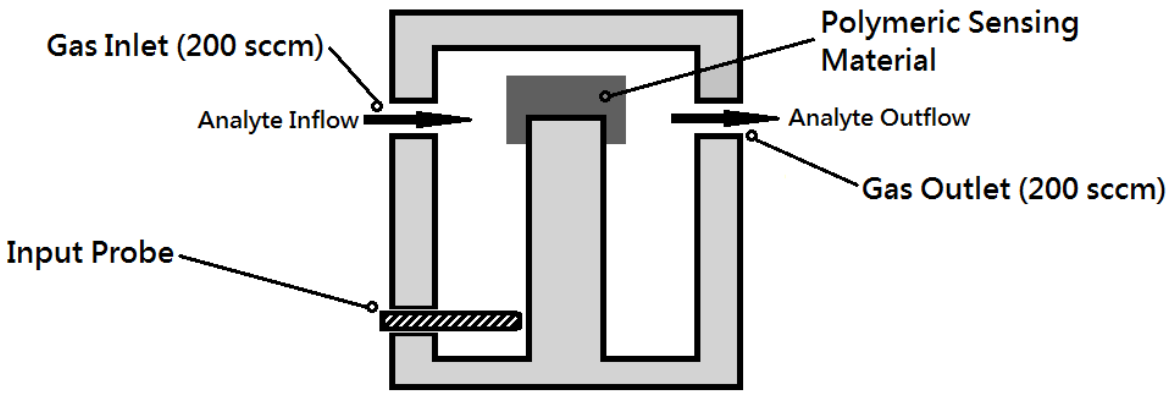

Fig. 4.2.1. RF combline cavity resonator and the corresponding model.

The bare cavity resonator by itself is sensitive to changes in analyte concentration in the cavity free space, which subsequently affects the effective dielectric constant of the free space and the resonant frequency of the resonator. However, this change lacks critical differentiation among analytes with similar dielectric constants. To address this shortcoming, a polymeric sensing material coating is applied to the tip of the combline, as shown in Fig. 1. The loading due to the polymeric material coating consequently becomes sensitive to selected chemical compounds. Most polymeric sensing materials undergo changes in $\varepsilon_{r,poly}$ and physical volume after analyte sorption [55], both of which contribute to changes in the cavity resonant frequency. In this way, the resonant sensor can be functionalized to enhance its response against specific analytes with selected polymer coatings.

4.3 FABRICATION AND CHARACTERIZATION SETUP

Fig. 4.3.1 shows the unassembled polymer-coated combline cavity filter designed to operate around 4 GHz with a measured unloaded quality factor of 880 (51% of the simulated theoretical value, due to the quality of copper plating and machining surface roughness). The cavity and the probe dimensions are designed in Ansoft HFSS for optimal cavity sensor size and loaded Q, and then fabricated with aluminum housing followed by ~50 μm electroplated copper to reduce the material loss. Two through holes (Inlet: 1/8" OD, 1/16" ID. Outlet: 1/16" OD) are opened on opposite side walls of the cavity to allow gas-line integration with the multipurpose gas characterization system used in [20], [55] and [56].

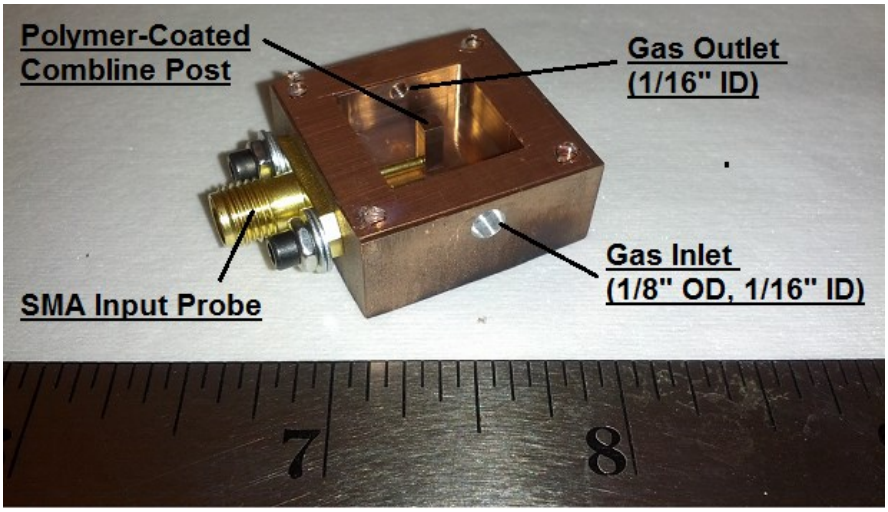

Fig. 4.3.1. Fabricated RF combline cavity resonant sensor.

The two selected polymeric sensing materials (namely, OV-275 [siloxane-based] and 20 wt. % NiO-doped poly [2,5-dimethyl aniline] [P25DMA]) were dissolved in acetone and *N*-methyl-2-pyrrolidone (NMP) (10 w.t. % solutions) before being deposited onto the tip of the combline post (2 mm x 2 mm), forming a polymer coating of approximately 40 μm in thickness. Both polymers are known to be responsive to certain VOCs and have low loss below 5 GHz. To remove all solvent, polymer curing was carried out on OV-275 at 60˚C for 30 minutes and on P25DMA at 90˚C for 24 hours.

Then, as shown in Fig. 4.3.2, the sensor was assembled and connected to the gas characterization system [48], and the S_{11} of the sensor was monitored with an Agilent 8719ES VNA. The analyte gases of acetone (ε_r = 22.3) and benzene (ε_r = 2.5) were delivered into the sensor cavity at a constant flow rate of 200 sccm at four discrete concentration levels: 5000 ppm, 2500 ppm, 1250 ppm, and 625 ppm. This was accomplished by delivering a mixture of nitrogen and analyte gases using multiple mass flow controllers (MFCs). The unfunctionalized sensor (free of polymer coating) was tested first for baseline cavity sensor response before the two functionlized sensors were evaluated. The S_{11} curves of the sensor responses were recorded accordingly to construct their sensitivity curves.

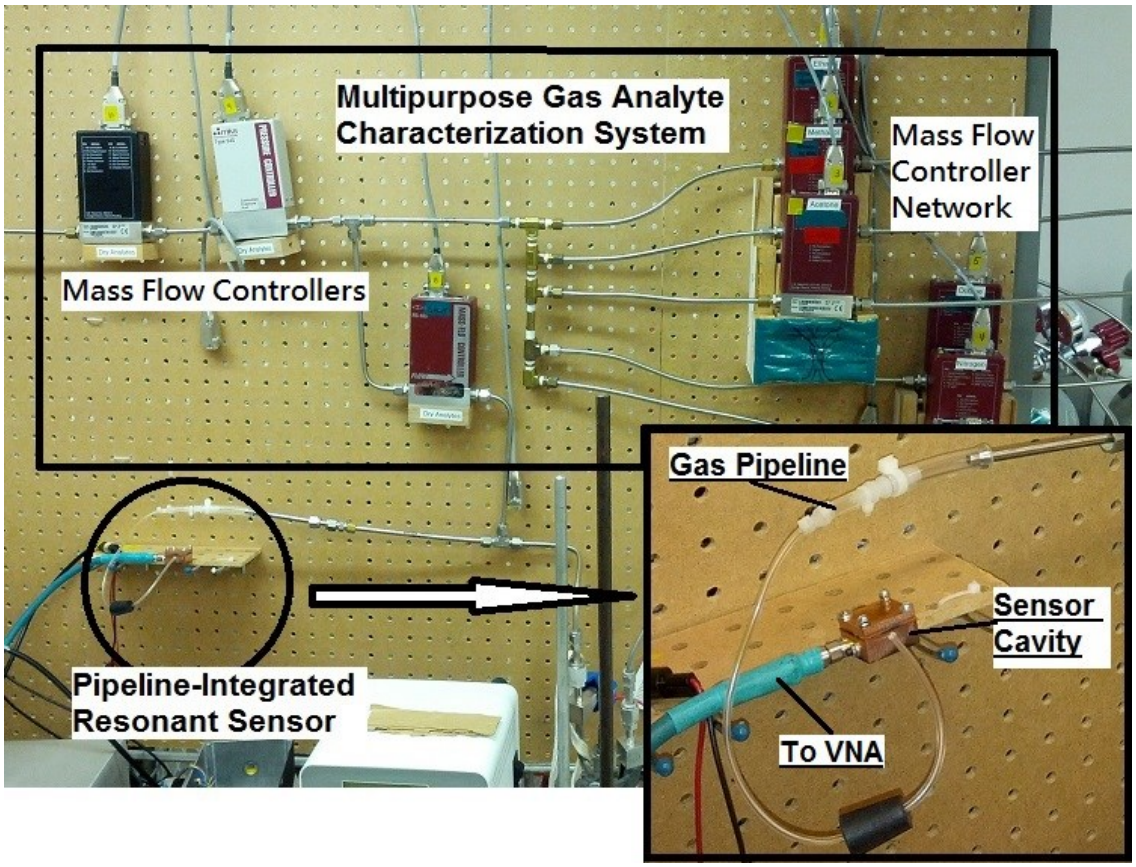

Fig. 4.3.2. Combline resonant sensor integrated with the gas-line network of the multipurpose gas characterization system.

4.4 INITIAL CHARACTERIZATION PROCEDURES

Fig. 4 shows the sample S_{11} curves illustrating the Δf_0 of the OV-275 sensor under the exposures of gaseous acetone, and by monitoring ΔS_{11} at $S_{11,\,0ppm}$ = -20dB ($f \sim$ 4.1052 GHz), the sensor has seen a %ΔS11 of approximately 17%, under a $\%\Delta f_0$ of ~0.02%.

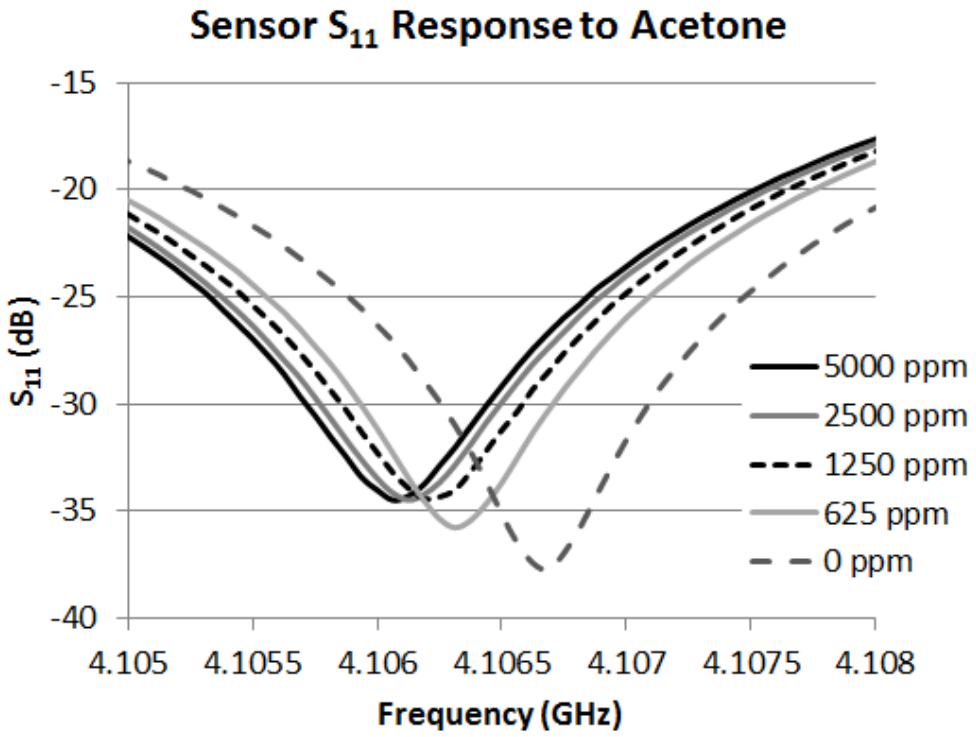

Fig. 4.4.1. S_{11} response curves of OV-275 sensor under discrete gaseous acetone exposures.

The resultant average response amplification factor was therefore calculated to be more than 1000, which is one order of magnitude higher than that of the planar CPW resonant sensor reported in [55], indicating a significantly higher sensitivity of the cavity sensor. If the sensor is excited with an arbitrary monotone RF signal at ~4.1052 GHz, the ΔS_{11} would be significant enough to achieve an unsaturated sensitivity level of 2.883 mdB/ppm. All results presented in the next section are obtained with the identical methodology.

4.5 RESULTS AND DISCUSSIONS

Fig. 4.5.1 and Fig. 4.5.2 are constructed for $\%\Delta S_{11}$ and $\%\Delta f_0$ using similar data sets for both acetone and benzene for each sensing material, along with the responses of the unfunctionalized sensor as a baseline comparison. It is important to note that OV-275 is visibly approaching its analyte saturation level under acetone exposure beyond 2500 ppm. This limitation can be overcome by increasing the thickness of the deposited polymeric sensing material to allow more analyte sorption capacity, but this may reduce the sensitivity of the sensor.

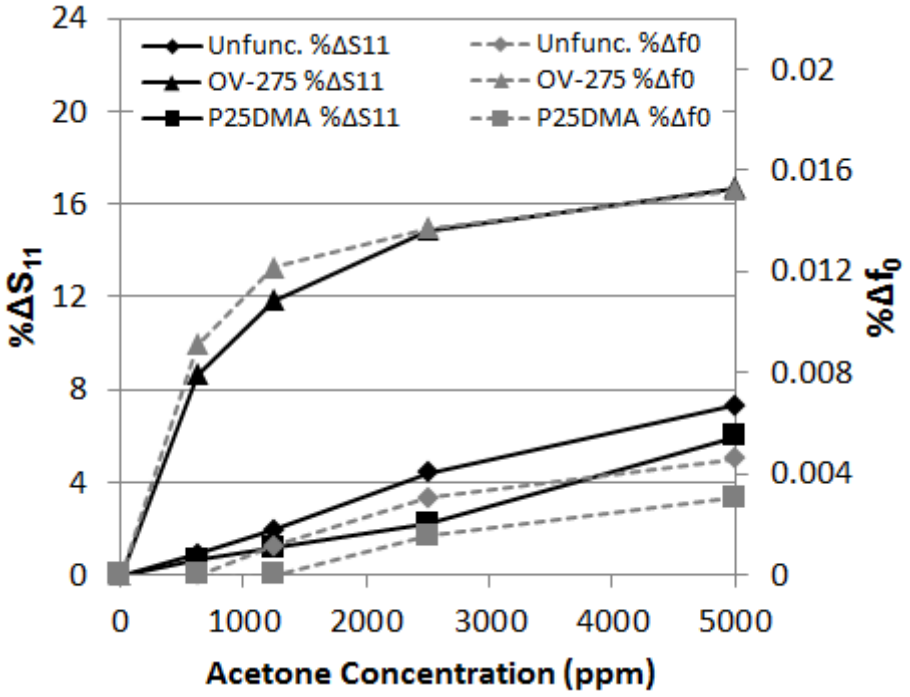

Fig. 4.5.1. Normalized S_{11} sensitivity curves of OV-275 sensor against acetone and benzene exposures (sampled at S_{11} = -20dB).

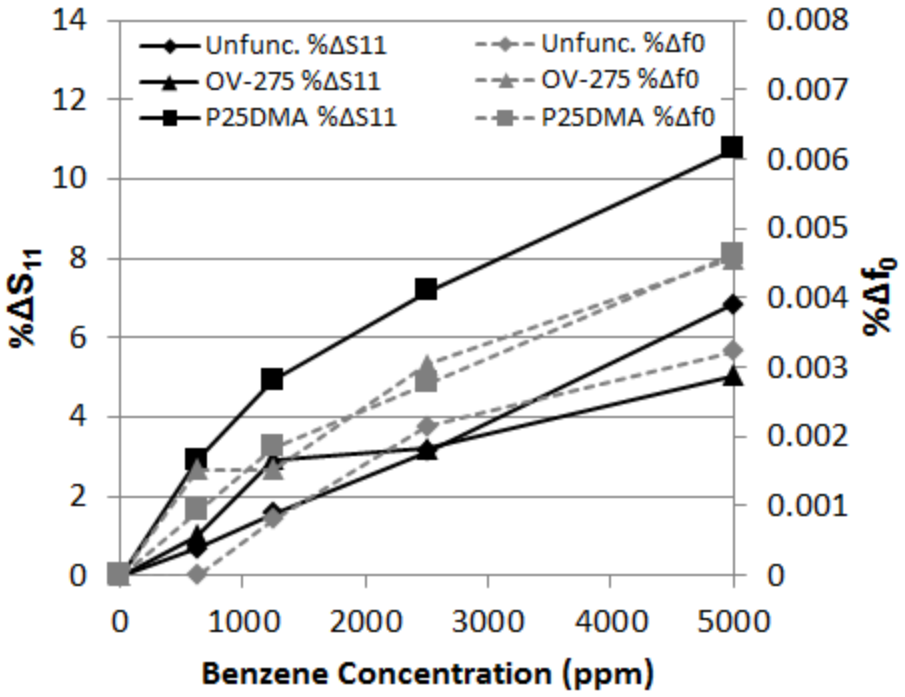

Fig. 4.5.2. Normalized S_{11} sensitivity curves of P25DMA sensor under discrete gaseous acetone exposures (sampled at S_{11} = -20dB, acetone $\%\Delta f_0$ below 1000 ppm is too small to be calculated due to equipment limitations).

With the estimated sensitivity curves constructed, the slopes of the unsaturated linear portion of the response curves are calculated as the sensitivities of the respective sensors, and summarized with the average amplification factors in Table I.

Table 4.5.1. Summary of S_{11} Sensitivity and Average Amplification Factor

Sensor	S_{11} Sensitivity (mdB/ppm)		Amplification Factor ($\%\Delta S_{11}/\%\ \Delta f_0$)	
	Acetone	Benzene	Acetone	Benzene
Unfunctionalized	0.310	0.247	1576.5	1829.6
OV-275	2.332	0.348	1051.5	1157.6
P25DMA	0.199	0.764	1700.2	2525.2

4.6 SUMMARY

A polymeric sensing material-based RF combline resonant sensor has been demonstrated in this chapter with the sensor designed to be integrated with a chemical gas pipeline system for analyte-specific, high-sensitivity detection of VOCs. The sensors show respective S_{11} sensitivities against acetone and benzene of 2.332 mdB/ppm and 0.348 mdB/ppm for the OV-275 sensor, and 0.199 mdB/ppm and 0.764 mdB/ppm for P25DMA. A sensitivity amplification factor exceeding 1000 resulted from the high Q of the cavity resonant sensor. This design can also be further expanded into multi-resonator structures with different polymer coatings on individual combline posts to form a RF cavity-based gaseous compound sensor array.

CHAPTER 5

FLEXIBLE RF SENSOR ARRAY WITH CMRE TECHNIQUE

5.1 INTRODUCTION

This chapter presents a novel single-port, multi-pole resonant sensor array fabricated on novel Frame-Flex flexible substrate for wearable epidermal ethanol sensor system. Individual sensors carrying different functional polymers are brought together to share the same electrical input and output, and their resonance behavior along with inter-resonator coupling are captured through the a single reflected array response curve (S_{11}). A coupling-matrix readout extraction (CMRE) technique is proposed to determine, from the S_{11} response, the changes in diagonal-coupling coefficient, ΔM_{ii}, which are used to identify different chemical analytes as the coupling signature. Two sensor arrays implementing different functional polymer sets (one with siloxane-based polymers and the other with crystalline-based polymers) are fabricated and tested under two selected mechanical loading conditions. The CMRE technique is then employed to obtain the coupling signatures of ethanol, methanol, acetone, and benzene on the arrays. It is successfully shown that the array response analyzed through the CMRE technique can clearly distinguish the

presence of ethanol from other chemical interferents. For complicated mixtures of ethanol and other unwanted analytes, the distinctive coupling signatures obtained by CMRE can be used as a reliable data source feed to post-readout multi-variant analysis for pattern recognition.

5.2 RESONANT SENSOR ARRAY DESIGN

Conventional sensor arrays used as electronics noses for chemical signature identification all have dedicated electrical connections before or after the analog-digital converter (ADC) to individual sensors to mutually decouple the sensor readings from each other. This configuration poses the fundamental size limit to the sensor array. In addition, when operating sensor at resonance for amplified response and sensitivity, the required electrical separation would be higher, resulting in larger design footprint with more complicated readout circuit.

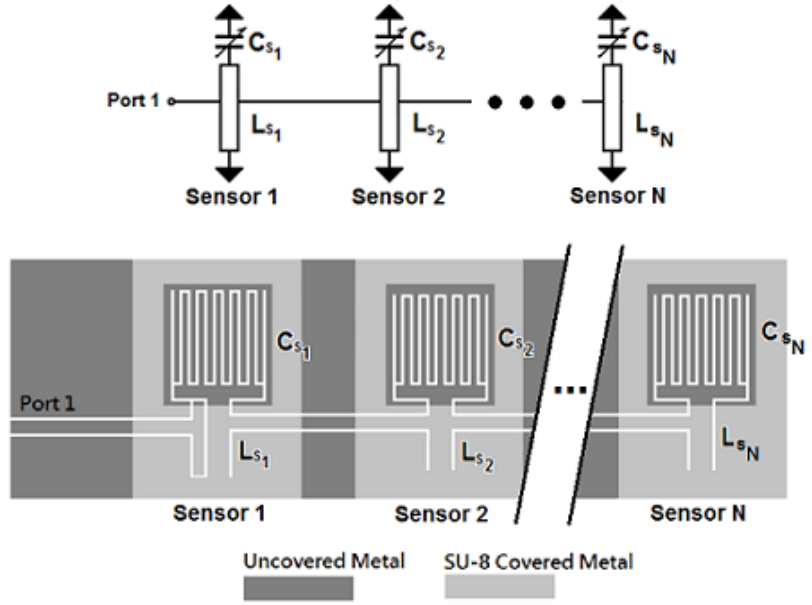

Fig. 5.2.1: Single-port, multi-pole resonant sensor circuit model (above) and CPW realization (below).

In order to overcome this size limitation for wearable sensor array design, the combline chemi-capacitive resonant sensor [20] is used as the building block for the single-port, multi-pole resonant sensor array shown in Fig. 5.2.1. The sensor consists of the thick-film interdigital chemi-capacitive sensor loaded with different functional polymers that are responsive to different chemical analytes [20]. It is connected in shunt with a fixed inductor, L_S, to form a resonant sensor at the selected frequency, f_S. These resonators may be designed to resonate either at the same frequency or at

distinctively different frequencies for different application needs. The change in capacitance of the chemi-capacitive sensor (ΔC_S) is reflected in the shift in the sensor resonant frequency (Δf_S), thereby providing an effective readout pathway for each sensor.

In such configuration, all the sensors are sharing one single electrical connection, and their collective response curve, known as the return loss (S_{11}) of the resonant structure, contain the responses of individual sensors. In this way, the sensor array can be operated at resonance for improved sensitivity, while keeping the sensor design footprint and the readout circuit as small as possible.

In this configuration, however, all of the resonant sensors inadvertently have mutual coupling with each other along the shared electrical connection. As a result, an observed Δf_S on one resonator may not be solely due to ΔC_S but to the coupling between resonators (ΔM_{ij}), rendering the simple mathematical relationship of $f_S = 1 / 2\pi(L_S C_S)^{1/2}$ ineffective in extracting ΔC_S from Δf_S. Such a drawback requires a more sophisticated readout method to decouple the sensor readings from the inter-resonator coupling.

5.3 COUPLING MATRIX READOUT EXTRACTION (CMRE) TECHNIQUES

The general form of the two-port, *n*-resonator coupling matrix model defined in Fig. 5.3.1 and Eq. 5.3.1 is widely used to characterize and isolate tuning parameters out of two-port, multi-pole resonant structures, and thus is common in filter optimization. The *n*-pole coupling matrix model contains the main coupling matrix $\boldsymbol{M}$ with the dimension of n x n, in which the diagonal-coupling coefficients (M_{ii}) arisen from the capacitance-inductance resonance, and the inter-resonator coupling (M_{ij}) arisen from the effect of energy sharing among the resonators are defined. The termination impedance matrix, $\boldsymbol{R}$, contains all zeroes except the input impedance in R_{11} and the output impedance in R_{nn}. Finally, λ is the lowpass to bandpass transformation variable, in which the center frequency of the resonant structure is denoted as f_0, the bandwidth of the structure as BW, and the independent frequency variable as f. With these matrices and formulas, the close-form expression of the insertion loss and return loss as functions of f (i.e., $S_{11}(f)$ and $S_{21}(f)$) can be derived [29].

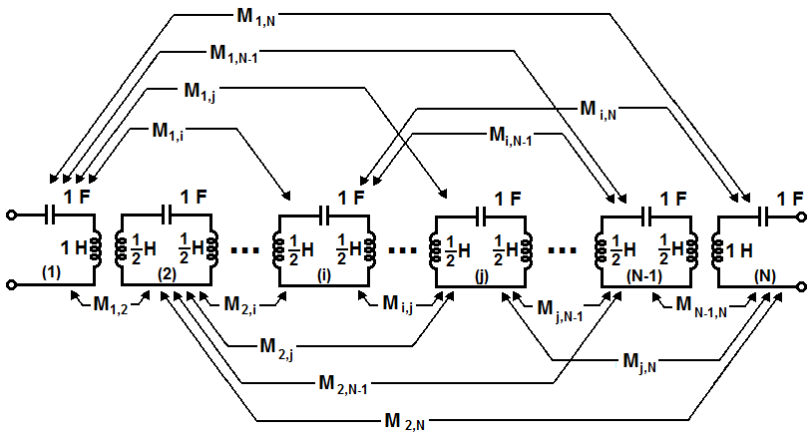

Fig. 5.3.1. General coupling matrix model for 2-port, multi-pole system [21].

$$\boldsymbol{M} = \begin{bmatrix} M_{11} & \cdots & M_{1n} \\ \vdots & \ddots & \vdots \\ M_{n1} & \cdots & M_{nn} \end{bmatrix}$$

$$\boldsymbol{R} = \begin{bmatrix} R_S & \cdots & 0 \\ \vdots & \ddots & \vdots \\ 0 & \cdots & R_L \end{bmatrix}$$

$$\lambda = \frac{f_0}{BW}\left(\frac{f}{f_0} - \frac{f_0}{f}\right) \tag{5.3.1}$$

$$S_{11} = 1 + 2jR_S[\lambda \boldsymbol{I} - j\boldsymbol{R} + \boldsymbol{M}]^{-1}_{11}$$

$$S_{21} = -2j\sqrt{R_S R_L}[\lambda \boldsymbol{I} - j\boldsymbol{R} + \boldsymbol{M}]^{-1}_{n1}$$

By applying an open-circuit load at port two of the general coupling matrix model, a modified coupling matrix model for single-port, multi-resonator structure presented in Fig. 1 can be obtained, as shown in Fig. 5.3.2, and the close-form expression of S_{11} at port one can be expressed as a function of R_S, R_L, M_{ii} and M_{ij}. A sample S_{11} expression of a one-port, three-pole resonant array is shown in Eq. 5.3.2. As far as the CPW implementation of the sensor array in Fig. 5.2.1 is concerned, the capacitive input coupling and the direct transmission line connection coupling between resonators can be represented by their respective numerical coupling coefficients, M_{ij}, as both physical implementations serve to control the amount of RF energy shared among resonators.

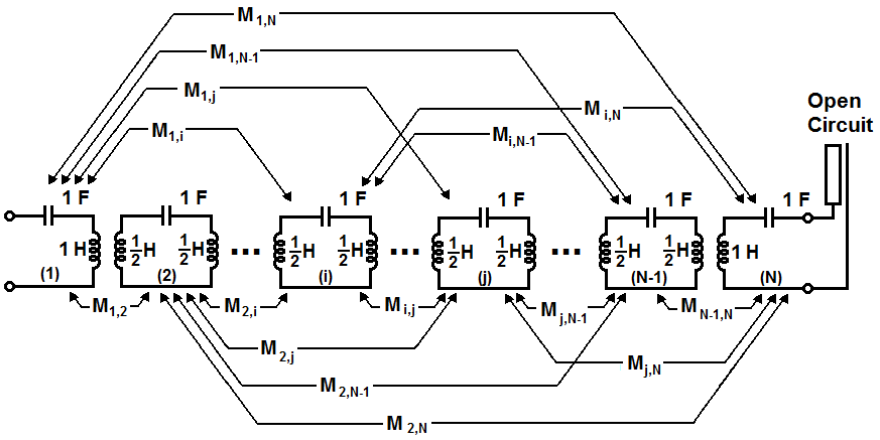

Fig. 5.3.2. Modified coupling matrix model for 1-port, multi-pole sensor array.

$$\Gamma_{OpenLoad} = S_{11} + \frac{{S_{21}}^2}{1-S_{22}}$$

$$= 1 + \frac{2jR_S}{\det(\lambda \boldsymbol{I} - j\boldsymbol{R} + \boldsymbol{M})}\left\{\left[(\lambda + M_{22})(\lambda - jR_L + M_{33}) - {M_{23}}^2\right] - \frac{{M_{12}}^2{M_{23}}^2}{\left[(\lambda+M_{22})(\lambda-jR_S+M_{11})-{M_{12}}^2\right]}\right\} \quad (5.3.2)$$

When individual sensors are designed to resonate at different frequencies, the bandwidth of the array is defined as the frequency range between the lowest and the highest sensor resonant frequencies (f_1 and f_n) and the center frequency of the array (f_0) as the $f_0 = (f_1 f_n)^{1/2}$. In this case, asynchronous tuned coupling matrix model must be considered, and all M_{ii} would hold non-zero values, through which their corresponding resonant frequencies (f_{Si}) can be derived from Eq. 5.3.3 [29].

$$M_{ii} = \frac{f_0}{BW}\left(\frac{f_0}{f_{Si}} - \frac{f_{Si}}{f_0}\right) \quad (5.3.3)$$

By taking the differentiation of M_{ii} with respect to C_{Si}, as shown in Eq. 5.3.4, it is obvious that ΔM_{ii} / ΔC_{Si} is a function of C_{Si} and L_{Si}, implying that to obtain a numerical value of ΔC_{Si} from ΔM_{ii}, either C_{Si} or L_{Si} of the array have to be characterized beforehand in order to obtain the *Capacitance Signature* of the array [56]. Furthermore, Eq. 5.3.4 mathematically asserts a basis transformation relationship between ΔM_{ii} and ΔC_{Si}, implying that ΔM_{ii} and ΔC_{Si} are merely two number sets representing the same phenomenon. As a result, in the case scenarios where isolated characterizations of C_{Si} and L_{Si} are difficult to perform, Eq. 5.3.4 guarantees that ΔM_{ii} alone can also be used as the *Coupling*

Signature to identify the analyte, with no loss of accuracy in the absence of the absolute values of C_{Si} and L_{Si}.

$$\frac{\Delta M_{ii}}{\Delta C_{Si}} = \left(\frac{\Delta M_{ii}}{\Delta f_{Si}}\right)\left(\frac{\Delta f_{Si}}{\Delta C_{Si}}\right) = -\frac{{f_0}^2}{BW}\left[\pi\sqrt{\frac{L_{Si}}{C_{Si}}} + \frac{1}{4\pi {f_0}^2\sqrt{L_{Si}{C_{Si}}^3}}\right] \tag{5.3.4}$$

In addition to the constant L_S assumption, M_{ij}, R_S and R_L should also be assumed constant under analyte exposure. This is because the input transmission line, the coupling transmission lines, and the open-circuit termination of the sensor array illustrated in Fig. 5.2.1 are not covered in functional polymer and thus are not responsive to analyte exposure. As a result, the parameters subject to change against analyte exposures can be safely assumed to be only ΔM_{ii}, or the *Coupling Signature*.

5.4 FRAME-FLEX FLEXIBLE SENSOR ARRAY FABRICATION

Expanded from MEMS rigid-flex flexible substrate processes [31], the novel "*Frame-Flex*" process is designed to allow MEMS or non-MEMS devices to submerge into the solid islands, providing higher design flexibility and monolithic device packaging. As illustrated in Fig. 5.4.1, by incorporating the Frame-Flex flexible substrate preparation process with the resonant sensors designed in the previous chapter, the sensor can be mechanically protected from physical deformation when the sensor strip is bent to conform to skin surface and to physical contact against the skin surface. This is done to prevent unwanted damage to the polymer-coated portion of the sensor. Moreover, the "frame" that surrounds the sensor area also acts as the polymer pocket, thereby guaranteeing the polymeric sensing materials are deposited exactly on the interdigital chemi-capacitor area without overflow.

The sample fabrication process of the RF resonant sensor array on the Frame-Flex substrate is illustrated in Fig. 5.4.2.

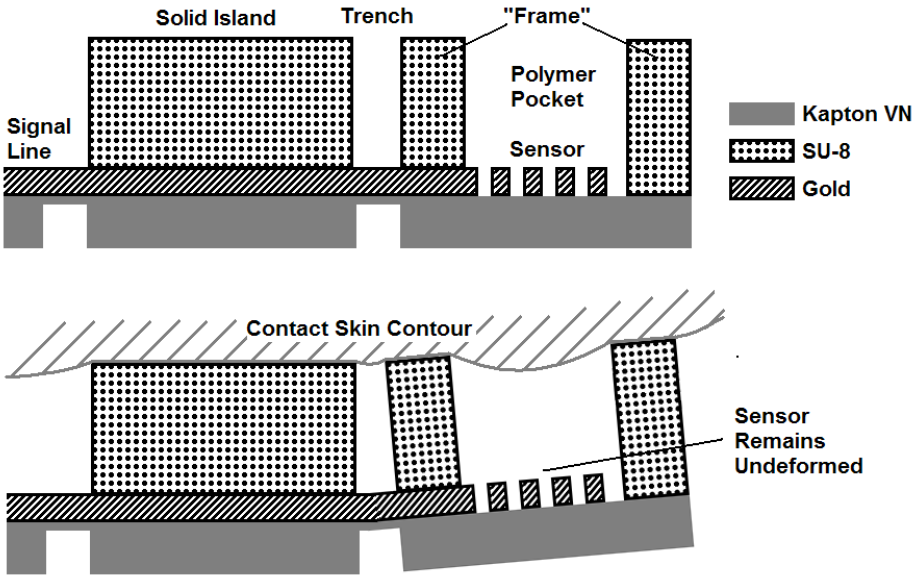

Fig. 5.4.1: Resonant sensor on Kapton/SU-8 Frame-Flex substrate for deformation and physical contact protection, as well as polymer deposition convenience.

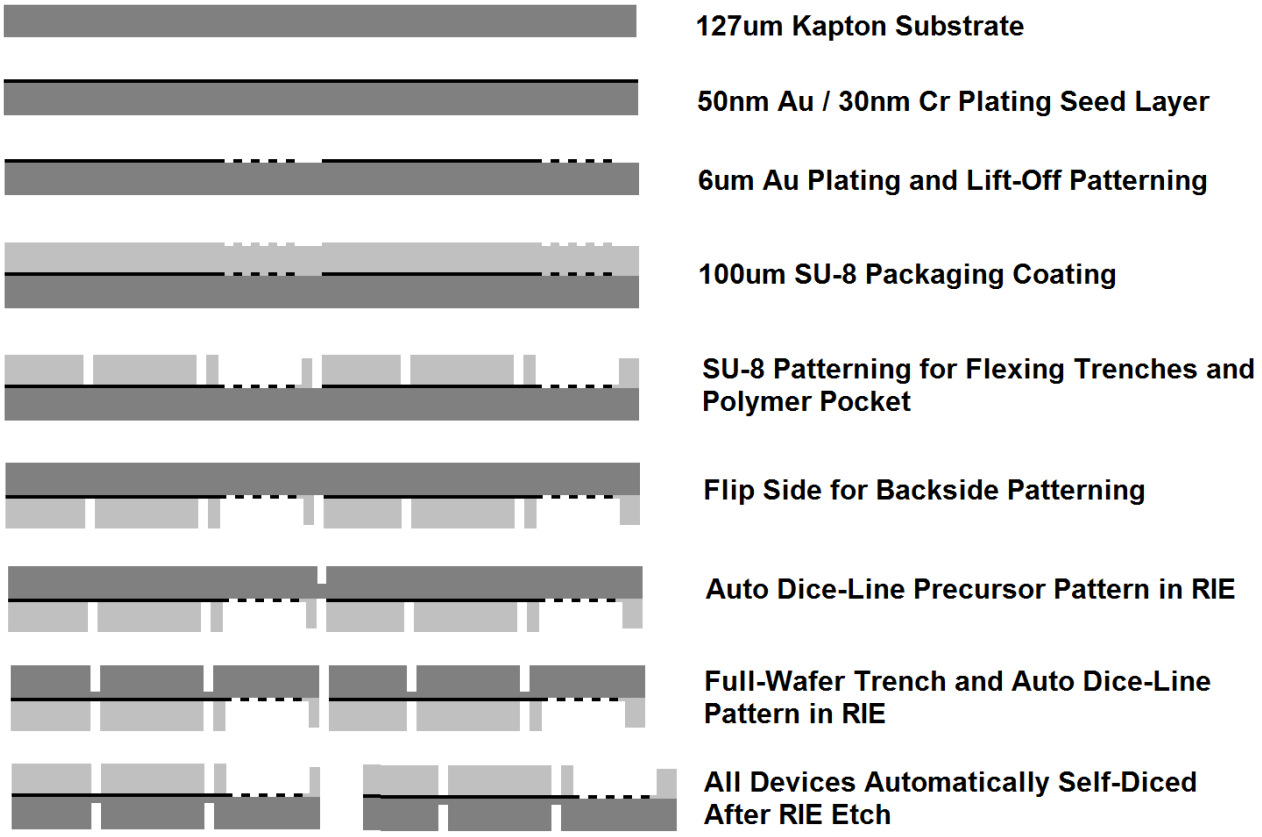

Fig. 5.4.2: Frame-Flex flexible substrate preparation process.

The process illustrated in Fig. 5.4.2 starts with a 500mil Dupont Kapton VN substrate with a 5µm plated gold pattern on the front side as the RF resonant sensor structure. Then, a layer of 100µm SU-8 is spin-coated and patterned to form the plastic *Frame* that provides mechanical protection on the resonant sensor, while leaving an opening in the chemi-capacitor area to allow for simple and controlled functional polymer deposition. The thickness of the SU-8 frame can be further increased to achieve more optimal separation distance between the sensor and the target skin surface in order to prevent physical damage to the sensor. Finally, the substrate is patterned from the back side with O_2 plasma in a reactive ion etcher to complete the Frame-Flex substrate preparation process. The etching process is carried out with 30 sccm O_2 flow and DC-biased RIE at 300W, the chamber pressure is kept at 50 Pa, and inductively-coupled plasma power is kept at a minimal level of 50W to ensure the etching process is fully anisotropic at the substrate surface.

Fig. 5.4.3 and Fig. 5.4.4 show, respectively, the fabricated single-resonant sensor and the 3-sensor array on a Frame-Flex Kapton/SU-8 substrate.

Fig. 5.4.3: Single RF resonant sensor on Kapton/SU-8 frame-flex substrate.

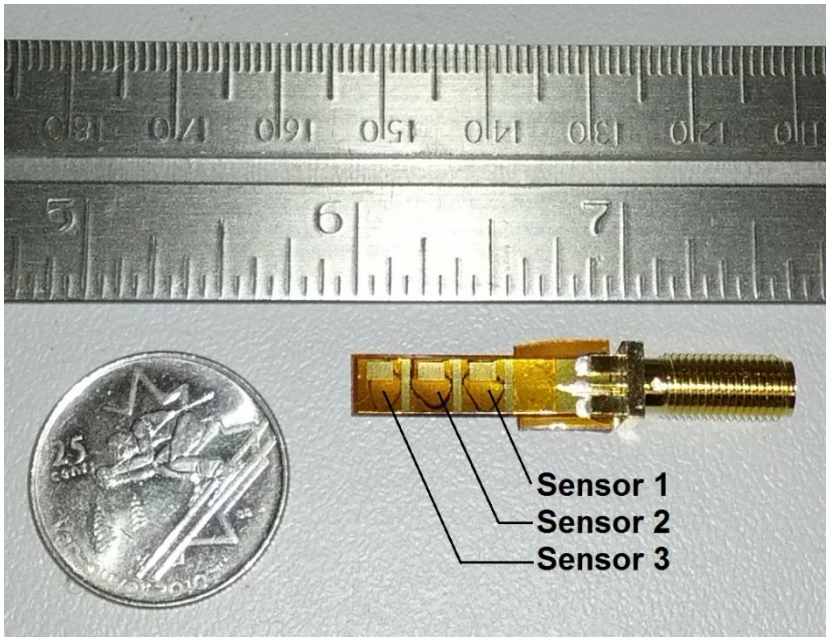

Fig. 5.4.4: 3-sensor RF resonant sensor array on Kapton/SU-8 frame-flex substrate.

5.5 EXPERIMENTAL SET-UP

The same testing system introduced in the previous chapter was used for the characterization of the sensor array. All four sample gases are individually tested with the same discrete concentrations of 5000 ppm, 2500 ppm, 1250 ppm, 625 ppm, and 0 ppm (unless otherwise indicated). However, in order to further characterize the sensor performance under substrate-bending conditions, plastic benders were built as illustrated in Fig. 5.5.1 to help hold the flexible sensor array in bent condition in the test chamber shown in Fig. 5.5.2. All of the experimental results for the sensor array characterization are collected under both the flat and bent mechanical states.

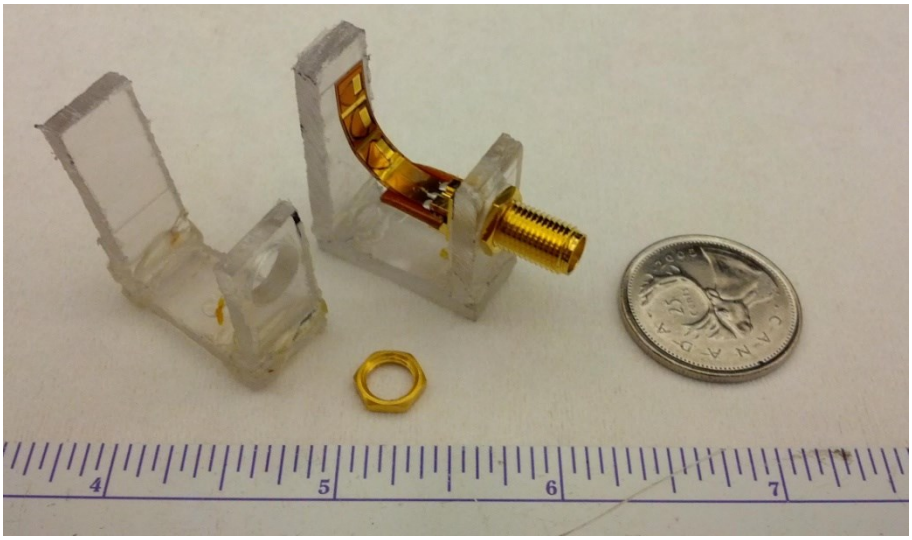

Fig. 5.5.1: Plastic bender for the frame-flex sensor array.

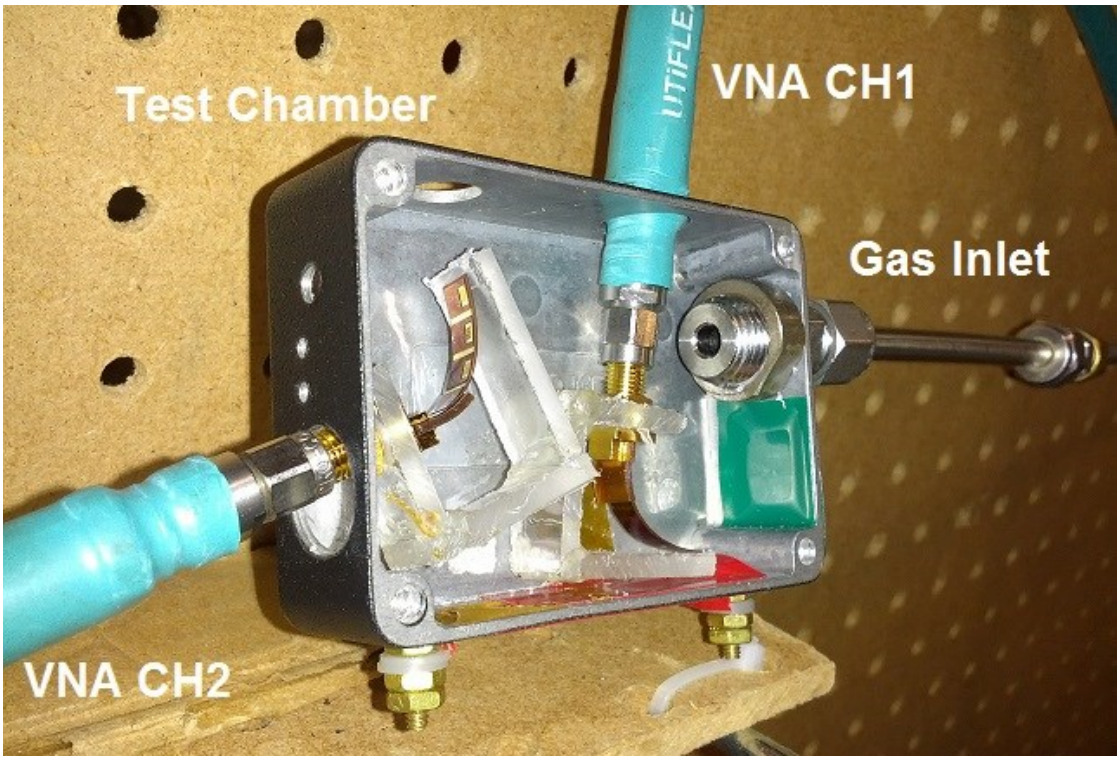

Fig. 5.5.2: Two arrays in mechanically bent state for performance characterization.

5.6 CMRE BASELINE CHARACTERIZATION PROCESS

5.6.1 ARRAY CHARACTERIZATION: SEQUENTIAL METHOD

We consider the example shown in Fig. 5.6.1. In order to utilize the CMRE technique to extract ΔM_{ii} and the subsequent ΔC_S from the sensor array, the array must first be characterized at its baseline, with no chemical exposure. This is done by purging the sensor array in the MFC-controlled chamber with constant nitrogen flow for at least an hour. Then, the baseline parameters of the coupling-matrix model, namely M_{ii}, M_{ij}, R_S, and R_L, are extracted through sequential coupling matrix mapping method [29].

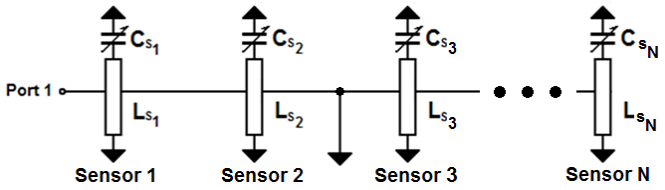

Fig. 5.6.1: Two-resonator partially terminated sensor array.

As illustrated in Fig. 5.6.1, the first step of the sequential method consists of terminating the coupling section between sensors 2 and 3, effectively making $M_{23} = 0$. Physically, such coupling termination can be done by shorting the coupling transmission line in Fig. 5.2.1 to the adjacent ground patches with wire bond. In this way, the resonant array will appear at port 1 as a two-resonator structure, thereby limiting the unknown baseline parameters to five: M_{11}, M_{22}, M_{12}, R_S and R_L. To find the approximated initial values of these parameters, a second-order 3dB-ripple Chebyshev filter prototype parameter [30], with an open load on port 2, is used as the initial model. The resultant values in $\boldsymbol{M}$ are then detuned to reflect the asynchronously-tuned nature of the array.

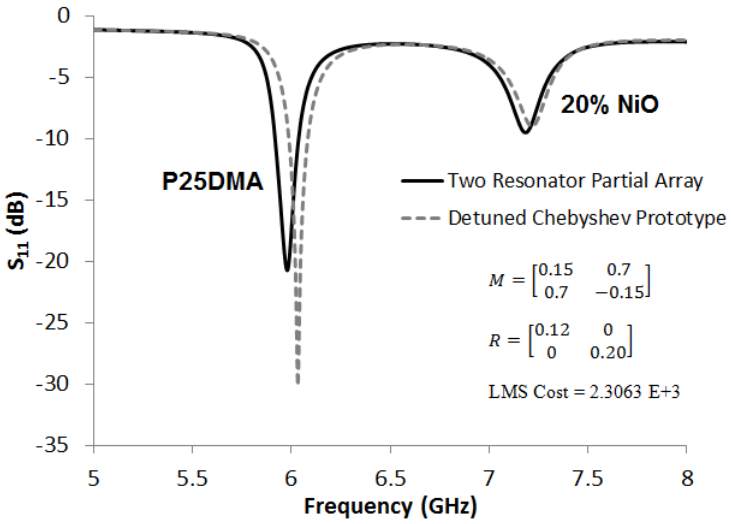

Fig. 5.6.2: Initial M and R selection derived from detuning a second-order 3-dB ripple Chebyshev filter prototype, and the respective S_{11} response from the two-resonator partial array recorded on VNA.

Fig. 5.6.2 shows the baseline ***M*** and ***R*** resulting from the detuned one-port, two-resonator Chebyshev prototype model with the VNA-recorded sensor response as the reference. The Least Mean Square (LMS) cost value indicates the amount of dissimilarity between the empirical response and the model through MatLab optimizer. The two-resonator partial array response in Fig. 5.6.2 is recorded from the crystalline sensor array under *Flat* conditions, with the second coupling segment grounded by wire bond. The names of the functional polymers are indicated next to their respective resonant peaks. The LMS optimizer in MatLab is then executed to fit the approximated model onto the empirical result. The resultant ***M***, ***R***, and LMS cost are shown in Fig. 5.6.3 to illustrate a successful baseline parameter capture.

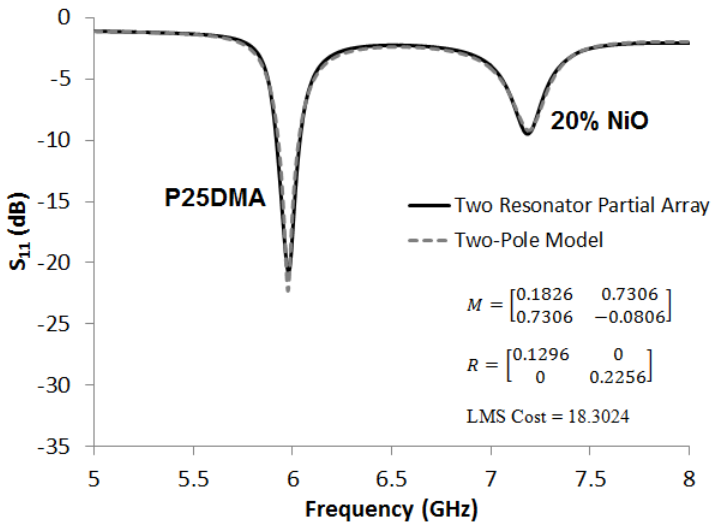

Fig. 5.6.3: LMS-Optimized M and R through MatLab, and the respective S_{11} response from the two-resonator partial array recorded on VNA.

The second step introduces the coupling termination in between sensors 3 and 4, making $M_{34} = 0$ and all the resonant sensors beyond sensor 3 inactive, as illustrated in Fig. 5.6.4. In this configuration, the following unknown baseline parameters are captured: M_{33}, M_{23}, and the new R_L. In addition, the four known parameters from step 1 (i.e., M_{11}, M_{22}, and M_{12}, and R_S) are slightly adjusted in the CMRE process as well. The resultant seven baseline parameters are illustrated in Fig. 4.6.5 along with the LMS cost and the empirical reference.

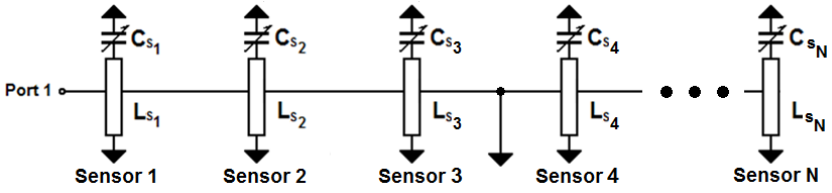

Fig. 5.6.4: Three-resonator partially terminated sensor array.

The subsequent steps are similar to step 2 and continue until all baseline parameters are captured and optimized. The result presented in Fig. 5.6.5 is the baseline response recorded when applied to the crystalline sensor array illustrated in Fig. 5.4.4, and will be used later in the example readout extraction for the crystalline array.

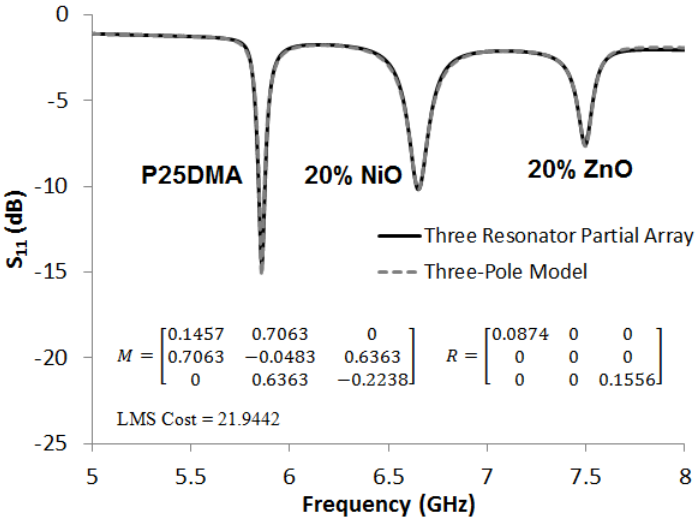

Fig. 5.6.5: LMS-Optimized M and R through MatLab, and the respective S_{11} response from the full three-sensor array recorded on VNA.

5.6.2 READOUT EXTRACTION EXAMPLES

With the CMRE-characterized sensor array parameters, the changes in sensor response after exposure to chemical analytes can be accurately quantized. Using the same crystalline sensor array prototype characterized in Fig. 5.6.5, the coupling signature parameters (M_{ii}) are introduced as the unknowns. Through the CMRE technique in Matlab optimizer, the changes in S_{11} responses of the array from different analyte exposures can be numerically represented, and the resultant M_{ii} as the coupling signatures are used for distinguishing different analytes.

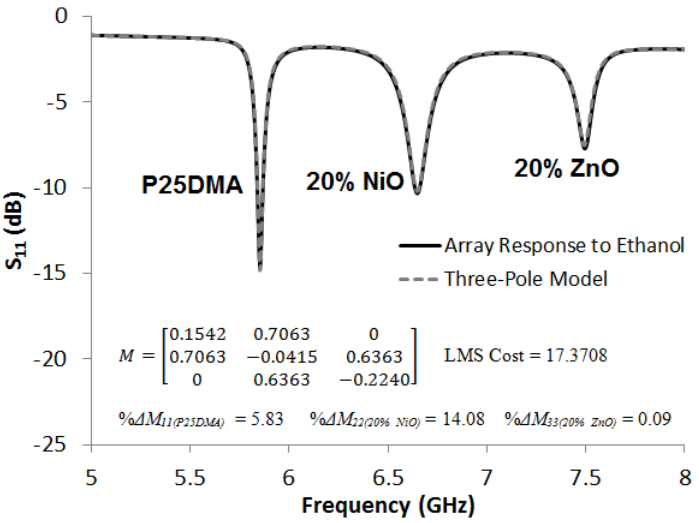

Fig. 5.6.6: Changes in coupling signature (M_{ii}) captured by CMRE technique for the crystalline sensor array exposed to 5000 ppm ethanol.

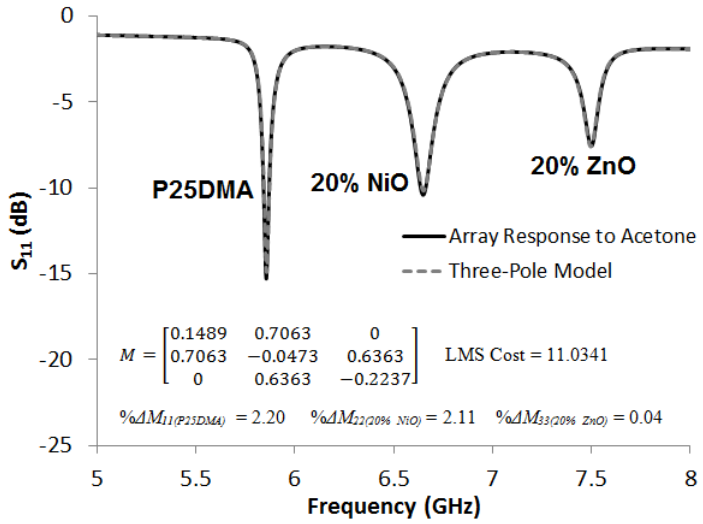

Fig. 5.6.7: Changes in coupling signature (M_{ii}) captured by CMRE technique for the crystalline sensor array exposed to 5000 ppm acetone.

Fig. 5.6.6 and Fig. 5.6.7 illustrate the S_{11} responses of the sensor array prototype exposed to 5000 ppm of ethanol and acetone, respectively. All of the coupling signatures along with their LMS costs are listed in the respective figures as well.

5.7 SILICONE POLYMERIC SENSOR ARRAY STEADY-STATE CHARACTERIZATION

Fig. 5.7.1 and Fig. 5.7.2 illustrate the baseline responses of the siloxane sensor array and the respective baseline ***M*** and ***R*** values of the coupling matrix model under *Flat* and *Bent* conditions, respectively. The names of the functional polymers are indicated beside their respective resonant peaks. These two baseline models are then used in the CMRE technique to help extract the coupling signatures of the gaseous analytes. The frequency-selective loss is assumed linear in the CMRE model.

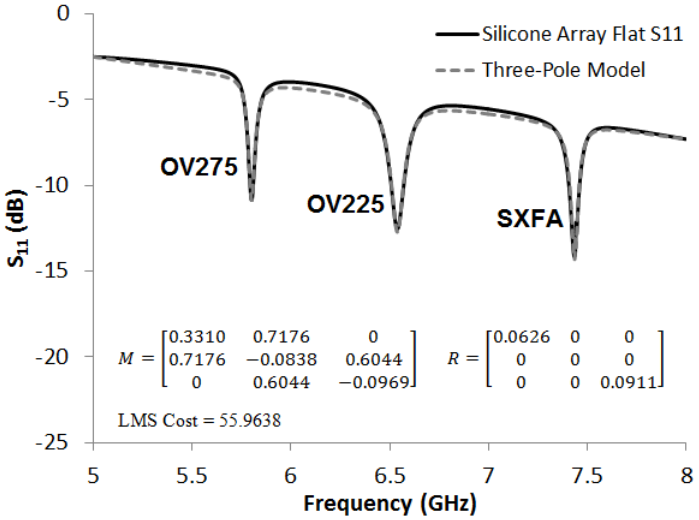

Fig. 5.7.1: Baseline CMRE model mapped on the baseline silicone sensor array response under no mechanical bending.

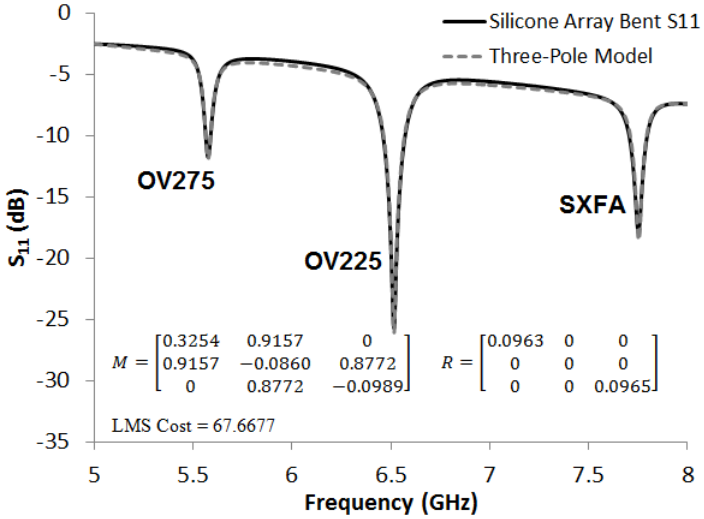

Fig. 5.7.2: Baseline CMRE model mapped on the baseline silicone sensor array response under applied mechanical bending.

Through the CMRE technique, the corresponding ΔM_{ii} values are extracted at the four discrete gaseous analyte concentrations. Fig. 5.7.3 to Fig. 5.7.6 illustrate the sensor array responses to ethanol and three other interferents (methanol, benzene and acetone) under both *Flat* and *Bent* conditions.

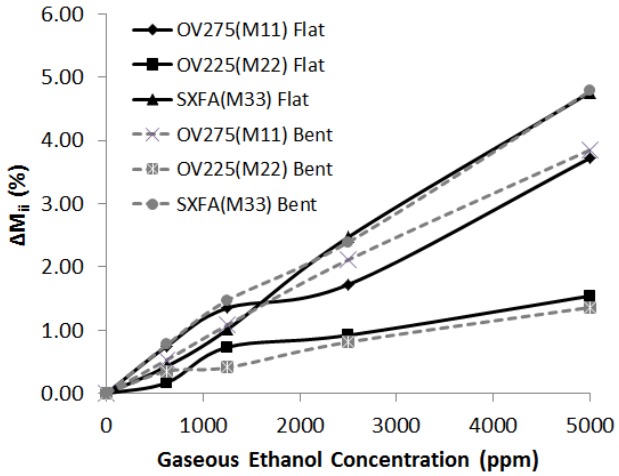

Fig. 5.7.3: Percentage change of M_{ii} under ethanol gaseous exposure. Flat and Bent responses are denoted in solid lines and dashed lines respectively.

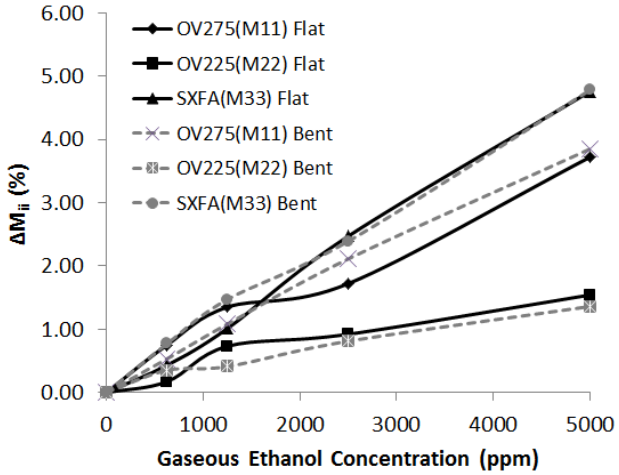

Fig. 5.7.4: Percentage change of M_{ii} under Methanol gaseous exposure. Flat and Bent responses are denoted in solid lines and dashed lines respectively.

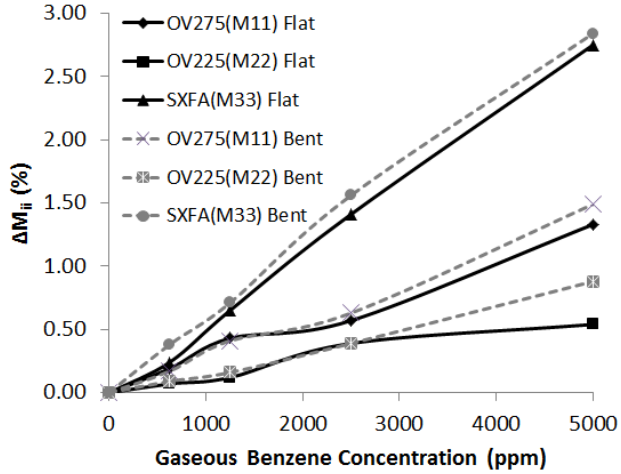

Fig. 5.7.5: Percentage change of M_{ii} under Benzene gaseous exposure. Flat and Bent responses are denoted in solid lines and dashed lines respectively.

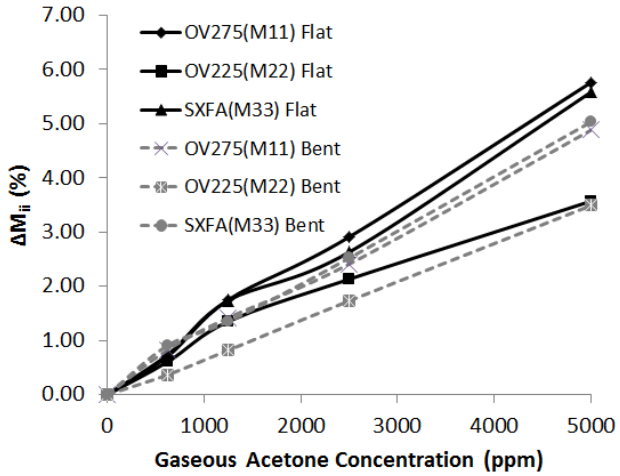

Fig. 5.7.6: Percentage change of M_{ii} under Acetone gaseous exposure. Flat and Bent responses are denoted in solid lines and dashed lines respectively.

It is very clear that the siloxane sensor array, through the CMRE technique, is capable of generating distinctive coupling signatures for identifying ethanol from other interferents. Benefiting from the Frame-Flex substrate, the sensor array shows only very small changes in ΔM_{ii} because the chemi-capacitor portion of the resonant sensor is mechanically protected inside the solid islands; these changes are well within the optimizer-reachable range from the *Flat* baseline model, and can be successfully captured. The changes in ΔM_{ij} and $\boldsymbol{R}$ are due to the mechanical deformation in the trench area, where the input and inter-resonator couplings are taking place. However, this performance deviation can still be accommodated by the CMRE technique, and all of the coupling signatures can still be successfully extracted. The analyte differentiation capability of the sensor array is minimally affected by the bending. Table 5.7.1 and Table 5.7.2 summarizes the sensitivity of each individual sensors in the array under both mechanical conditions. Fig. 5.7.7 and Fig. 5.7.8 summarize the coupling signatures against different analytes in terms of $\%M_{ii}$ / 1000 ppm under flat and bent conditions, respectively.

Table 5.7.1: Summary of Sensitivity of Siloxane Sensors (Flat Condition)

Analyte	Sensitivity ($\%M_{ii}$ / 1000ppm)		
	OV275	OV225	SXFA
Ethanol	0.928	0.383	0.859
Methanol	0.850	0.597	1.515
Benzene	0.286	0.118	0.505
Acetone	1.213	0.906	1.186

Table 5.7.2: Summary of Sensitivity of Siloxane Sensors (Bent Condition)

Analyte	Sensitivity ($\%M_{ii}$ / 1000ppm)		
	OV275	OV225	SXFA
Ethanol	0.832	0.371	1.080
Methanol	0.858	0.650	1.305
Benzene	0.288	0.151	0.592
Acetone	1.101	0.660	1.138

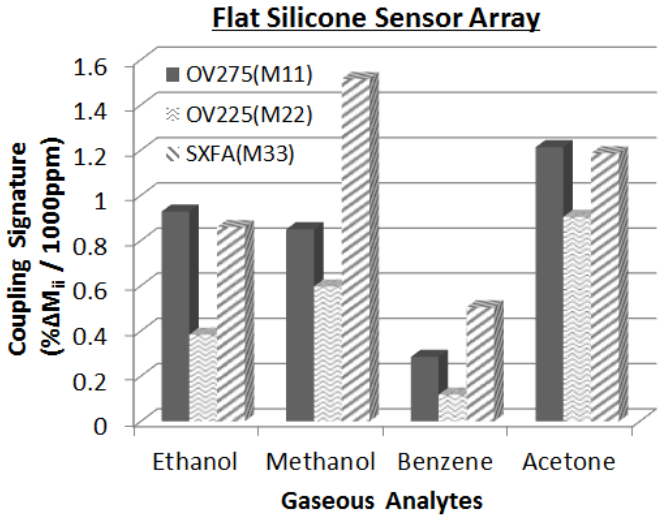

Fig. 5.7.7: Summary of coupling signatures of the four analytes on silicone sensor array under no mechanical bending.

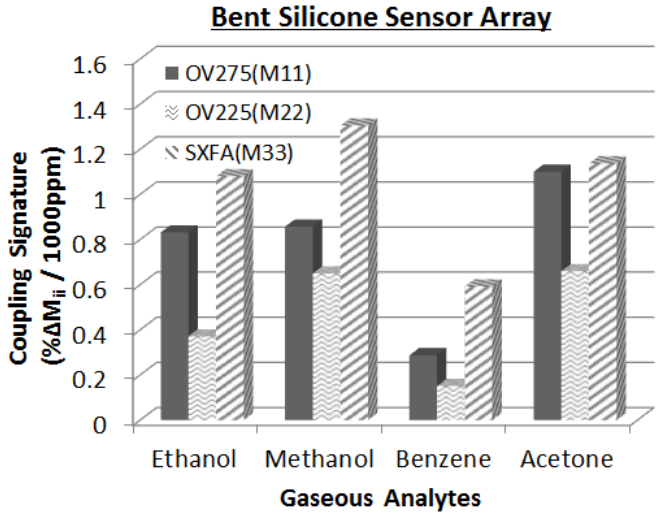

Fig. 5.7.8: Summary of coupling signatures of the four analytes on silicone sensor array under applied mechanical bending.

The siloxane-based functional polymers are known for their lossiness at higher frequencies, a characteristic that is evident on both baseline measurements in Fig. 5.7.1 and Fig. 5.7.2. Moreover, due to the non-linear frequency-selective loss, the CMRE models in these two figures showed slight discrepancies from the empirical results. The crystalline-based functional polymers, on the other hand, demonstrated a superior performance at higher frequencies, and thus are used in the second sensor array candidate in the next section.

5.8 Crystalline Polymeric Sensor Array Steady-State Characterization

Fig. 5.6.5 is again used as the baseline model for the flat condition, whereas Fig. 5.8.1 shows the baseline model under bent condition. The frequency-selective loss is assumed to be linear in the CMRE model.

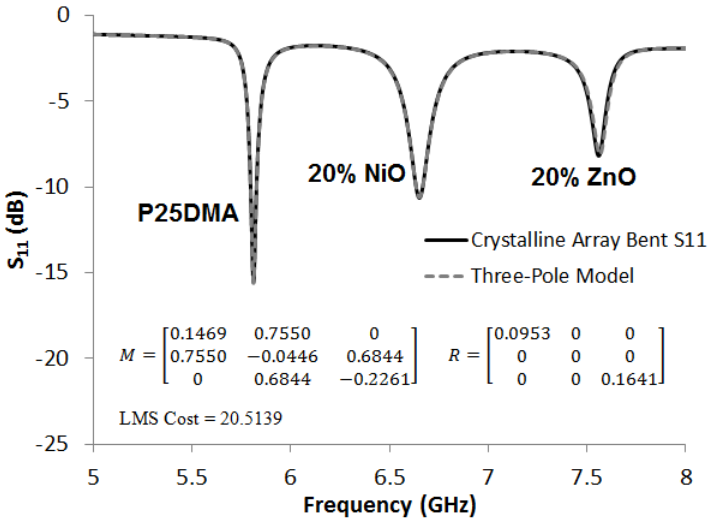

Fig. 5.8.1: Baseline CMRE model mapped on the baseline crystalline sensor array response under applied mechanical bending.

Similarly, both models use the CMRE process to extract the sensor array responses to different analytes at different concentrations, and their respective results are illustrated in Fig. 5.8.2 to Fig. 5.8.5.

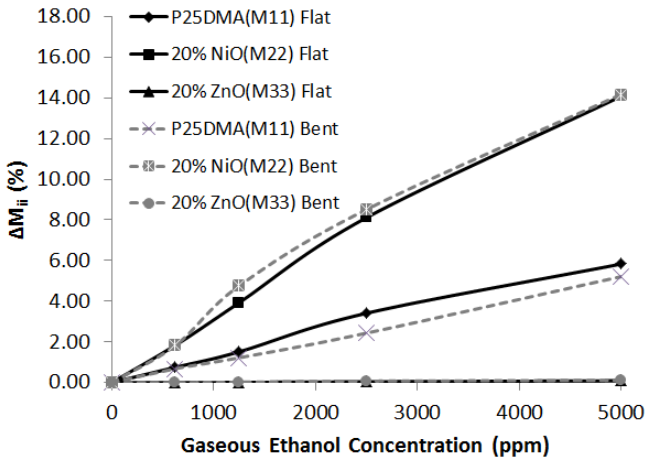

Fig. 5.8.2: Percentage change of M_{ii} under Ethanol gaseous exposure. Flat and Bent responses are denoted in solid lines and dashed lines respectively.

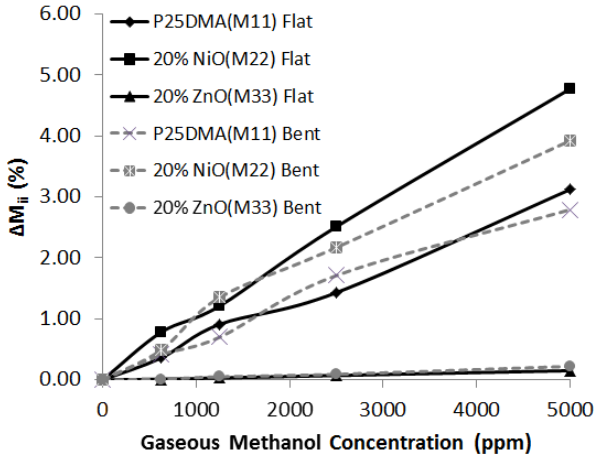

Fig. 5.8.3: Percentage change of M_{ii} under Methanol gaseous exposure. Flat and Bent responses are denoted in solid lines and dashed lines respectively.

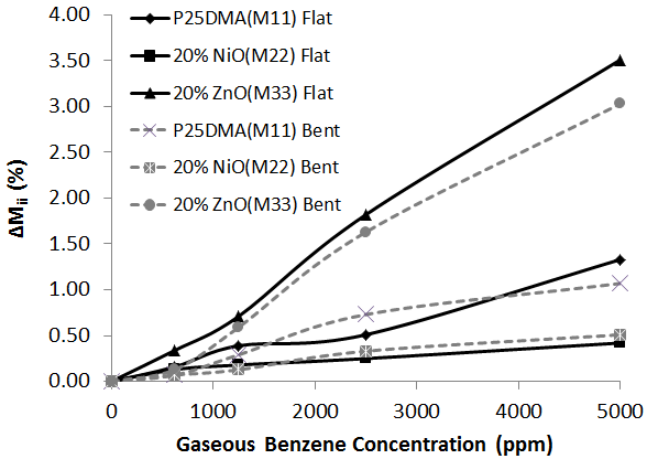

Fig. 5.8.4: Percentage change of M_{ii} under Benzene gaseous exposure. Flat and Bent responses are denoted in solid lines and dashed lines respectively.

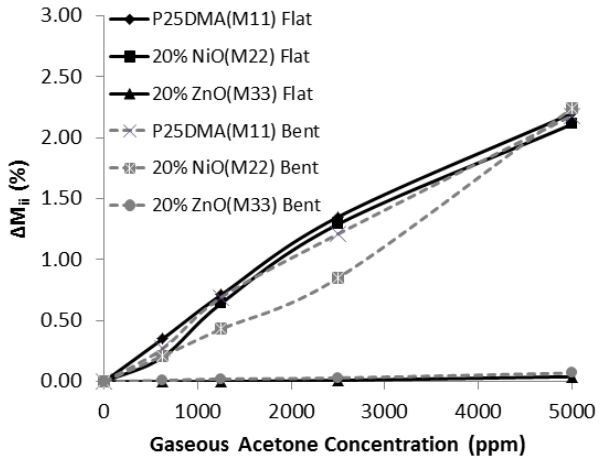

Fig. 5.8.5: Percentage change of M_{ii} under Acetone gaseous exposure. Flat and Bent responses are denoted in solid lines and dashed lines respectively.

Because of the low frequency-selective loss, our assumption of linear loss in the CMRE model has successfully brought us to a relatively accurate model mapping and thus a higher reliability for the extracted readouts. In addition to the improved frequency loss at high frequency, the CMRE process also indicates that the 20% NiO-doped P25DMA has an exceptional selectivity against ethanol. This fully verifies that the NiO-doped derivative of the P25DMA crystalline polymer is successfully customized as an ethanol-selective polymer. Once again, the performance reduction due to mechanical bending is minimal, as all the coupling signatures from both flat and bent conditions are highly similar. Table 5.8.1 and Table 5.8.2 summarize the sensitivities of individual sensors in the crystalline array.

Table 5.8.1: Summary of Sensitivity of Crystalline Sensors (Flat Condition)

Analyte	SENSITIVITY (%M_{ii} / 1000PPM)		
	P25DMA	20% NiO	20% ZnO
Ethanol	1.245	3.031	0.011
Methanol	0.625	1.044	0.025
Benzene	0.260	0.134	0.636
Acetone	0.527	0.443	0.003

Table 5.8.2: Summary of Sensitivity of Crystalline Sensors (Bent Condition)

Analyte	SENSITIVITY (%M_{ii} / 1000PPM)		
	P25DMA	20% NiO	20% ZnO
Ethanol	1.020	3.238	0.017
Methanol	0.615	0.879	0.034
Benzene	0.213	0.113	0.485
Acetone	0.476	0.367	0.015

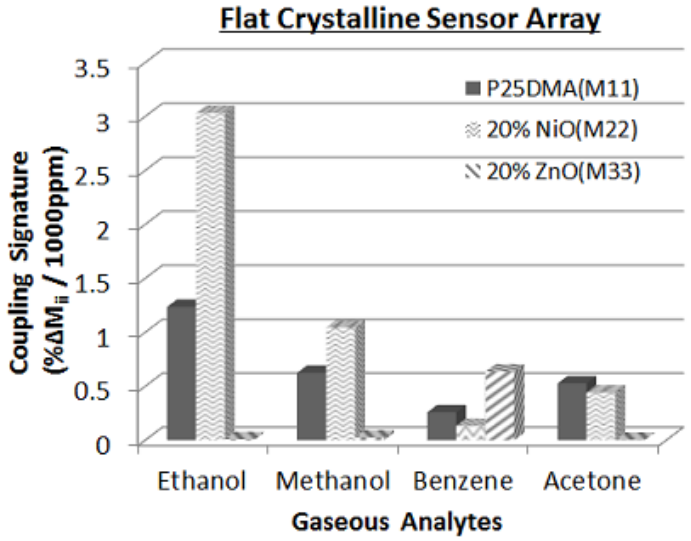

Fig. 5.8.6: Summary of coupling signatures of the four analytes on crystalline sensor array under no mechanical bending.

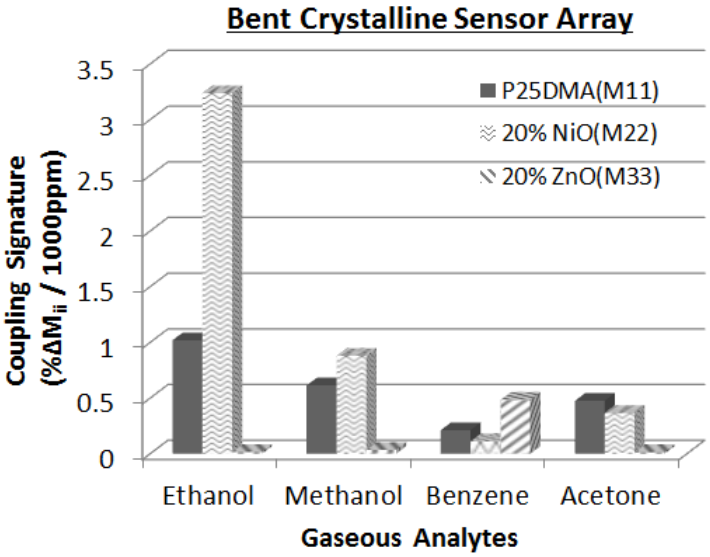

Fig. 5.8.7: Summary of coupling signatures of the four analytes on crystalline sensor array under applied mechanical bending.

Fig. 5.8.6 and Fig. 5.8.7 summarize all the coupling signatures in terms of $\%M_{ii}$ / 1000 ppm under flat and bent conditions, respectively. It is important to indicate that the sensitivity levels reported here, as well as those in [20], are in the equivalent range of $1 \sim 5$ % M_{ii} / 1000 ppm, which is lower than the existing DART and NIR technology where sub-ppm detections [38, 57] are possible. However, in light of the large reduction in cost and high physical conformity on human skin (i.e., optimal unobtrusiveness), performance reduction is a cost to be paid. Moreover, this reported performance can be further improved by investigating better polymer customization processes as well as developing more consistent polymer coating on the chemi-capacitor portion of the sensor array.

5.9 MULTI-ANALYTE PERFORMANCE CHARACTERIZATION

5.9.1 SINGLE-ANALYTE INTERFERENT MIXTURE

In more practical applications, the sensor array is expected to be exposed to mixtures of different gaseous analytes. The CMRE technique in such applications is capable of reliably extracting the distinct coupling signatures of each mixture from the sensor array response, and delivering them to the subsequent pattern recognition software to identify the presence of each gas analyte as well as their respective concentrations in the mixture. Fig. 5.9.1 and Fig. 5.9.2 show, respectively, the response signatures of the siloxane and crystalline sensor arrays to the selected two-analyte gas mixtures. The concentrations of all three interferents – methanol, acetone, and benzene – were held at 1250 ppm throughout the entire characterization run, and the coupling signatures were captured for the two discrete ethanol concentrations of 1250 ppm and 625 ppm. These concentrations are selected based on the limitations of the multi-purpose gas testing system. Both flat and bent physical conditions were recorded as well.

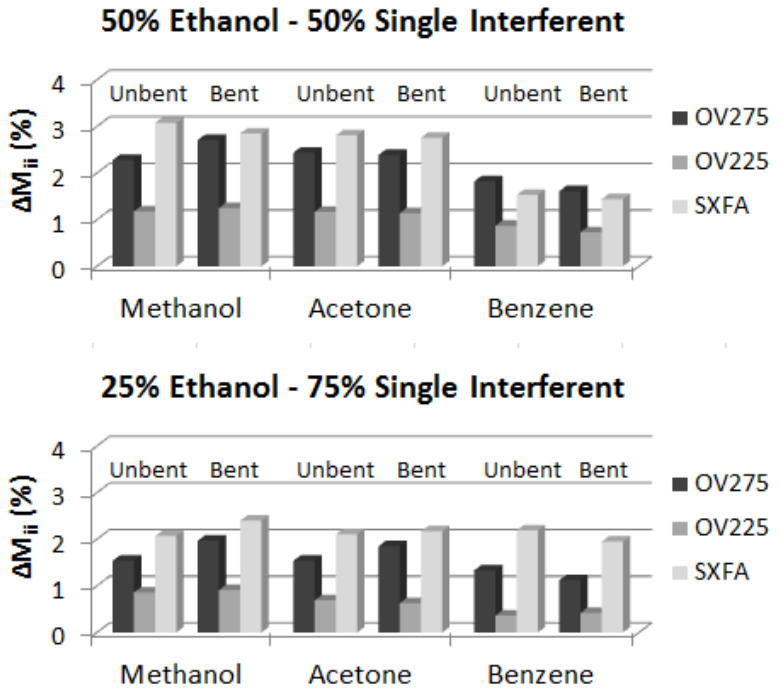

Fig. 5.9.1: Summary of coupling signatures of the gaseous mixtures of ethanol and selected single interferents on the siloxane sensor array with flat and bent physical conditions.

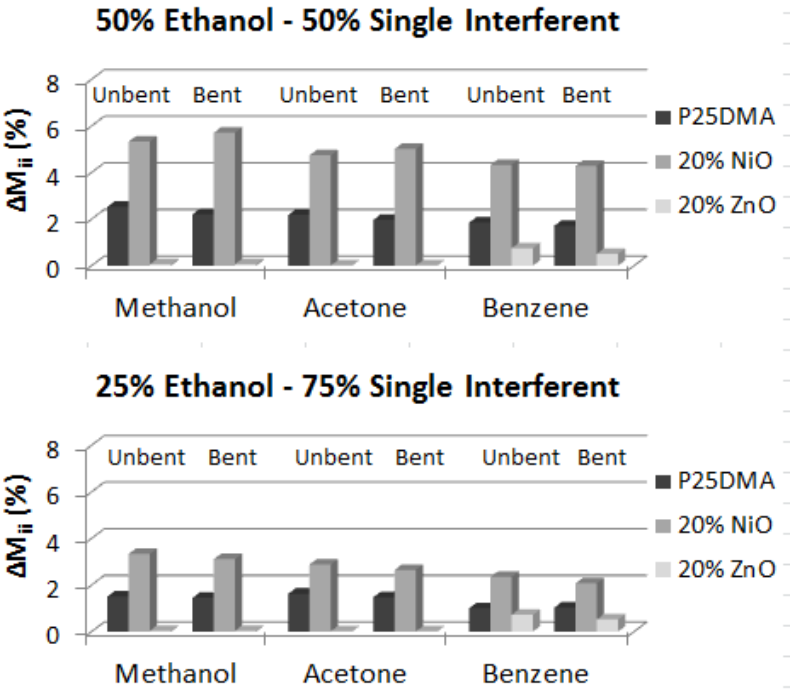

Fig. 5.9.2: Summary of coupling signatures of the gaseous mixtures of ethanol and selected single interferents on the crystalline sensor array with flat and bent physical conditions.

5.9.2 MULTI-ANALYTE INTERFERENT MIXTURE

Fig. 5.9.3 and Fig. 5.9.4 show the respective response signatures of the two versions of the sensor arrays to the selected three-analyte gas mixtures. The responses of both arrays to the mixture of ethanol and all three interferents are shown in Fig. 5.9.5. Once again, the concentrations of all the interferents were held at 1250 ppm, while ethanol concentrations were varied from 1250 ppm to 625 ppm. Both flat and bent physical conditions were recorded accordingly. All of these signatures are successfully extracted with the CMRE technique from the interference-infested, single-port, multi-resonator resonant sensor array structure, and can be used as the reliable data source for further post-readout analysis.

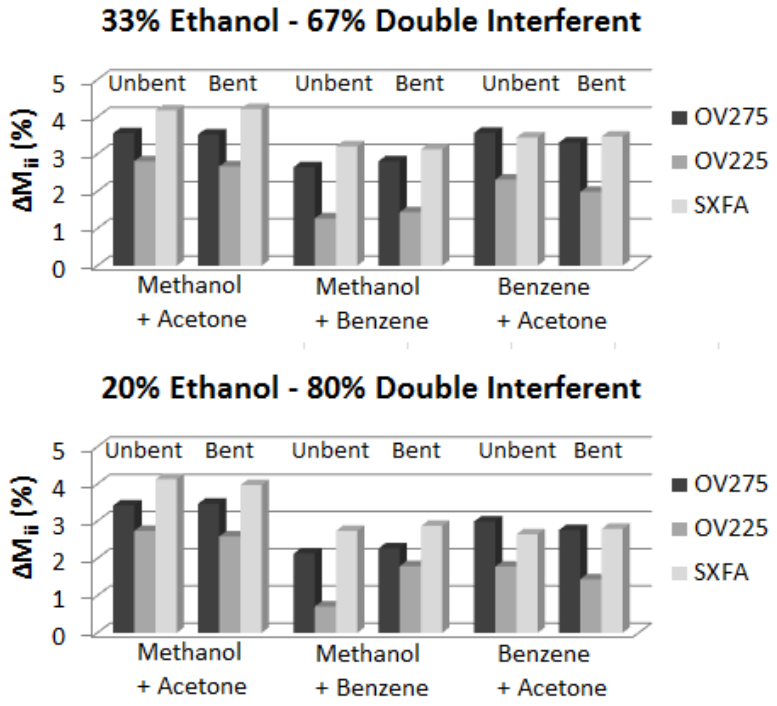

Fig. 5.9.3: Summary of coupling signatures of the gaseous mixtures of ethanol and selected double interferents on the siloxane sensor array with flat and bent physical conditions.

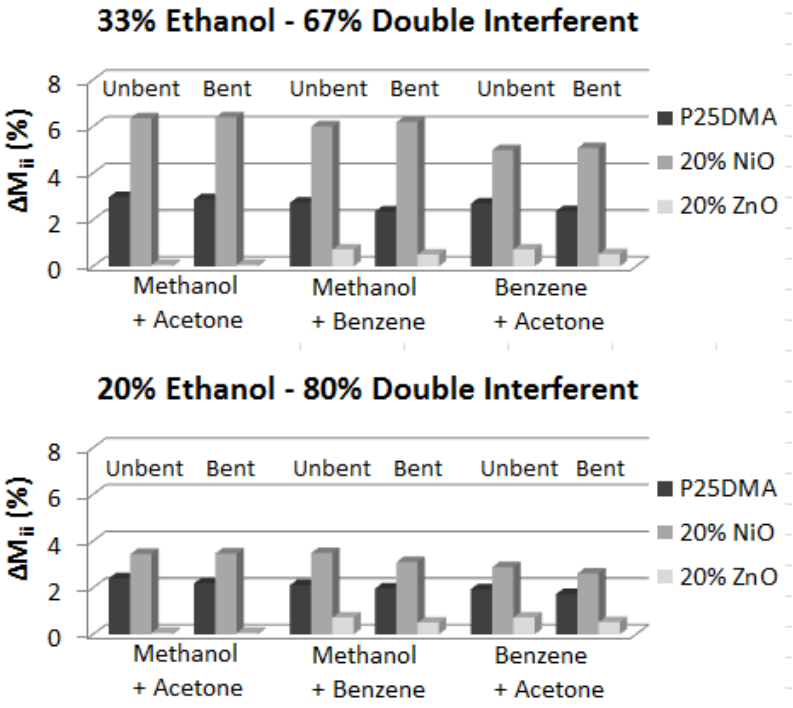

Fig. 5.9.4: Summary of coupling signatures of the gaseous mixtures of ethanol and selected double interferents on the siloxane sensor array with flat and bent physical conditions.

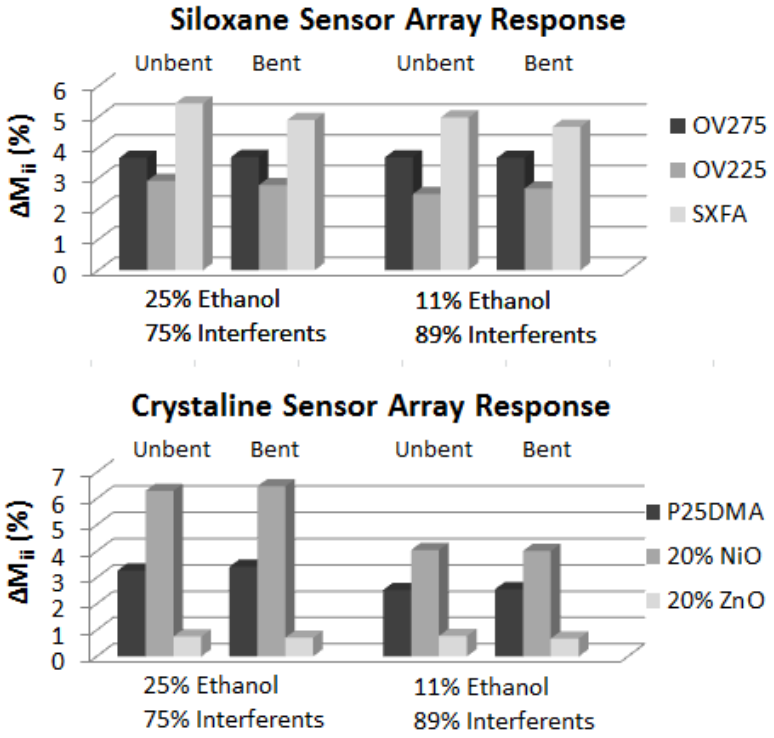

Fig. 5.9.5: Summary of coupling signatures of the gaseous mixtures of ethanol and all three interferents on the siloxane and crystalline sensor array with flat and bent physical conditions.

5.10 SUMMARY

The coupling matrix readout extraction technique has been demonstrated to be capable of not only characterizing single-port, multi-pole resonant sensor array, but also extracting sensor readouts in terms of coupling coefficients, M_{ii}, which are used as coupling signatures to differentiate different chemical analytes detected by the sensor array. Two types of sensor arrays fabricated on Kapton/SU-8 Frame-Flex flexible substrate both demonstrated consistent signature detection capability regardless of the presence of mechanical bending, making the sensor array suitable for foldable and wearable applications. Furthermore, two sets of functional polymers – siloxane-based and crystalline-based – were deployed on the array prototypes to examine the feasibility of the CMRE technique on different sensor configurations. The results confirmed that, regardless of the severity of the frequency-selective loss of the polymer family, the CMRE technique is capable of extracting the required signatures for analyte identification. Finally, through the CMRE technique, the performance superiority of in-house customized P25DMA family crystalline functional polymers was confirmed, with the 20% NiO-doped polymer being very successful in detecting the presence of ethanol, and the 20% ZnO-doped polymer being suitable for detecting the presence of chemical interferents. Finally, the sensor array accompanied with the CMRE technique was shown to be capable of extracting distinctive coupling signatures of various selected gas mixtures to allow further post-readout pattern recognition analyses to be carried out. In the future, more sophisticated loss models can be introduced to the CMRE technique to enable better baseline model mapping and sensor readout extractions.

CHAPTER 6
CONCLUSION

6.1 CONTRIBUTIONS

The research tasks completed in this thesis include polymeric sensing material characterizations, the development of transdermal wearable sensor array infrastructure, and the creation of a mathematical extraction method to obtain readings of individual sensors from the array. The detailed contributions are summarized as follows:

- Characterizing commercially available siloxane-based polymeric sensing materials – namely, OV-225, OV-275, and SC-201 (SXFA) – for their steady-state and transient sensing performance when carried by individual RF resonant sensors towards the gaseous biomarkers and interferents specifications outlined in [24]. Methanol, ethanol, benzene, and acetone were then used in transdermal alcohol detections. Combinations of the three siloxane-based polymers were also shown to generate distinctively different chemical signatures when put in the array configuration, and can thus be used to identify the presence of multiple analytes [20, 55].

- Characterizing in-house synthesized polyaniline crystalline polymeric sensing materials (namely, P25DMA, P25DMA with 20% NiO-dopant, and P25DMA with 20% ZnO-dopant) developed by the Advanced Polymer Institute of University of Waterloo. The polymers were shown to be successfully functionalized through the metallic oxide doping process. Specifically, 20% NiO-doped P25DMA showed strong sensing performance towards ethanol, while 20% ZnO-doped version demonstrated an inhibited sensing capability towards ethanol. Both results concur to the intended functionalization of the polymers. Furthermore, the polyaniline-based polymers were confirmed to have a superior sensing performance compared to siloxane-based ones. All three polymers were shown to be capable of generating distinct chemical signatures for different mixtures of analytes when assembled in an array configuration. Moreover, the polyaniline polymers displayed significantly lower frequency-selective loss and thus can potentially yield higher sensitivity when applied to RF resonant sensors. [55]

- Developing the Frame-Flex flexible substrate preparation and monolithic device packaging process to allow RF resonant sensors to be submerged into the solid islands of the conventional rigid-flex structure. The sensors fabricated with the Frame-Flex process are physically protected by the solid islands from deformation, and the frames on top of the solid islands help expose the chemi-capacitor portion of the resonant sensor for both the high exposure area against gaseous analytes and the convenience and repeatability in polymeric sensing material deposition. The thickness of the frame also helps maintain a sizeable gap between the target skin surface and the polymeric sensing material on the chemi-capacitor, thereby preventing physical damage to the sensor due to skin contact. [58]

- Developing and characterizing the CPW-based solid [20, 55] and flexible chemical sensors [58], as well as the cavity-based combline resonant chemical sensor [59] in order to explore optimal RF resonant structures for different applications. While a CPW-based structure is ideal for flexible sensor design and subsequent transdermal biomarker sensing applications, the cavity-based structure was shown to be highly suitable for integration with existing chemical pipeline infrastructures for many different chemical and biochemical applications.

- Developing the Coupling Matrix Readout Extraction (CMRE) technique along with the Single-Port, Multi-Resonator Resonant Sensor Array structure in order to achieve the most

minimized sensor array design size for a wearable device integration. While the single-port multi-resonator sensor array structure introduced significant inter-sensor interference due to strong coupling among the cascaded resonant sensors, the CMRE technique allows individual sensor readings to be extracted from the S_{11} response curves of the array without the adverse effect of inter-sensor interference. [58]

- The single-port, multi-resonator sensor array structure and the accompanied CMRE technique and the Frame-Flex flexible substrate preparation process have been submitted for patent application.

6.2 FUTURE WORK

Various topics covered in the thesis research would benefit from further engineering and research investigations. The following topics, derived from Chapter 3, comprise future work that would help expand the knowledge basis of individual polymeric sensing materials for gaseous biomarker detections.

- Adding more sample gases, as well as humidity and temperature variations, to the existing experimental trials to fully characterize the sensing materials against a wider, more complete range of chemical analytes and biomarkers.

- Characterizing additional polymeric sensing materials and their performance at RF with the resonant sensor for different sensing applications.

- Developing new dilution and dispensary methods for the polymeric sensing materials of interest to enable more precise and consistent polymer coating applications. Ultimately, as a roadmap to mass production, the process of spin-coating and wafer-wide patterning of the selected polymeric sensing material would also have to be developed.

- Developing the readout circuit that can be integrated with the RF resonant sensor to provide meaningful output for indicating the detection of certain biomarkers. The readout circuit

may also implement certain signal amplification circuits to further improve the sensitivity of the sensor.

- Investigating the feasibility of operating the sensor at higher harmonics to exploit the advantage of increased frequency shifts due to changes in capacitance at the fundamental mode.

The following topics derived from the works presented in Chapter 4 would help improve the performance of the single-port, multi-resonator resonant sensor array, as well as apply the array in different fields of applications.

- Computer integrating the CMRE algorithm with the post-readout multivariate analysis algorithm on a DSP (Digital Signal Processing) chip to enable embedded system integration of the high speed readout circuit / IC and the sensor array.

- Developing a larger sensor array with a more cascaded resonant sensor carrying different polymeric sensing materials in order to open up more practical applications towards ubiquitous ambient sensing, rather than strictly limiting them to the sensing of specific chemical analytes.

- Designing the array with multiple sensors carrying the same sensing material and resonating at the same frequency would help investigate the improvement of sensitivity of the selected polymeric sensing material towards specific analytes. This would help enable the detection of certain specific analytes at a minimum concentration that was historically unachievable with the polymer operated in DC capacitive sensing mode.

- Investigating the additional post-fabrication packaging process to allow more air flow to facilitate polymer desorption and prevent biomarker build-up.

- Incorporating heating elements into the fabrication process to allow accelerated polymer desorption between sampling trials.

APPENDIX A

SUMMARY OF SENSOR CHARACTERISTICS

A1. % Normalized f_0 Sensitivity

Sensor Type	Methanol	Ethanol	Benzene	Acetone
OV225	$3.72e^{-5}$ %/ppm	$3.14e^{-5}$ %/ppm	$1.17e^{-5}$ %/ppm	$6.35e^{-5}$ %/ppm
OV275	$3.33e^{-5}$ %/ppm	$5.91e^{-5}$ %/ppm	$1.71e^{-5}$ %/ppm	$5.56e^{-5}$ %/ppm
SXFA	$4.87e^{-5}$ %/ppm	$5.09e^{-5}$ %/ppm	$9.70e^{-5}$ %/ppm	$3.73e^{-5}$ %/ppm
P25DMA	$8.78e^{-5}$ %/ppm	$1.47e^{-5}$ %/ppm	$3.44e^{-5}$ %/ppm	$6.82e^{-5}$ %/ppm
P25DMA 20% NiO	$5.69e^{-5}$ %/ppm	$1.67e^{-4}$ %/ppm	$8.50e^{-6}$ %/ppm	$2.45e^{-5}$ %/ppm
P25DMA 20% ZnO	$3.23e^{-5}$ %/ppm	$1.61e^{-5}$ %/ppm	$6.75e^{-5}$ %/ppm	$1.07e^{-5}$ %/ppm

A2. % Normalized S_{11} Sensitivity

Sensor Type	Methanol	Ethanol	Benzene	Acetone
OV225	$6.71e^{-4}$ %/ppm	$8.02e^{-4}$ %/ppm	$1.47e^{-4}$ %/ppm	$1.16e^{-3}$ %/ppm
OV275	$6.81e^{-4}$ %/ppm	$9.56e^{-4}$ %/ppm	$1.70e^{-4}$ %/ppm	$1.07e^{-3}$ %/ppm
SXFA	$1.01e^{-3}$ %/ppm	$9.08e^{-4}$ %/ppm	$1.69e^{-3}$ %/ppm	$8.17e^{-4}$ %/ppm
P25DMA	$7.80e^{-4}$ %/ppm	$1.56e^{-3}$ %/ppm	$3.71e^{-5}$ %/ppm	$7.39e^{-4}$ %/ppm
P25DMA 20% NiO	$9.16e^{-4}$ %/ppm	$3.15e^{-3}$ %/ppm	$8.65e^{-5}$ %/ppm	$4.77e^{-4}$ %/ppm
P25DMA 20% ZnO	$2.83e^{-4}$ %/ppm	$1.46e^{-4}$ %/ppm	$6.33e^{-4}$ %/ppm	$8.64e^{-5}$ %/ppm

A3. % Normalized GD_{11} Sensitivity

Sensor Type	Methanol	Ethanol	Benzene	Acetone
OV225	$3.65e^{-3}$ %/ppm	$3.70e^{-3}$ %/ppm	$7.55e^{-4}$ %/ppm	$5.84e^{-3}$ %/ppm
OV275	$3.14e^{-3}$ %/ppm	$3.55e^{-3}$ %/ppm	$8.62e^{-4}$ %/ppm	$4.67e^{-3}$ %/ppm
SXFA	$4.75e^{-3}$ %/ppm	$3.35e^{-3}$ %/ppm	$5.59e^{-3}$ %/ppm	$3.34e^{-3}$ %/ppm
P25DMA	$1.44e^{-3}$ %/ppm	$3.30e^{-3}$ %/ppm	$7.58e^{-4}$ %/ppm	$1.86e^{-3}$ %/ppm
P25DMA 20% NiO	$1.91e^{-3}$ %/ppm	$5.63e^{-3}$ %/ppm	$1.68e^{-4}$ %/ppm	$8.79e^{-4}$ %/ppm
P25DMA 20% ZnO	$3.37e^{-4}$ %/ppm	$1.91e^{-4}$ %/ppm	$7.92e^{-4}$ %/ppm	$1.03e^{-4}$ %/ppm

B1. Transient Characteristics

		Methanol	Ethanol	Benzene	Acetone
OV225	*Response Time,* t_r	75s	75s	60s	75s
	Recovery Time, t_d	105s	45s	90s	45s
	Response Time Constant, τ	60s	60s	45s	60s
OV275	*Response Time,* t_r	75s	75s	75s	75s
	Recovery Time, t_d	90s	135s	135s	90s
	Response Time Constant, τ	45s	60s	60s	60s
SXFA	*Response Time,* t_r	75s	75s	75s	90s
	Recovery Time, t_d	90s	120s	105s	105s
	Response Time Constant, τ	60s	45s	45s	60s
P25DMA	*Response Time,* t_r	45s	60s	105s	60s
	Recovery Time, t_d	60s	60s	45s	60s
	Response Time Constant, τ	30s	60s	75s	45s
P25DMA 20% NiO-Doped	*Response Time,* t_r	45s	45s	60s	45s
	Recovery Time, t_d	45s	60s	90s	60s
	Response Time Constant, τ	30s	30s	45s	30s
P25DMA 20% ZnO-Doped	*Response Time,* t_r	75s	60s	60s	60s
	Recovery Time, t_d	90s	90s	90s	75s
	Response Time Constant, τ	45s	30s	30s	45s

APPENDIX B

FABRICATION PROCESS OF FLEXIBLE RESONANT SENSOR ARRAY

STEP 1: FLEXIBLE SUBSTRATE CUTTING, CLEANING, AND FIRST TEMPORARY BONDING

- Substrate Cutting
  Cut the 5-mil Kapton VN substrate into 2.2" by 2.2" square patches to fit the 3" carrier wafer.

- Substrate Cleaning
  1. Acetone Bath
     Immerse substrates and 3" carrier wafers (glass or silicon) in HPLC-grade acetone for 3 minutes, followed by a HPLC-grade acetone rinse. Flip sides after rinsing, and repeat the bath at least three times.

  2. IPA Bath
     Immerse substrates and carrier wafers in HPLC-grade isopropanol for 3 minutes, followed by a HPLC-grade isopropanol rinse. Flip sides after rinsing, and repeat the bath at least three times.

  3. Drying
     Leave wet substrates and carrier wafers on clean wipe to air dry. Flip sides as needed.

- Temporary Bonding
  1. Isopropanol Temporary Bonding with Capillary Force
     Apply two drops of isopropanol on the carrier wafer. Place the Kapton substrate onto the carrier wafer with the back side facing the carrier wafer. The capillary force of the isopropanol droplets will pull the Kapton wafer flat against the carrier wafer for bonding.

  2. Apply Kapton Tape
     Apply Kapton tape to four corners of the Kapton substrate to fix it to the carrier wafer. Use tools to squeeze out any air bubbles trapped in the tape.

  3. Isopropanol Evaporation Bake
     Place the Kapton substrate-bonded carrier wafer onto the hotplate and bake at 110°C for 2 minutes to fully evaporate the layer of isopropanol.

Step 2: Gold Plating Seed Layer Metallization

- Place Kapton substrates in the Intelvac evaporation system for electroplating seed layer metallization.

- E-Beam Evaporation Layers
    - 30 μm Chromium
    - 50 μm Gold

Step 3: Thick-Film Electroplating Mold Preparation

1. <u>Apply 9.8 μm AZ-9260 Resist onto the Kapton substrate</u>
    - Spin-Coating Recipe
        - 100 rpm – 10 seconds
        - 500 rpm – 10 seconds
        - 1500 rpm – 40 seconds
        - Soft Bake - 90 ˚C – 60 seconds
        - Resultant Thickness – 9.8um

2. <u>Rehydration Period</u>
   Place the substrate in the petri dish with partially closed lids to allow for free air flow while preventing dust accumulation on top.

   Allow for at least 1 hour of rehydration time before proceeding to the next step.

3. Resist Exposure with MJB4 Aligner
    - AZ 9260 Exposure Recipe
        - Power – 25.4W
        - Exposure Steps
            - 3 steps, 12.5 seconds per step
            - Break Time – 10 seconds between steps
        - **<u>No post-exposure baking is required</u>**

4. Heat and Agitation Assisted Development
    - AZ 9260 Development Recipe
        - Developer – AZ Kwik Strip Developer
        - Temperature – 40 ˚C
        - Agitation – 500 rpm
        - Development Time – 9 minutes

- No hard-baking required.
- Development time varies with the completeness of the rehydration process.

Step 4: Gold Electroplating

- AZ 9260 Plating Mold Descum
  - Descum Recipe in Trion Reactive Ion Etcher (RIE)
    - Chamber Pressure – 50 mTorr
    - Reactive Ion Etching Power – 50 W
    - Inductive Coupled Plasma Power – 150 W
    - Oxygen (O_2) Flow – 30 sccm
    - Time – 15 seconds
    - Inspect after descum

- Gold Plating Preparation
  - Clean the metallic contact with an acetone-wetted cotton swab.
  - Fix the plating alligator clips onto the metallic contact on the Kapton substrate.
  - Fix the substrate onto the Teflon substrate holder.
  - Thoroughly DI-water rinse the substrate and holder.
  - Connect the substrate onto the cathode of the plating system, and immerse the substrate and the Teflon holder into the plating solution.

- Gold Plating Recipe
  - Current – 60 mA
  - Time – 1 hour
  - Resultant Thickness ~6.5 um
  - Thorough DI-water rinse of the substrate after plating

Step 5: Lift-Off Preparation: Chromium Mask

- **DO NOT PERFORM DEHYDRATION BAKE** due to thermal cracking of the AZ 9260 mold.

- Place substrates in the Intelvac evaporation system for lift-off mask metallization.

- E-Beam Evaporation Layers
  - 30 μm Chromium

Step 6: Mold Lift-Off

- Heat and Agitation Assisted Lift-Off
    - AZ 9260 Lift-Off Recipe
        - Developer – AZ Kwik Strip Developer
        - Temperature – 40 ˚C
        - Agitation – 500 rpm
        - Development Time – 15 minutes

Step 7: Plating Seed Layer Removal

- Remove the Kapton substrate from the temporary bonding. Rinse thoroughly with DI-water, followed by HPLC-grade isopropanol.

- Gold Seed Layer Removal
    - Etchant – CE200 Gold Etchant
    - Time – 50 seconds
    - Thorough DI-water and HPLC-grade isopropanol rinse

- Chromium Adhesion Layer / Mask Removal
    - Etchant – Chromium Etchant
    - Time – 15 seconds
    - Thorough DI-water and HPLC-grade isopropanol rinse

- Inspect with microscope after removing each layer.

Step 8: Second Temporary Bonding

1. <u>Isopropanol Temporary Bonding with Capillary Force</u>
   Apply two drops of isopropanol on the carrier wafer. Place the Kapton substrate onto the carrier wafer with back side facing the carrier wafer. The capillary force of the isopropanol droplets will pull the Kapton wafer flat against the carrier wafer for bonding.

2. <u>Apply Kapton Tape</u>
   Apply Kapton tape to four corners of the Kapton substrate to fix it to the carrier wafer. Use tools to squeeze out any air bubbles trapped in the tape.

3. Isopropanol Evaporation Bake
   Place the Kapton substrate-bonded carrier wafer onto the hotplate and bake it at 110˚C for 2 minutes to fully evaporate the layer of isopropanol.

Step 9: Thick-Film SU-8 Mold

1. Apply 100 µm SU-8 2035 Resist onto the Kapton substrate
   - Spin-Coating Recipe
     - 100 rpm – 10 seconds
     - 500 rpm – 10 seconds
     - 1200 rpm – 40 seconds
     - Soft Bake Step 1 – 65 ˚C, 5 minutes
     - Soft Bake Step 2 – 95 ˚C, 12 minutes
     - Soft Bake Step 3 – 65 ˚C, 5 minutes
     - Cool Down – 10 minutes
     - Resultant Thickness – ~100 um

2. Rehydration Period
   Place the substrate in the petri dish with partially closed lids to allow for free air flow while preventing dust accumulation on the top.

   Allow for at least 4 hours of rehydration time before proceeding to the next step.

3. Resist Exposure with MJB4 Aligner
   - SU-8 Exposure Recipe
     - Power – 25.4W
     - Exposure Steps
       - 3 steps, 10 seconds per step
       - Break Time – 10 seconds between steps
     - Post-Exposure Bake Step 1 – 65˚C, 5 minutes
     - Post-Exposure Bake Step 2 – 95˚C, 5 minutes
     - Post-Exposure Bake Step 1 – 65˚C, 5 minutes
     - Cool Down – 10 minutes
     - Inspect for proper exposure

4. Heat and Agitation Assisted Development
   - SU-8 Development Recipe
     - Developer – SU-8 Developer / Acetone
     - Temperature – 40 ˚C
     - Agitation – 500 rpm
     - Development Time – 13.5 minutes

- No hard bake required.
- Development time varies with the completeness of rehydration process.

5. Substrate Rinsing and Temporary Bonding Removal
   - Remove the Kapton substrate from the temporary bonding.
   - Rinse the substrate only with isopropanol. **DO NOT RINSE WITH DI WATER.**
   - If white residue is observed, repeat step 4.
   - Do not hard bake to avoid excessive stress build-up.

Step 10: Third Temporary Bonding – Flipside

1. Isopropanol Temporary Bonding with Capillary Force
   Apply two drops of isopropanol on the carrier wafer. Place the Kapton substrate onto the carrier wafer with **FRONT SIDE** facing the carrier wafer. The capillary force of the isopropanol droplets will pull the Kapton wafer flat against the carrier wafer for bonding.

2. Apply Kapton Tape
   Apply Kapton tape to four corners of the Kapton substrate to fix it to the carrier wafer. Use tools to squeeze out any air bubbles trapped in the tape.

3. Isopropanol Evaporation Bake
   Place the Kapton substrate-bonded carrier wafer onto the hotplate and bake at 110˚C for 2 minutes to fully evaporate the layer of isopropanol.

Step 11: Oxide Mask Deposition

1. Silicon Dioxide Deposition in Trion Plasma-Enhanced Chemical Vapour Deposition (PECVD)
   - Chamber Pressure – 900 mTorr
   - Chamber Temperature – 250˚C
   - Power – 60 W
   - Gas Flows
     - Silane (SiH_4) – 5 sccm
     - Nitrogen (N_2) – 118 sccm
     - Nitrous Oxide (N_2O) – 140 sccm
   - Deposition Time – 540 seconds
   - Resultant Thickness ~ 500 nm

Step 12: Oxide Mask Patterning I: Auto-Diceline Precursor Pattern

1. AZ-3312 Photoresist Pattern on the Kapton substrate
    - Spin Coat Recipe
        - 100 rpm – 10 seconds
        - 500 rpm – 10 seconds
        - 3000 rpm – 30 seconds
        - Soft Bake – 110 ˚C
        - Rehydration Process Time – 2 minutes
    - Exposure Recipe
        - Power – 25.4 W
        - Time – 4 seconds
        - Post Exposure Bake - 110 ˚C
    - Potting Development
        - Developer – AZ MIF-300 (Metallic Ion-Free) Developer
        - Temperature – 25 ˚C
        - Time – 40 seconds
        - Agitation – 5 seconds before removal from the developer.

2. AZ-3312 Pattern Descum
    - Descum Recipe in Trion Reactive Ion Etcher (RIE)
        - Chamber Pressure – 50 mTorr
        - Reactive Ion Etching Power – 50 W
        - Inductive Coupled Plasma Power – 150 W
        - Gas Flow
            - Oxygen (O_2) – 30 sccm
        - Time – 15 seconds
        - Inspect after descum

3. Oxide Mask Etching
    - Oxide Etching Recipe in Trion Reactive Ion Etcher
        - Chamber Pressure – 250 mTorr
        - Reactive Ion Etching Power – 100 W
        - Inductive Coupled Plasma Power – 250 W
        - Gas Flow
            - Halocarbon (CF_4)– 30 sccm
        - Time – 600 seconds
        - Inspect after descum

Step 13: Kapton Dry Etching I: Auto-Diceline Precursor Etch

- Kapton (Polyimide-Derivative) Etching Recipe in Trion Reactive Ion Etcher
    - Chamber Pressure – 50 mTorr
    - Reactive Ion Etching Power – 300 W
    - Inductive Coupled Plasma Power – 50 W
    - Gas Flow
        - Oxygen (O_2) – 30 sccm
    - Time – 18 minutes
    - Resultant Etched Depth – 1 mil (25.4 um)
    - Pause every 10 minutes to allow the nitrogen purge to cool down and prevent residue repolymerization on the substrate surface.

Step 14: Oxide Mask Patterning II: Trench Pattern

1. AZ-3312 Photoresist Pattern on the Kapton substrate
    - Spin Coat Recipe
        - 100 rpm – 10 seconds
        - 500 rpm – 10 seconds
        - 3000 rpm – 30 seconds
        - Soft Bake – 110 ˚C
        - Rehydration Process Time – 2 minutes
    - Exposure Recipe
        - Power – 25.4 W
        - Time – 4 seconds
        - Post Exposure Bake - 110 ˚C
    - Potting Development
        - Developer – AZ MIF-300 (Metallic Ion-Free) Developer
        - Temperature – 25 ˚C
        - Time – 40 seconds
        - Agitation – 5 seconds before removal from the developer.

2. AZ-3312 Pattern Descum
    - Descum Recipe in Trion Reactive Ion Etcher (RIE)
        - Chamber Pressure – 50 mTorr
        - Reactive Ion Etching Power – 50 W
        - Inductive Coupled Plasma Power – 150 W
        - Gas Flow
            - Oxygen (O_2) – 30 sccm
        - Time – 15 seconds
        - Inspect after descum

3. Oxide Mask Etching
    - Oxide Etching Recipe in Trion Reactive Ion Etcher
        - Chamber Pressure – 250 mTorr
        - Reactive Ion Etching Power – 100 W
        - Inductive Coupled Plasma Power – 250 W
        - Gas Flow
            - Halocarbon (CF_4)– 30 sccm
        - Time – 600 seconds
        - Inspect after descum

Step 15: Kapton Dry Etching II: Diceline + Trench Etch

- Kapton (Polyimide-Derivative) Etching Recipe in Trion Reactive Ion Etcher
    - Chamber Pressure – 50 mTorr
    - Reactive Ion Etching Power – 300 W
    - Inductive Coupled Plasma Power – 50 W
    - Gas Flow
        - Oxygen (O_2) – 30 sccm
    - Time – 72 minutes
    - Resultant Etched Depth – 4 mil (101.6 um)
    - Pause every 10 minutes to allow nitrogen purge to cool down and prevent residue repolymerization on the substrate surface.

- Collect the self-diced devices from the carrier wafer

Step 16: Device Cleaning

1. <u>Acetone Bath</u>
   Immerse devices in HPLC-grade acetone for 3 minutes, followed by HPLC-grade acetone rinse. Flip sides after rinsing and repeat the bath at least three times.

2. <u>Isopropanol Bath</u>
   Immerse devices in HPLC-grade isopropanol for 3 minutes, followed by an HPLC-grade isopropanol rinse. Flip sides after rinsing and repeat the bath at least three times.

3. <u>Drying</u>
   Leave wet devices upright on clean wipe to air dry.

Step 17: SMA Connector Bonding

- Wafer Padding
  - 0.25" x 0.25" 5-mil Kapton tape patches – 7 pieces
  - Place all 7 patches under the Kapton substrate on the CPW feed line side of the device

- Insert the padded sensor into the connector slot of the SC-8447 SMA connector with a 40-mil clip height.

- Apply silver epoxy on the following areas:
  - Ground pins of the connector and the ground patches of the CPW line.
  - Signal pins of the connector and the signal line of the CPW line.

- Epoxy Curing Bake
  - Temperature – 100˚C
  - Time – 2 hours

- Inspect the sensor performance with vector network analyzer (VNA).

Step 18: Polymeric Sensing Material Deposition and Curing

- Siloxane Family Polymeric Sensing Material Deposition Recipe

Polymeric Sensing Material	Dilution Solvent (HPLC-Grade)	Dilution Ratio (w.t. %)	Deposition Temp. (°C)	Deposition Tools	Curing
OV-225	Acetone, Agitation	< 0.01	-10	VWR Micropipette	80°C, 30m
OV-275	Acetone, Agitation	< 0.01	-10	VWR Micropipette	80°C, 30m
SXFA	Acetone, Agitation	< 0.01	-10	VWR Micropipette	80°C, 30m

- Polyaniline Family Polymeric Sensing Material Deposition Recipe

Polyaniline Sensing Material	Dilution Solvent (HPLC-Grade)	Dilution Ratio (w.t. %)	Deposition Temp. (°C)	Deposition Tools	Curing
P25DMA	NMP, Agitation	1 ~ 3	25	VWR Micropipette / Microplotter	85°C, 24 h
P25DMA, 20% NiO-Doped	NMP, Agitation	1 ~ 3	25	VWR Micropipette / Microplotter	85°C, 24 h
P25DMA, 20% ZnO-Doped	NMP, Agitation	1 ~ 3	25	VWR Micropipette / Microplotter	85°C, 24 h

REFERENCES

[1] G.D. Webster, H.C. Gabler, "Feasibility of transdermal ethanol sensing for the detection of intoxicated drivers", *51st Annual Proceedings of Association for the Advancement of Automotive Medicine,* 2007.

[2] A.E. Jones, R.L. Summers, "Detection of Isopropyl Alcohol in a Patient with Diabetic Ketoacidosis", *The Journal of Emergency Medicine*, Vol. 19, No. 2, pp. 165-168, 2000.

[3] Z. Syed, W.S. Leal, "Acute olfactory response of Cules mosquitoes to a human- and bird-derived attractant", *Proceedings of National Academic of Science*, Vol. 106, No. 44, pp. 18803-18808, 2009.

[4] M. Philips, "Sweat-Patch test for alcohol consumption: rapid assay with an electrochemical detector", *Alcohol Clin. Exp. Res*., Vol 6, No. 4, pp. 532-534, 1982.

[5] J.S. Hawthorne, M.H. Wojcik, "Transdermal Alcohol Measurement: A Review of the Literature", *Canadian Society of Forensic Science Journal*, Vol. 39, No. 2, pp. 65-71, 2006.

[6] S.E. Luczak, I.G. Rosen, J. Weiss, "Determining Blood and / or Breath Alcohol Concentration from Transdermal Alcohol Data", *American Control Conference 2013*, Washington, DC, 2013.

[7] M.A. Dumett, I.G. Rosen, J. Sabat, A. Shaman, L. Tempelman, C. Wang, R.M. Swift, "Deconvolving an estimate of breath measured blood alcohol concentration from biosensor collected transdermal ethanol data", *Applied Mathematics and Computation*, Vol. 196, pp. 724-743, 2008.

[8] J.C. Anderson, M.P. Hlastala, "The kinetics of transdermal ethanol exchange", *J. APpl. Physiol.*, Vol. 100, pp. 649-655, 2006.

[9] Electronics Tutorials, "Capacitance of a Parallel Plate Capacitor," Introduction to Capacitors, Available: http://www.electronics-tutorials.ws/capacitor/cap_1.html

[10] S.V. Patel, T.E. Mlsna, B. Fruhberger, E. Klaassen, S. Cemalovic, R.D. Baselt, "Chemicapacitive microsensors for volatile organic compound detection", Sensors and Actuators, Vol. B: Chemical, Issue 96, pg. 541-553, 2003.

[11] F. Lisdat, D. Schafer, "The use of electrochemical impedance spectroscopy for biosensing", *Anal. Bioanal. Chem.*, Vol. 391, pp. 1555-1567, 2008.

[12] F.G. Banica, "Conductometric Sensors", *Chemical Sensors and Biosensors – Fundamentals and Applications*, Ed. New York: Wiley, 2012, pp. 386-395.

[13] N.F. Sheppard, R.C. Tucker Jr., C. Wu, "Electrical Conductivity Measurements using Microfabricated Interdigitated Electrodes", *Anal. Chem.*, Vol. 65, pp. 1199-12.02, 1993.

[14] T.M. Anh, S.V. Dzyadevych, M.C. Van, N.J. Renault, C.N. Duc, J. Chovelon, "Conductometric - Tyrosinase Biosensor for the Detection of Diuron, Atrazine, and Its Main Metabolites", *Talanta*, Vol. 63, pp. 365-370, 2004.

[15] M.E. Khater, E. Abdel-Rahman, "Binary Gas Sensors", presented at Auto 21 Conference, 2013.

[16] M.E. Khater, E.M. Abdel-Rahman, A.H. Nayfeh, "A Mass Sensing Technique for Electrostatically-Actuated MEMS", *ASME IDETC/CIE 2009*, San Diego, California, USA, 2009.

[17] S.Z. Lulec, C. Sagiroglu, A. Mostafazadeh, E. Ermek, E. Timurdogan, Y. Leblebici, H. Urey, "Simultaneous Self-Sustained Actuation and Parallel Readout with MEMS Cantilever Sensor Array", *IEEE MEMS 2012*, Conference Proceedings, pp. 644-647, Paris, France, 2012.

[18] B.L. Allen, P.D. Kichambare, A. Star, "Carbon Nanotube Field-Effect-Transistor-Based Biosensors, "*Advanced Materials*, Vol. 19, pp. 1439-1451, 2007.

[19] R.J. Young, *Introduction to Polymers*, Chapman & Hall, 1987.

[20] W.T. Chen, K.M.E. Stewart, J. Carroll, R. Mansour, E. Abdel-Rahman, A. Penlidis, "Novel Gaseous Phase Ethanol Sensor Implemented with Underloaded RF Resonator for Sensor-Embedded Passive Chipless RFIDs", in *Transducer 2013 Conf. Proc.,* Barcelona, Spain, 2013, pp. 2059-2062.

[21] P. Lobotka, P. Kunzo, E. Kovacova, L. Vavra, Z. Kirzanova, V. Smatko, J. Stejskal, E.N. Konyushenko, M. Omastova, Z. Spitalsky, M. Micusik, L. Krupa, "Thun Polyaniline and Polyaniline/Carbon nanocomposite films for gas sensing", *Thin Solid Films*, Vol. 519, pp. 4123-4127, 2011.

[22] A. Choudhury, "Polyaniline/Silver Nanocomposites: Dielectric Properties and Ethanol Vapour Sensitivity", *Sensors and Actuators B: Chemical*, Vol. 138, pp. 318-325, 2009.

[23] J. Huang, T. Yang, Y.F. Kang, Y. Wang, S.R. Wang, "Gas sensing performance of polyaniline/ZnO organic-inorganic hybrids for detecting COVs at low temperature", *Journal of Natrual Gas Chemistry*, Vol. 20, pp. 515-519, 2011.

[24] *Driver Alcohol Detection System for Safety: Subsystem Performance Specification*, QinetiQ North America / Foster-Miller, Inc. Technology Solution Group, Waltham, MA, USA, 2008.

[25] J. Covington, "Background: What's an Electronic Nose?", *Warwick Engineering in Biomedicine*, Warwick School of Engineering, Aug. 2012.

[26] M. Esashi, "Resonant Sensors by Silicon Micromachining", *IEEE International Frequency Control Symposium 1996*, Conference Proceedings, pp. 609-614, 1996.

[27] M.P.J Gaudreau, R.A. Weisenseel, "Resonant Sensor System and Method", U.S. Patent 5,942,991, issued August 24, 1999.

[28] G. Subramanyam, "Resonant Sensor Capable of Wireless Interrogation", U.S. Patent 7,922,975 B2, issued April 12, 2011.

[29] R. C. Cameron, C. M. Kudsia and R. R. Mansour, "Design and Physical Realization of Coupled Resonator Filters", Microwave Filters for Communication Systems - Fundamentals, Design and Applications, 1st Edition, Hoboken NJ, John Wiley & Sons, Inc., 2007, Chp. 14, Sec. 3, pp. 511-512.

[30] D.M. Pozar, "Electromagnetic Theory", Microwave Engineering, 3rd Edition, Hoboken NJ, John Wiley & Sons, Inc., 2005, Chp. 1, Sec. 1, p. 18.

[31] Gorden M. Coutts, "Miniature MEMS-Based Adaptive Antennas on Flexible Substrate", Ph. D. Thesis, Dept. Elect. Eng., University of Waterloo, Waterloo, ON, Canada, 2005.

[32] Kusu Guiati, Hae-Seung Lee, "Eliminating the Analog Circuit Bottleneck – Cambridge Analog Technologies' Ultra Low Power High Performance Analog / Digital Conversion", *Cambridge Analog Technologies, Whitepaper,* CAT-TB-0903 Rev. 1.2, 2010.

[33] Reitz, J., Milford, F. and Christy, R., *Foundations of Electromagnetic Theory*, 4th Ed. Addison-Wesley, 1993.

[34] Jose M. L. Comeras, "New Functional Polymers for Sensors, Smart Materials, and Solar Cells", Ph.D. Thesis, Sept. of Chemistry, Massachusetts Institute of Technology, MA, USA, 2012.

[35] T. Nenov, S. Yordanov, "Ceramic Sensor Device Materials", *Sensors and Actuators, Vol. B: Chemical*, Vol. 8, Issue 1, April 1992, pp. 117-122.

[36] Ing. H.D. Ngo, Basic Modules for Chemical Sensors, Figure 1, Available: http://www-mat.ee.tu-berlin.de/research/chemsens/chemsens.htm

[37] J. Janata (Sept. 2010), "Electrochemical Sensors", *Electrochemistry Encyclopedia*, Figure 7, Available: http://knowledge.electrochem.org/encycl/art-s02-sensor.htm

[38] Sensors – Preliminary Product Datasheet, Innovation Centre, University of Exeter, Devon, England, March 2011.

[39] Rooks Heath Science, "Goldsmith's 2013: Practical – Hydrogen Fuel Cell", Rooks Heath College, October 2013. Available: http://rooksheathscience.com/2013/10/

[40] P. Pistor, V. Chu, D.M.F. *et al*. "pH sensitive photoconductor based on poly (para-phenylene vinylene)", *Sensors and Actuators B: Chemical*, Vol. 123, pp. 153-157, 2007.

[41] R.A. Potyrailo, C. Surman, W.G. Morris, S. Go, "Selective Detection of Chemical Species in Liquids and Gases using Radio-Frequency Identification (RFID) Sensors", TRANSDUCERS 2009. International, pp.1650-1653, June 21-25, 2009.

[42] S.Zhang, P. Pasupathy, D.P. Neikirk, "Microfabricated Self-Resonant Structure as a Passive Wireless Dielectric Constant and Conductivity Sensor", *Mycrosyst. Technol.* vol. 18, pp. 885-891, 2012.

[43] Y. Zhao, S.H. Kim, Y. Li, B. Pan, X.S. Wu, M. Tentzeris, J. Parapolymerou, M.G. Allen, "A Micromachined Airflow Sensor Based on RF Evanescent-Mode Cavity Resonator", *International Microwave Symposium Digest 2008*, pp. 1199-1202, Atlanta, GA, 2008.

[44] G. Gennarelli, S. Romeo, M.R. Scarfi, F. Soldovieri, "A Microwave Resonant Sensor for Concentration Measurements of Liquid Solutions", *IEEE Sensors Journal*, Vol. 13, No. 15, pp. 1857-1864, May 2013.

[45] E. Fratticcioli, M. Dionigi, R. Sorrentino, "An Accurate and Low Cost Complex Permittivity Measurement System using a Planar Resonant Sensor", *32nd European Microwave Conference*, pp. 1-4, Milan, Italy, 2002.

[46] R.A. Potyrailo, W.G. Morris, "Wireless Resonant Sensor Array for High-Throughput Screening of Materials", *Review of Scientific Instruments*, Vol. 78, No. 072214, pp. 1-6, 2007.

[47] J.J. Carr, J.M. Brown, "Sensor Terminology", Introduction to Biomedical Equipment Technology, 3rd Edition, National Instruments & Prentice Hall, 2010. Available: http://zone.ni.com/devzone/cda/ph/p/id/227#toc8.

[48] K.M.E. Stewart, A. Penlidis, "Novel Test System for Gas Sensing Materials and Sensors", *Macromolecular Symposia, Polymer Reaction Engineering VIII*, Vol. 324, pp. 11-18, 2013.

[49] E. Nyman, A. Palmlov, "The elimination ethyl alcohol in sweat", *Skand. Arch. Physiol.*, Vol. 74, pp. 154-159, 1936.

[50] "Adsorption or Absorption", Figure # MTJ 23/6, 02, BioSite, August 2008. Available: http://www.biosite.dk/leksikon/adsorption.htm

[51] B. Chichkov, "Two-Photon Polymerization – High Resolution 3D Laser Technology and its Applications", Nanoelectronics and Photonics: From Atoms to Materials, Devices, and Architectures, Springer Science + Business Media, LLC., 2008.

[52] G. Wiger, "Polymers – Very Long Chains", *CSUDH WWW Project for Chemistry – Chemistry 240*, 2001. Available: http://chemistry2.csudh.edu/rpendarvis/Polymer.html

[53] M.A. Gauthier, J. Luo, D. Calvet, C. Ni, X.X. Zhu, M. Garon, M.D. Buschmann, "Degree of crosslinking and mechanical properties of crosslinked poly(vinyl alcohol) beads for use in solid-phase organic synthesis", *Polymer*, Vol. 45, pp. 8201-8210, 2004.

[54] M. Butler, Y. Yamazoe, P. Vanysek, M. Aizawa, *Chemical Sensors IV*, The Electrochemical Society, Inc., 10 South Main Street, Pennington, NY 08534-2896, 1999.

[55] W.T. Chen, K.M.E. Stewart, R.R. Mansour, A. Penlidis, "*Novel Undercoupled Radio-Frequency (RF) Resonant Sensor for Gaseous Ethanol and Interferents Detection*", submitted to Sensors and Actuators Vol. A: Physical. (Accepted)

[56] W.T. Chen, R.R. Mansour, and J. Carroll, "A Coupling Matrix-Based Readout Technique for Single-Port Multi-Resonator Passive Sensor Array", presented at *IEEE MTT-S International Microwave Symposium*, Tampa Bay, FL, USA, June 1-6, 2014.

[57] *TruTouch Technology Overview White Paper*, TruTouch Technologies, Inc., Sudbury, MA, USA, 2005. Available: http://www.trutouchtechnologies.com/sites/default/files/TruTouchTechnologyOverview.pdf

[58] W.T. Chen, K.M.E. Stewart, C.K. Yang, R.R. Mansour, J. Carroll, A. Penlidis, "*Wearable RF Sensor Array Implementing Coupling-Matrix Readout Extraction Technique*", submitted to IEEE Transactions on Microwave Theory and Techniques. (Submitted, under 3rd revision)

[59] W.T. Chen, K.M.E. Stewart, R.R. Mansour, A. Penlidis, "Polymeric Sensing Material-based Selectivity-enhanced RF Resonant Cavity Sensor for Volatile Organic Compound (VOC) Detection", submitted to *IEEE MTT-S International Microwave Symposium 2015*. (Accepted)

[60] Schuetzle Hammerle, *Fundamentals and Applications of Chemical Sensors,* American Chemical Society, 1986.

[61] *Dupont Kapton E* Polyimide Sheet, Technical Data Sheet.

[62] *Dupont Kapton HN* Polyimide Sheet, Technical Data Sheet.

[63] *Dupont Pyralux AC Copper-Clad* Laminated Sheet, Technical Data Sheet.

[64] *Dupont Pyralux AX Copper-Clad* Laminated Sheet, Technical Data Sheet.

[65] Shu Peng, James O'Keeffe, Chengyu Wei, K. Cho, Jing Kong, Robert Chen, Nathan Franklin, H. Dai, *"Carbon Nanotube Chemical and Mechanical Sensors"*, 3rd International Workshop on Structural Health Monitoring, Conference Proceeding, pp. 1-8, 2002.

[66] Jaehyun Chung, Kyong-Hoon Lee, Junghoon Lee, *"Multi-Walled Carbon Nanotube Sensors"* ,Transducer 2003 / 12th International Conference on Solid-State Sensors, Actuators, and Microsystems, Vol. 1, pp. 718-721, June 8-12, 2003.

[67] King Wait Chiu Lai, Carmen Kar Man Fung, Victor Tak Sing Wong, Mandy Lai Yi Sin, Wen Jung Li, and Chung-Ping Kwong, *"Development of an Automated Microspotting System for Rapid Dielectrophoretic Fabrication of Bundled Carbon Nanotube Sensors"*, IEEE Transactions on Automation Science and Engineering, Vol. 3, no. 3, pp. 218-227, July 2006.

[68] Ju-Hyung Yun, Han Chang-Soo, Joondong Jim, Jin-Won Song, Dong-Hun Shin, and Young-Geun Park, *"Fabrication of Carbon Nanotube Sensor Device by Inkjet Printing,"* 3rd IEEE International Conference on NEMS / Nano/Micro Engineered and Molecular Systems, pp. 506-509, January 6-9, 2008.

[69] James Calusdian and Xiaoping Yun; Jing Li, Yijiang Lu, and Meyya Meyyappan, *"Design and Testing of a Wireless Portable Carbon Nanotube-Based Chemical Sensor System"*, 6th IEEE Conference on Nanotechnology, pp. 794-797, June 17-20, 2006.

[70] SeGi Yu and Whikun Yi, *"Single-Walled Carbon Nanotubes as a Chemical Sensor for SO_2 Detection"*, IEEE Transactions on Nanotechnology, Vol. 6, No. 5, pp. 545-548, 2007.

[71] Qi Zhang, Lars Nyborg, Urban Jelvestam, Zonghe Lai, Zhaonian Cheng, Johan Liu; "*Adhesion Study of Copper Layer Deposited onto Liquid Crystalline Polymer for Electronic Packaging"*, Conference on High Density Microsystem Design and Packaging and Component Failure Analysis, pp. 1-6, June 2005.

[72] Carmen K. M. Fung, Wen J. Li, *"Ultra-Low-Power and High-Frequency-Response Carbon Nanotube Based MEMS Thermal Sensors",* IEEE International Conference on Intelligent Robots and Systems, Vol. 3, pp. 2371-2376, October 27-31, 2003.

[73] Carmen K. M. Fung, Maggie Q. H. Zhang, Zaili Dong and Wen J. Li, *"Fabrication of CNT-Based MEMS Piezoresistive Pressure Sensors Using DEP Nanoassembly",* Proceedings of 5th IEEE Conference on Nanotechnology, Vol. 1, pp. 199-202, July 11-15, 2005.

[74] Ashwin Mohan, Ajay P. Malshe, Shyam Aravamudhan, Shekhar Bhansali, *"Piezoresistive MEMS Pressure Sensor and Packaging for Harsh Oceanic Environment",* 54th Electronics Components and Technology Conference, Vol. 1, pp. 948-950, June 1-4, 2004.

[75] Yixian Ge, Ming Wang, Xuxing Chen, Haitao Yan, Hua Rong, *"An Optical MEMS Pressure Sensor Based on Phase Demodulation",* Sensors and Actuators A: Physical, Vol. 143, No. 2, pp. 224-229, May 16, 2008.

[76] L.-P. Wang, K. Deng, L. Zou, R. Wolf, R. J. Davis, and S. Trolier-McKinstry, *"Microelectromechanical Systems (MEMS) Accelerometers Using Lead Zirconate Titanate Thick Films",* IEEE Electron Device Letters, Vol. 23, No. 4, pp. 182-184, April 2002.

[77] Lrobert Stewart, Robert Thede, Paul Couch, Dave Tarrant, *"High G MEMS Accelerometer for Compact Kinetic Energy Missile",* Position Location and Navigation Symposium, pp. 20-25, April 26-29, 2004.

[78] John E. Rogers, Ramesh Ramadoss, Phillip M. Ozmun, Robert N. Dean, *"MEMS Accelerometer Fabricated Using Printed Circuit Processing Techniques",* IEEE International Symposium on Industrial Electronics, pp. 3250-3254, June 4-7, 2007.

[79] Tai-Ran Hsu, *MEMS and Microsystems –Design, Manufacture, and Nanoscale Engineering*, John Wiley & Sons, Inc. 2008.

[80] Nicolae Lobontiu and Ephrahim Garcia, *Mechanics of Microelectromechanical Systems*, Kluwer Academic Publishers, 2005.

[81] Walter Wunderlich and Walter D. Pilkey, *Mechanics of Structures – Variational and Computational Methods,* 2nd Edition, CRC Press, 2003.

[82] Nelson R. Bauld Jr, *Mechanics of Materials*, Wadsworth, Inc., 1982.

[83] Laszlo Peter Kollar, George S. Springer, *Mechanics of Composite Structures*, Cambridge University Press, 2004.

[84] Stephen D. Senturia, *Microsystem Design*, 1st Edition, Chapter 5, Springer Inc., 2004.

[85] Andrew J. Deeks, Hong Hao, *Developments in Mechanics of Structures and Materials*, CRC Press, 2004.

[86] Byunghoon Bae, Richard I. Masel, and Mark A. Shannon, "*A Touch-Mode Capacitance Microvalve Equipped with High Speed and Pressure Microsecond Switching Performance*", 19th IEEE Conference on Micro Electro Mechanical Systems, pp. 766-769, Intanbul, Turkey, January 22-26, 2006.

[87] Joseph A. Potkay and Kensall D. Wise, "*An Electrostatically Latching Thermopneumatic Microvalve with Closed-Lope Position Sensing*", 18th IEEE Conference on Micro Electro Mechanical Systems, pp. 415-418, January 30-February 3, 2005.

[88] Rebeiz G M, *RF MEMS: Theory, Design and Technology*, New York: Wiley, 2002.

[89] P G Steeneken, Th G S M Rijks, J T M van Beek, M J E Ulenaers, J De Coster and R Puers, "*Dynamics and Squeeze Film Gas Damping of a Capacitive RF MEMS Switch*", Journal of Micro Electro Mechanical Systems, Vol. 15, pp. 176, October 25, 2004.

[90] Jungyul Park, Jinseok Kim, Dukmoon Roh, Seokho Park, Byungkyu Kim and Kukjin Chun, "*Fabrication of 3D Thin Polymer Structures for Hybrid Sensors and Actuators*", 19th IEEE Conference on Micro Electro Mechanical Systems, pp. 310-313, Intanbul, Turkey, January 22-26, 2006.

[91] Rudolf H. Krondorfer, Yeong K. Kim, "*Packaging Effect on MEMS Pressure Sensor Performance*", IEEE Transactions on Components and Packaging Technology, Vol. 30, No. 2, pp. 285-293, June 2007.

[92] Xiaodong Wang, Baoqing Li, Onofrio L. Russo, Harry T. Roman, Ken K. Chin, Kenneth R. Farmer, "*Diaphragm Design Guidelines and an Optical Pressure Sensor based on MEMS Technique*", Microelectronics Journal, Vol. 37, No. 1, pp. 50-56, January 2006.

[93] Kaoru Yamashita, Hiroki Nishimoto, Masanori Okuyama, "*Diaphragm Deflection Control of Piezoelectric Ultrasonic Microsensors for Sensitivity Improvement*", Sensors and Actuators A: Physical, Vol. 139, No. 1, pp. 118-123, 2007.

[94] Michael A. Huff, Aleks D. Nikolich, and Martin A. Schmidt, "*A Threshold Pressure Switch Utilizing Plastic Deformation of Silicon*", 1991 Transducers, Conference Proceedings, pp. 177-180, 1999.

[95] Jose A. Segovia, Montserrat Fernandez-Bolaiios and Jose M. Quero., "*Design of a Programmable Pressure Switch Suspended Gate MOSFET*", 2005 Spanish Conference on Electron Devices, pp. 525-528, February 2-4, 2005.

[96] J.W. Kang, and K. Simonette, "*Surface Micromachined Multi-Layer Moving Gate Field Effect Transistor (MOGFET) Pressure Switch with Integrated Vacuum Sealed Cavity*", 12th IEEE International Conference on Micro Electro Mechanical Systems, pp. 499-504, January 21, 1999.

[97] Xia Zhang, Camilla Karnfelt, Johan Liu, Shiwei Ma, Xu Wang, Linqin Meng, Herbert Zirath, *"Realization of Ultra Wideband Bandpass Filter based on LCP Substrate for Wireless Application"*, International Symposium on High Density Packaging and Microsystem Integration, pp. 1-5, June 26-28, 2007.

[98] B. Kim, S. Nikolaou, G.E.Ponchak, Y.S. Kim, J.Papapolymerou, M.M. Tentzeris, *"A Curvature CPW-fed Ultra-Wideband Monopole Antenna on Liquid Crystal Polymer Substrate using Flexible Characteristic,"* IEEE International Symposium on Antennas and Propagation Society, pp. 1667-1670, July 9-14, 2006.

[99] N. Kingsley, Guoan Wang, J. Papapolymerou, *"14 GHz Microstrip MEMS Phase Shifters on Flexible, Organic Substrate"*, 2005 European Microwave Conference, Vol. 1, October 4-6, 2005.

[100] J. N. Palasagaram, R. Ramadoss, *"MEMS-Capacitive Pressure Sensor Fabricated Using Printed-Circuit-Processing Techniques"*, IEEE Sensors, Vol. 6, No. 6, pp. 1374-1375, December, 2006.

[101] Guoan Wang, D. Thompson, E.M. Tentzeris, J. Papapolymerou, *"Low Cost RF MEMS Switches using LCP Substrate"*, 34th European Microwave Conference, Vol. 3, pp. 1441-1444, October 11-15, 2004.

[102] R. Dean, J. Pack, N. Sanders, P. Reiner, *"Micromachined LCP for Packaging MEMS Sensors"*, 31th Annual Conference of IEEE Industrial Electronics Society, November 6-10, 2005.

[103] S. Mukherjee, M. Swaminathan, E. Matoglu, *"Statistical Analysis and Diagnosis Methodology for RF Circuits in LCP Substrates"*, IEEE Transactions on Microwave Theory and Techniques, Vol. 53, No. 11, pp. 3621-3630, November 2005.

[104] Dae-Hee Weon, L.P.B. Katehi, S. Mohammadi, *"*3-D Integrated Inductors and Transformers on Liquid Crystal Polymer Substrate*"*, IEEE MTT-S International Microwave Symposium, pp. 1381-1384, June 11-16, 2006.

[105] M.M. Tentzeris, J. Laskar, J. Papapolymerou, S. Pinel, V. Palazzari, R. Li, G. DeJean, N. Papageorgiou, D. Thompson, R. Bairavasubramanian, S Sarkar, J.H. Lee, *"3-D-Integrated RF and Millimeter-wave Functions and Modules using Liquid Crystal Polymer (LCP) System-on-Package Technology"*, IEEE Transactions on Advanced Packaging, Vol. 27, No. 2, pp. 332-340, May 2004.

[106] Jiri Janata, *Principles of Chemical Sensors,* New York, NY and London, UK: Plenum Press, 1989.

[107] T.E. Edmonds and Contributors, *Chemical Sensors,* Blackie and Son Ltd., 1988.

[108] M. Carminati, G. Ferrari, F. Guagliardo, M. Sampietro, "*ZeptoFarad Capacitance Detection with a Miniaturized CMOS Current Front-End for Nanoscale Sensor*", Sensors and Actuators Vol. A: Physical, Vol. 172, pp. 117-123, 2011.

[109] J. Wei, C. Yue, M. van der Velden, Z.L. Chen, Z.E. Lie, K.A.A. Makinwa, P.M. Sarro, "*Design, Fabrication, and Characterization of a Femto-Farad Capacitive Sensor for Pico-Liter Liquid Monitoring*", Sensors and Actuators Vol. A: Physical, Vol. 162, pp. 406-417, 2010.

[110] V. Matko, "*Next Generation AT_Cut Quartz Crystal Sensing Devices*", Sensors, vol. 5, no. 11, pp. 4474-4482, 2011.

[111] V. Matko, M. Milanovic, "*Temperature-Compensated Capacitance-Frequency Converter with High Resolution*", Sensors and Actuators Vol. A: Physical, Vol. 220, pp. 262-269, December 2014.

[112] L.G. Miller, E.R. Wagner, "*Resonant Phase Shift Technique for the Measurement of Small Changes in Grounded Capacitors*", Rev. Science Instrumentation, Vol. 61, pp. 1267, 1990.

[113] K.M.E. Stewart, W.T. Chen, R.R. Mansour, A. Penlidis, "Doped Poly(2,5-dimethylaniline) for the Detection of Ethanol", submitted to Journal of Applied Polymer Science. (Accepted)